



# Politecnico di Bari

Repository Istituzionale dei Prodotti della Ricerca del Politecnico di Bari

## EM Tracking Systems and Miniaturized Biosensors for Minimally Invasive Surgery

This is a PhD Thesis

*Original Citation:*

EM Tracking Systems and Miniaturized Biosensors for Minimally Invasive Surgery / Ragolia, Mattia Alessandro. - ELETTRONICO. - (2022). [10.60576/poliba/iris/ragolia-mattia-alessandro\_phd2022]

*Availability:*

This version is available at <http://hdl.handle.net/11589/246160> since: 2022-12-20

*Published version*

DOI:10.60576/poliba/iris/ragolia-mattia-alessandro\_phd2022

Publisher: Politecnico di Bari

*Terms of use:*

(Article begins on next page)



LIBERATORIA PER L'ARCHIVIAZIONE DELLA TESI DI DOTTORATO

Al Magnifico Rettore  
del Politecnico di Bari

Il sottoscritto Mattia Alessandro RAGOLIA, nato a MILANO il 26.03.1992, e residente a BARI, in via dei Mille 40, e-mail [mattiaalessandro.ragolia@poliba.it](mailto:mattiaalessandro.ragolia@poliba.it), iscritto al 3° anno di Corso di Dottorato di Ricerca in Ingegneria Elettrica e dell'Informazione, ciclo XXXV, ed essendo stato ammesso a sostenere l'esame finale con la prevista discussione della tesi dal titolo:

“EM Tracking Systems and Miniaturized Biosensors for Minimally Invasive Surgery”

**DICHIARA**

- 1) di essere consapevole che, ai sensi del D.P.R. n. 445 del 28.12.2000, le dichiarazioni mendaci, la falsità negli atti e l'uso di atti falsi sono puniti ai sensi del codice penale e delle Leggi speciali in materia, e che nel caso ricorressero dette ipotesi, decade fin dall'inizio e senza necessità di nessuna formalità dai benefici conseguenti al provvedimento emanato sulla base di tali dichiarazioni;
- 2) di essere iscritto al Corso di Dottorato di ricerca in Ingegneria Elettrica e dell'Informazione, ciclo XXXV, corso attivato ai sensi del “Regolamento dei Corsi di Dottorato di ricerca del Politecnico di Bari”, emanato con D.R. n.286 del 01.07.2013;
- 3) di essere pienamente a conoscenza delle disposizioni contenute nel predetto Regolamento in merito alla procedura di deposito, pubblicazione e autoarchiviazione della tesi di dottorato nell'Archivio Istituzionale ad accesso aperto alla letteratura scientifica;
- 4) di essere consapevole che attraverso l'autoarchiviazione delle tesi nell'Archivio Istituzionale ad accesso aperto alla letteratura scientifica del Politecnico di Bari (IRIS-POLIBA), l'Ateneo archiverà e renderà consultabile in rete (nel rispetto della Policy di Ateneo di cui al D.R. 642 del 13.11.2015) il testo completo della tesi di dottorato, fatta salva la possibilità di sottoscrizione di apposite licenze per le relative condizioni di utilizzo (di cui al sito <http://www.creativecommons.it/Licenze>), e fatte salve, altresì, le eventuali esigenze di “embargo”, legate a strette considerazioni sulla tutelabilità e sfruttamento industriale/commerciale dei contenuti della tesi, da rappresentarsi mediante compilazione e sottoscrizione del modulo in calce (Richiesta di embargo);
- 5) che la tesi da depositare in IRIS-POLIBA, in formato digitale (PDF/A) sarà del tutto identica a quelle **consegnate**/inviata/da inviarsi ai componenti della commissione per l'esame finale e a qualsiasi altra copia depositata presso gli Uffici del Politecnico di Bari in forma cartacea o digitale, ovvero a quella da discutere in sede di esame finale, a quella da depositare, a cura dell'Ateneo, presso le Biblioteche Nazionali Centrali di Roma e Firenze e presso tutti gli Uffici competenti per legge al momento del deposito stesso, e che di conseguenza va esclusa qualsiasi responsabilità del Politecnico di Bari per quanto riguarda eventuali errori, imprecisioni o omissioni nei contenuti della tesi;
- 6) che il contenuto e l'organizzazione della tesi è opera originale realizzata dal sottoscritto e non compromette in alcun modo i diritti di terzi, ivi compresi quelli relativi alla sicurezza dei dati personali; che pertanto il Politecnico di Bari ed i suoi funzionari sono in ogni caso esenti da responsabilità di qualsivoglia natura: civile, amministrativa e penale e saranno dal sottoscritto tenuti indenni da qualsiasi richiesta o rivendicazione da parte di terzi;
- 7) che il contenuto della tesi non infrange in alcun modo il diritto d'Autore né gli obblighi connessi alla salvaguardia di diritti morali od economici di altri autori o di altri aventi diritto, sia per testi, immagini, foto, tabelle, o altre parti di cui la tesi è composta.

Bari, 20.12.2022

Firma

Il sottoscritto, con l'autoarchiviazione della propria tesi di dottorato nell'Archivio Istituzionale ad accesso aperto del Politecnico di Bari (POLIBA-IRIS), pur mantenendo su di essa tutti i diritti d'autore, morali ed economici, ai sensi della normativa vigente (Legge 633/1941 e ss.mm.ii.),

**CONCEDE**

- al Politecnico di Bari il permesso di trasferire l'opera su qualsiasi supporto e di convertirla in qualsiasi formato al fine di una corretta conservazione nel tempo. Il Politecnico di Bari garantisce che non verrà effettuata alcuna modifica al contenuto e alla struttura dell'opera.
- al Politecnico di Bari la possibilità di riprodurre l'opera in più di una copia per fini di sicurezza, back-up e conservazione.

Bari, 20.12.2022

Firma



**POLITECNICO DI BARI**

DEPARTMENT OF ELECTRICAL AND INFORMATION ENGINEERING

ELECTRICAL AND INFORMATION ENGINEERING

PH.D. PROGRAM

SSD: ING-INF/07–ELECTRICAL AND ELECTRONIC MEASUREMENTS

**FINAL DISSERTATION**

---

**EM Tracking Systems and Miniaturized  
Biosensors for Minimally Invasive Surgery**

---

by

MATTIA ALESSANDRO RAGOLIA

SUPERVISOR:

PROF. ANNA M. L. LANZOLLA

*Coordinator of Ph.D. Program:*

*Prof. Mario Carpentieri*

---

*Course n°35, 01/11/2019 - 31/10/2022*



**POLITECNICO DI BARI**  
DEPARTMENT OF ELECTRICAL AND INFORMATION ENGINEERING  
ELECTRICAL AND INFORMATION ENGINEERING  
PH.D. PROGRAM  
SSD: ING-INF/07–ELECTRICAL AND ELECTRONIC MEASUREMENTS  
**FINAL DISSERTATION**

---

**EM Tracking Systems and Miniaturized  
Biosensors for Minimally Invasive Surgery**

---

by

MATTIA ALESSANDRO RAGOLIA

REFEREES:

PROF. SABRINA GRASSINI  
PROF. MARCO MUGNAINI

SUPERVISOR:

PROF. ANNA M. L. LANZOLLA

*Coordinator of Ph.D. Program:*

*Prof. Mario Carpentieri*

---

*Course n°35, 01/11/2019 - 31/10/2022*

*Misura gli altri come sei misurato da Dio: con una misura abbondante, piena di amore. È esattamente questo che l'uomo ricerca, e ciò che lo rende felice: l'amare ed essere amato. Esamina accuratamente il tuo cuore, getta via l'incertezza e sii certo: Dio che ha creato il mondo, misurando con precisione come un bravo architetto, e ha fatto l'uomo e la donna così belli, ha a cuore la tua vita e ha in serbo cose meravigliose per te. Sii grato.*

# *Abstract*

The goal of this work is to support minimally invasive surgery (MIS) by developing sensors and systems able to assist surgeon during operations, remaining “invisible” to the medical staff. Hence, in this thesis we focused on the development of an electromagnetic tracking system (EMTS), which can be employed for intracorporeal interventions, since it does not require a direct line of sight between the source of the signal and the sensor, as instead is required for optical systems. Indeed, in order to reduce invasiveness, very small magnetic sensors are used to measure the magnetic field of known geometry produced by a field generator (FG); due to the small sensor sizes, the sensitivity is reduced, and when employing current commercial systems, the surgeon needs to place the FG too much near the operating volume (i.e., patient’s table), thus hindering the staff during the operation. Hence, in this thesis is presented a novel EMTS, developed to increase the tracking distance of current systems, and several considerations are provided, which can be applied to the development of other EMTSs. Moreover, a virtual platform is developed, which permits to analyze system performances by adding noise components and simulating error sources, hence the robustness and the accuracy of the system and its weaknesses can be studied. The platform can be particularly useful for system prototyping, by investigating the effects of system parameters (geometrical and electrical ones) before the fabrication of the real EMTS prototype.

Additionally, along with the need of continuously tracking the surgical tools inside human body there is the need of information about the real-time status of the patient. Therefore, this thesis will also focus on the development of a miniaturized sensor to obtain accurate measurements of ions, by finding robust fabrication parameters to achieve high sensing performances, with particular focus on  $K^+$  sensing: needle-shaped ISEs (Ion-Selective electrodes) can hence be inserted into the surgical instruments, thus providing important real-time information about cellular health, measuring  $K^+$  concentration directly from blood inevitably present during surgery.

# *Contents*

<b>Abstract</b> .....	<b>ii</b>
<b>Contents</b> .....	<b>iii</b>
<b>List of publications</b> .....	<b>vii</b>
<b>Chapter 1</b> .....	<b>1</b>
<b>Introduction</b> .....	<b>1</b>
1.1 Overview.....	1
1.2 Thesis Objectives.....	2
1.3 Thesis Structure .....	3
<b>Chapter 2</b> .....	<b>5</b>
<b>Overview of Tracking Systems for Surgical Navigation</b> .....	<b>5</b>
2.1 Optical Tracking Systems.....	6
2.2 EM Tracking Systems.....	9
2.2.1 Field Generator.....	9
2.2.2 Coil Sensor.....	10
2.2.3 Modeling the Transmitting Coils of the FG.....	12
<b>Chapter 3</b> .....	<b>15</b>
<b>System Overview and Performance Analysis</b> .....	<b>15</b>
3.1 Prototype of the realized EMTS .....	16
3.1.1 Field Generator.....	19
3.1.2 Coil Sensor.....	21
3.2 Hardware Development .....	21
3.2.1 Coherent Sampling.....	21

3.2.2	DAQ Synchronization.....	22
3.2.3	Analysis of the Electronic Board .....	23
3.2.4	Improved DAQ Devices.....	23
3.2.5	Cable’s Shielding .....	24
3.3	Performance Analysis .....	24
3.3.1	Induced Voltage Repeatability .....	24
3.3.2	Induced Voltage Drift .....	26
3.3.3	Excitation Currents Noise Quantification .....	29
3.4	Validation.....	29
3.4.1	Repeatability Error Evaluation through Gradients.....	30
3.4.2	Test Protocol and Position Repeatability Estimation.....	31
3.4.3	Analysis of Voltage Drift.....	34
3.4.4	Comparison with the State of the Art: the Aurora system .....	35
3.4.5	Effect of Excitation Currents Noise .....	37
3.5	Chapter Conclusions .....	38
	<b>Chapter 4 .....</b>	<b>41</b>
	<b>FG Configuration Analysis from Magnetic Field Gradients .....</b>	<b>41</b>
4.1	Assessment of Position RMS Error by using Experimental Data .....	42
4.1.1	Results .....	43
4.2	Analysis of Magnetic Field Gradients .....	47
4.3	Assessment of Position RMS Error by using Magnetic Field Model.....	50
4.3.1	Results .....	51
4.4	Chapter Conclusions .....	53
	<b>Chapter 5 .....</b>	<b>55</b>
	<b>Accuracy of Position Reconstruction .....</b>	<b>55</b>
5.1	Position Reconstruction Algorithm .....	56
5.2	Validation of the Reconstruction Algorithms.....	57

5.2.1	Case <i>a</i> : Orientation Perturbation.....	59
5.2.2	Case <i>b</i> : Position Perturbation.....	60
5.2.3	Case <i>c</i> : Orientation and Position Perturbation.....	61
5.3	Experimental Results.....	63
5.4	Compensation of Excitation Currents Noise.....	65
5.4.1	Simulated Data: Currents Noise.....	66
5.4.2	Simulated Data: both Currents and Measurement Noise.....	67
5.4.3	Experimental Data.....	69
5.5	Chapter Conclusions.....	70
	<b>Chapter 6.....</b>	<b>71</b>
	<b>A Virtual Platform for Real-Time Performance Analysis of EMTSs.....</b>	<b>71</b>
6.1	Sources of Error.....	72
6.2	Assessment Protocols.....	73
6.3	Virtual Platform.....	74
6.3.1	3D View and Real-Time Tracking Statistic.....	75
6.3.2	EMTS Model Import.....	76
6.3.3	Reconstruction Algorithm and Magnetic Field Model.....	77
6.3.4	Experimental or Simulation Mode.....	77
6.3.5	Noise Section.....	78
6.4	Validation.....	79
6.4.1	DAQ Device Selection.....	79
6.4.2	FG Configuration Optimization.....	80
6.4.3	Comparison with Experimental Test on the EMTS Prototype.....	81
6.5	Chapter Conclusions.....	82
	<b>Chapter 7.....</b>	<b>85</b>
	<b>Platinum Nanostructured Miniaturized Ion-Sensors.....</b>	<b>85</b>
7.1	Background.....	87

7.1.1	Working Principle .....	87
7.1.2	Performance Parameters.....	88
7.2	Materials and Methods.....	89
7.2.1	Synthesis of Pt Nanostructures.....	89
7.2.2	Ion-Selective Membrane .....	90
7.2.3	Morphological Analysis .....	91
7.2.4	Electrochemical Measurements .....	92
7.3	Results and Discussion .....	92
7.3.1	Membrane Adhesion and Nanostructure Thickness .....	92
7.3.2	Morphology of the Sensors .....	93
7.3.3	Electrochemical Performances of the Sensors .....	96
7.3.4	Optimization of Pt Nanostructuring Parameters with respect to K <sup>+</sup> Sensing Performances.....	98
7.4	Chapter Conclusions .....	100
	<b>Chapter 8 .....</b>	<b>103</b>
	<b>Conclusions .....</b>	<b>103</b>
	<b>Appendix A .....</b>	<b>107</b>
	<b>Funding Acknowledgements .....</b>	<b>109</b>
	<b>Personal Acknowledgements.....</b>	<b>110</b>
	<b>References .....</b>	<b>113</b>

# *List of publications*

## **Journals:**

- [1] A. Di Nisio, N. Giaquinto, A. M. L. Lanzolla, **M. A. Ragolia**, M. Scarpetta, and S. Carrara, “Platinum Nanostructured Needle-Shaped Sensors for Ion Detection in Biomedical Applications,” *IEEE Sensors Journal*, vol. 22, no. 23, pp. 22404–22412, Dec. 2022, doi: [10.1109/JSEN.2022.3216682](https://doi.org/10.1109/JSEN.2022.3216682).
- [2] G. Stano, A. Di Nisio, A. M. Lanzolla, **M. A. Ragolia**, and G. Percoco, “Additive manufacturing for capacitive liquid level sensors,” *Int J Adv Manuf Technol*, vol. 123, no. 7, pp. 2519–2529, Dec. 2022, doi: [10.1007/s00170-022-10344-7](https://doi.org/10.1007/s00170-022-10344-7).
- [3] A. M. L. Lanzolla, F. Attivissimo, G. Percoco, **M. A. Ragolia**, G. Stano, and A. Di Nisio, “Additive Manufacturing for Sensors: Piezoresistive Strain Gauge with Temperature Compensation,” *Applied Sciences*, vol. 12, no. 17, pp. 8607–8607, Aug. 2022, doi: [10.3390/app12178607](https://doi.org/10.3390/app12178607).
- [4] M. Scarpetta, M. Spadavecchia, G. Andria, **M. A. Ragolia**, and N. Giaquinto, “Accurate simultaneous measurement of heartbeat and respiratory intervals using a smartphone,” *Journal of Instrumentation*, vol. 17, no. 07, pp. P07020–P07020, Jul. 2022, doi: [10.1088/1748-0221/17/07/P07020](https://doi.org/10.1088/1748-0221/17/07/P07020).
- [5] **M. A. Ragolia**, F. Attivissimo, A. Di Nisio, A. M. L. Lanzolla, and M. Scarpetta, “A virtual platform for real-time performance analysis of electromagnetic tracking systems for surgical navigation,” *ACTA IMEKO*, vol. 10, no. 4, pp. 103–103, Dec. 2021, doi: [10.21014/acta\\_imeko.v10i4.1191](https://doi.org/10.21014/acta_imeko.v10i4.1191).
- [6] M. Scarpetta, M. Spadavecchia, F. Adamo, **M. A. Ragolia**, and N. Giaquinto, “Detection and Characterization of Multiple Discontinuities in Cables with Time-Domain Reflectometry and Convolutional Neural Networks,” *Sensors*, vol. 21, no. 23, pp. 8032–8032, Dec. 2021, doi: [10.3390/s21238032](https://doi.org/10.3390/s21238032).
- [7] **M. A. Ragolia**, A. M. L. Lanzolla, G. Percoco, G. Stano, and A. Di Nisio, “Thermal Characterization of New 3D-Printed Bendable, Coplanar Capacitive Sensors,” *Sensors*, vol. 21, no. 19, pp. 6324–6324, Sep. 2021, doi: [10.3390/s21196324](https://doi.org/10.3390/s21196324).

- [8] F. Attivissimo, A. D. Nisio, A. M. L. Lanzolla and **M. A. Ragolia**, “Analysis of position estimation techniques in a surgical EM tracking system,” in *IEEE Sensors Journal*, vol. 21, no. 13, pp. 14389-14396, Jul. 2021, doi: [10.1109/JSEN.2020.3042647](https://doi.org/10.1109/JSEN.2020.3042647).
- [9] G. Stano, A. Di Nisio, A. M. Lanzolla, **M. A. Ragolia**, and G. Percoco, “Fused filament fabrication of commercial conductive filaments: experimental study on the process parameters aimed at the minimization, repeatability and thermal characterization of electrical resistance,” *The International Journal of Advanced Manufacturing Technology*, vol. 111, no. 9–10, pp. 2971–2986, Dec. 2020, doi: [10.1007/s00170-020-06318-2](https://doi.org/10.1007/s00170-020-06318-2).
- [10] G. Andria, F. Attivissimo, A. Di Nisio, A. M. L. Lanzolla, and **M. A. Ragolia**, “Assessment of position repeatability error in an electromagnetic tracking system for surgical navigation,” *Sensors (Switzerland)*, vol. 20, no. 4, pp. 961–961, Feb. 2020, doi: [10.3390/s20040961](https://doi.org/10.3390/s20040961).

#### Conferences:

- [1] L. De Palma, F. Attivissimo, A. Di Nisio, A. M. L. Lanzolla, **M. A. Ragolia**, and M. Spadavecchia, “Development of a web-based system for interfacing a portable Bluetooth vital sign monitor,” in *2022 IEEE International Symposium on Medical Measurements and Applications (MeMeA)*, Jun. 2022, pp. 1–6. doi: [10.1109/MeMeA54994.2022.9856526](https://doi.org/10.1109/MeMeA54994.2022.9856526).
- [2] **M. A. Ragolia**, F. Attivissimo, A. Di Nisio, A. M. L. Lanzolla, and M. Scarpetta, “Reducing effect of magnetic field noise on sensor position estimation in surgical EM tracking,” in *2021 IEEE International Symposium on Medical Measurements and Applications (MeMeA)*, Jun. 2021, pp. 1–6. doi: [10.1109/MeMeA52024.2021.9478723](https://doi.org/10.1109/MeMeA52024.2021.9478723).
- [3] M. Scarpetta, M. Spadavecchia, G. Andria, **M. A. Ragolia**, and N. Giaquinto, “Simultaneous Measurement of Heartbeat Intervals and Respiratory Signal using a Smartphone,” in *2021 IEEE International Symposium on Medical Measurements and Applications (MeMeA)*, Jun. 2021, pp. 1–5. doi: [10.1109/MeMeA52024.2021.9478711](https://doi.org/10.1109/MeMeA52024.2021.9478711). (**Awarded with best Student Paper Award**)
- [4] **M. A. Ragolia**, A. di Nisio, A. M. Lanzolla, G. Percoco, M. Scarpetta, and G. Stano, “Thermal Characterization of Electrical Resistance of 3D printed sensors,” in *2021 IEEE International Instrumentation and Measurement Technology Conference (I2MTC)*, May 2021, pp. 1–6. doi: [10.1109/I2MTC50364.2021.9459968](https://doi.org/10.1109/I2MTC50364.2021.9459968).
- [5] M. Scarpetta, M. Spadavecchia, G. Andria, **M. A. Ragolia**, and N. Giaquinto, “Analysis of TDR Signals with Convolutional Neural Networks,” in *2021 IEEE*

- International Instrumentation and Measurement Technology Conference (I2MTC)*, May 2021, pp. 1–6. doi: [10.1109/I2MTC50364.2021.9460009](https://doi.org/10.1109/I2MTC50364.2021.9460009).
- [6] F. Adamo, F. Attivissimo, A. Di Nisio, **M. A. Ragolia**, and M. Scarpetta, “A New Processing Method to Segment Olive Trees and Detect Xylella Fastidiosa in UAVs Multispectral Images,” in *2021 IEEE International Instrumentation and Measurement Technology Conference (I2MTC)*, May 2021, pp. 1–6. doi: [10.1109/I2MTC50364.2021.9459835](https://doi.org/10.1109/I2MTC50364.2021.9459835).
- [7] N. Giaquinto, M. Scarpetta, **M. A. Ragolia**, and P. Pappalardi, “Real-time drip infusion monitoring through a computer vision system,” in *2020 IEEE International Symposium on Medical Measurements and Applications (MeMeA)*, Jun. 2020, pp. 1–5. doi: [10.1109/MeMeA49120.2020.9137359](https://doi.org/10.1109/MeMeA49120.2020.9137359).
- [8] **M. A. Ragolia**, F. Attivissimo, A. Di Nisio, and A. Maria Lucia Lanzolla, “Assessment of position repeatability of surgical EM tracking systems employing magnetic field model,” in *2020 IEEE International Symposium on Medical Measurements and Applications (MeMeA)*, Jun. 2020, pp. 1–6. doi: [10.1109/MeMeA49120.2020.9137161](https://doi.org/10.1109/MeMeA49120.2020.9137161).
- [9] **M. A. Ragolia**, F. Attivissimo, A. D. Nisio, and A. Maria Lucia Lanzolla, “Evaluation of position RMS error from magnetic field gradient for surgical em tracking systems,” in *I2MTC 2020 - International Instrumentation and Measurement Technology Conference, Proceedings*, May 2020, pp. 1–6. doi: [10.1109/I2MTC43012.2020.9128837](https://doi.org/10.1109/I2MTC43012.2020.9128837).

# *Chapter 1*

---

## *Introduction*

### **1.1 Overview**

Increased focus on improving patient safety and surgical outcomes in today's operating rooms is driving the transition from traditional surgery to minimally invasive surgery (MIS) [1]–[3], which offers many benefits such as reduced risk of infections and post-operative pain and decreased recovery time.

Significant support is provided by Computer Assisted Surgery (CAS), which relies on medical imaging techniques such as Magnetic Resonance Imaging (MRI), Computed Tomography (CT), and Ultrasound (US), to provide a three-dimensional model of the patient's anatomy [4]–[12], allowing for diagnostic and the pre-operative planning of interventions. CAS combines the anatomical model with the real-time position and orientation of surgical instruments, provided by tracking systems and guiding the surgeon during the intervention. The set of procedures that allow real-time visualization of the operating scenario during surgery is called *surgical navigation*.

Optical and electromagnetic tracking systems are the most used in surgery navigation. Optical tracking systems (OTS) are very robust and offer high accuracy and resolution, but the dependence from a direct line-of-sight between the cameras and the markers placed on the instrument prevents its use for intra-corporal interventions.

Electromagnetic tracking systems (EMTS) use a small coil sensor inserted into the surgical tool to determine the position and the orientation of the target object by measuring the amplitude of magnetic fields with known geometry, generated by a field generator (FG) [13]–[15]. The very small size of the magnetic sensor and the

independence from line-of-sight, overcome the limitations of OTSs. The frequencies of EMTSs, in the order of a few kilohertz, ensures greater penetration with respect to, e.g., microwaves, which can instead be exploited for other purposes such as indoor localization, imaging and monitoring [16]–[18].

## 1.2 Thesis Objectives

EMTS technology presents two main limitations: *a)* it has high sensitivity to EM interferences provided by electronic devices and to magnetic field distortions due to metal objects; *b)* current commercial systems are not able to provide accurate position estimations over a large distance from the signal source, due to the degradation of the magnetic field amplitude with the distance from the field generator. Hence, the signal source must be placed too much near the operating volume (i.e., patient's table), thus hindering the medical staff during the operation. Currently, commercial EMTSs provide accurate estimation of surgical instrument position only for limited distance from the field generator, generally not more than 0.5 m [13], [19]. It should be noted that a higher tracking distance can be achieved by using some systems, such as Polhemus Long Ranger trackers [20], but they employ larger FGs and bigger sensors, which are not suitable to track surgical instruments such as needles and endoscopes and cannot be used in many applications where a very small size is required.

The proposed research aims to overcome the limit of commercial EMTS, thus increasing the tracking volume achieved by current commercial systems, developing an EMTS to obtain accurate position estimation of the sensor at distance  $> 0.5$  m from the field generator, by ensuring good performances in terms of accuracy and repeatability position error. Particular consideration will regard the development of a validation protocol to assess system performance, and the experimental setup for the metrological characterization of the system.

Additionally, the need of integrated sensors for surgery is nowadays crucial, since it gives information about key parameters related to patients' status during surgical procedures. In particular, the role of ion concentration measurements is particularly useful in the biomedical field: among several, potassium ion is key to be monitored during surgical procedures as a biomarker of organs failure. The need for miniaturization of ion sensing systems is leading toward the development of sensors based on all-solid-state ion-selective electrodes but realized onto working electrodes in very small sizes. The reason relies on typical applications where minimum invasiveness is a main issue to be considered, e.g., in surgery. Hence, this dissertation introduces new miniaturized  $K^+$ -selective sensors with working electrodes obtained by electrodeposition of Pt-NSs on a very thin Pt wire with diameter of 0.1 mm, i.e., in needle-shape. For the first time in

literature, the effects of electrodeposition voltage and time on the morphology of the obtained nanostructures is investigated, in order to find a set of optimized electrodeposition parameters for a regular fabrication of high performances  $K^+$  ISEs.

### 1.3 Thesis Structure

This dissertation is organized into six major work chapters.

Chapter 2 illustrates the state of the art of tracking systems for surgical navigation, the limitation of commercial systems, provides background theory about EM tracking systems.

Chapter 3 shows the experimental setup to characterize an innovative prototype of EMTS, developed to overcome the limitation of commercial systems. Several tests are performed on the system to assess the performance in terms of signal repeatability and drift, as well their effect on position estimation.

In Chapter 4 the proposed configuration of FG is assessed by evaluating the gradients of the AC magnetic field produced by the transmitting coils, and the RMS position error is evaluated by performing simulated and experimental tests.

Chapter 5 illustrates an algorithm to reconstruct sensor position and orientation, and several tests are conducted to assess its performances. Moreover, a method to compensate the position error caused by noise due to the excitation of transmitting coils is presented and validated.

Chapter 6 discusses the main sources of error in EMTSs, and the importance of knowing them during system developing. Hence, a virtual platform is proposed, which is developed as a validation protocol to provide a tool for analyzing system performances during the prototyping phase, which is validated by simulated and experimental tests performed on the EMTS prototype.

Chapter 7 illustrates the fabrication and characterization of an innovative miniaturized biosensor to monitor potassium concentration in blood during surgical intervention. The sensors can be integrated with the EM tracking system during surgical interventions, providing the surgeon with real-time information about an important biomarker.

Finally, in Chapter 8 the key results of this dissertation are summarized and discussed, along with future work proposals for improving system performances.



# *Chapter 2*

---

## *Overview of Tracking Systems for Surgical Navigation*

In order to locate the surgical instruments in the operating volume, ad hoc tracking systems are used, which provide real-time position and orientation with respect to a local or global reference system. In the same way that the GPS navigator provides the driver with information on the route and position of the vehicle, the navigation systems guide the surgeon during surgical operations. They support more accurate diagnoses, planning the operation and performing IGS (Image-Guided Surgery) interventions.

Basically, tracking systems are composed of a signal source, one or more sensors, and a data processing unit. The system processes the signal acquired by the sensor and provides continuous tracking of the surgical instrument with respect to the reference system. Depending on the technology used, the sensor or signal source can be attached to the target.

Tracking systems are used in many fields, such as military, virtual reality, and indoor location [21]. To evaluate suitability for use in surgery, and to compare the performances of different tracking systems, it is necessary to evaluate some characteristic parameters:

- Signal latency [ms]: indicates the delay between a change in position or orientation of the target and the related information provided by the system. Latencies greater than 50 ms are not allowed.

- Refresh rate [Hz]: indicates the frequency with which the system updates the position and orientation information. The minimum required value is 20 Hz.
- Resolution [mm] [°]: is the smallest change in position and orientation that the system is able to measure. Since medical images have a resolution of approximately 1 mm, the resolution required of navigation systems is <1 mm and <0.1 °.
- Accuracy [mm] [°]: indicates the position and orientation error committed with respect to the real value. The reference values are the same as for the resolution.
- Sensitivity to interference and environmental factors [mm] [°]: in order to have a robust and reliable system, it is necessary to guarantee a certain immunity to external interference. The nature of the interference depends on the specific technology used. The reference values are similar to the previous parameters.
- Operating volume [m<sup>3</sup>]: indicates the portion of space within which the system can operate with a given resolution and accuracy. Values of approximately 5 m<sup>3</sup> are required.
- Number of degrees of freedom (Degree of Freedom - DoF): it is defined as the number of independent variables that allow to uniquely determine the position and orientation of a point in space.

There are several tracking systems that can be used in surgery, classified according to the technology used: mechanical, inertial, acoustic, optical, and electromagnetic systems. The following paragraphs describe the operating principles of the two most common tracking systems for minimally invasive surgical navigation: optical and electromagnetic tracking systems.

## 2.1 Optical Tracking Systems

Optical tracking systems (OTS) are based on well-established and reliable technology, offering a good refresh rate and high accuracy and resolution in a large operating volume [22].

They usually consist of a fixed infrared (IR) emitter and a camera, and a set of markers fixed on the target object. The beam generated by the emitter hits the markers, which are formed by a series of spheres arranged in a known configuration, which reflect the radiation; the camera detects the reflected wave and computes the position and orientation of the target through geometric triangulation (Figure 2.1). Depending on the system used,

the IR source can be linked to the target to be located, using active instead of passive markers.

It is important to note that the use of radiation in the visible spectrum is not recommended due to the presence of interference and its dependence on the brightness of the work area. The use of IR signals allows to filter unwanted radiation.

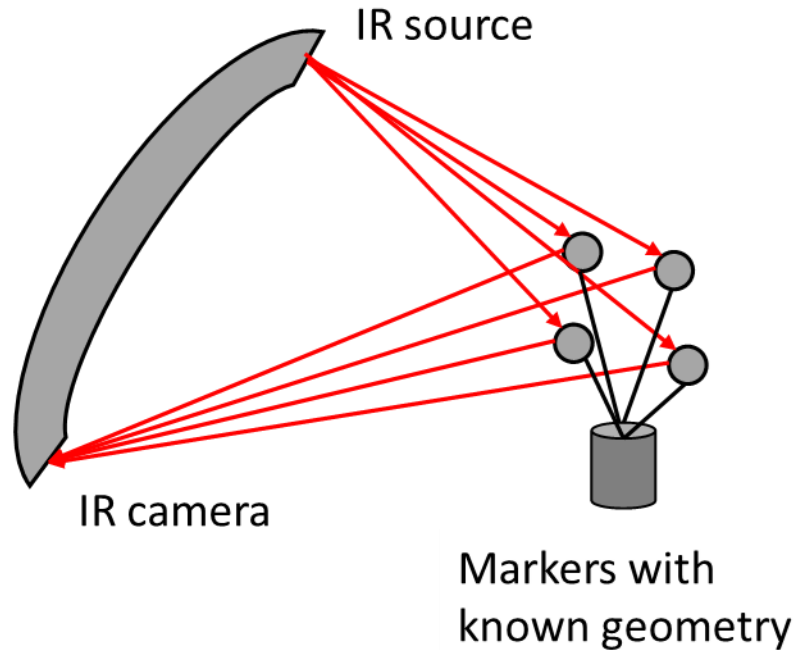


*Figure 2.1 Principle of operation of an optical tracking system.*

A major disadvantage of these systems is the dependence on a direct line of sight between camera and markers, which limits their use to extra-corporeal interventions. In fact, these systems rigidly connect the markers to the surgical instrument; if flexible tools are employed, such as catheters or needles, localization would not be possible. In addition, markers are usually disposable, since sterilization would reduce their reflective capacity.

Figure 2.2 shows an example of an OTS system produced by Masmec Biomed. It consists of an IR tracking module, a module for 3D processing and reconstruction of the anatomical area of interest, and a module for the fusion of multimodal images, in order to increase information content. It is also equipped with an ultrasound module for real-time operating support.

To refer the patient to the navigation system, several recording techniques are offered:

- Surface matching: A pointer is used on which a marker with reflective spheres is attached. The pointer is placed on a series of points of the skin to acquire the anatomical structure of the area of interest and refer it to the reference system of the tracking system.
- Fiducial matching: a marker is rigidly attached to the patient, and preoperative medical images are acquired. In this way a fixed reference will be displayed in the work area, with respect to which to refer during navigation.
- Back-up of the registration: carried out in case of accidental movements of the patient or of the reference markers.

This platform is widely used in neurosurgery, spinal surgery, and otolaryngology.



*Figure 2.2 Orion multimodal navigation system, based on optical technology. Produced by Masmec Biomed (<http://masmecbiomed.com/navigazione/orion>).*

## 2.2 EM Tracking Systems

When a direct line of sight is not available, electromagnetic tracking becomes the most appropriate choice. Electromagnetic Tracking Systems (EMTS) use a small coil sensor, inserted inside the surgical instrument, to determine its position and orientation by measuring the amplitude of the magnetic field of known geometry generated by a Field Generator (FG) [23]. The small size of the sensor and the independence from a direct line of sight allow to overcome the limitations of optical systems, also allowing the use of flexible instruments such as needles, catheters, and endoscopes. The frequencies of the FG's power signals, of the order of a few kilohertz, ensure a greater penetration capacity than, for example, microwaves, which can instead be used for other purposes, such as localization, image acquisition and monitoring in indoor environments [24].

EMTS technology presents two main limitations: a) it has high sensitivity to EM interferences provided by electronic devices and to magnetic field distortions due to metal objects; b) current commercial systems are not able to provide accurate position estimations over a large distance from the signal source, due to the degradation of the magnetic field amplitude with the distance from the FG.

### 2.2.1 Field Generator

The magnetic field is generated by a circuit consisting of a minimum number of three transmitting coils, arranged in space in a particular configuration. The number, size and arrangement of the FG coils determine the distribution of the magnetic field in space and the size of the FG itself, and influences tracking accuracy. Three types of generators can therefore be distinguished:

- Standard FGs: they are the most common type. Produced by different manufacturers, they are small and cover an operating volume of a few tens of centimeters.
- Flat FGs: they are flat and thin, designed to be placed directly under the operating table where the patient lies. Shielding the back of the FG greatly reduces the sensitivity to interference from below, such as induced eddy currents in metal structures.
- Mobile FGs: they are small FGs, which offer a small operating volume. Their advantage is that they can be positioned near the work, thus offering good accuracy despite the reduced range.
- Long-range FGs: available only from Pholemus Inc., they can cover areas up to 2 m.

The design of the FG (electrical and geometrical parameters, arrangements of transmitting coils, processing techniques) affects tracking performances, and different manufacturers propose their own FGs, but they do not provide their design principle. Hence, ongoing research is focused on designing FG's parameters with the aim of increasing tracking volume and accuracy. The main manufacturers of EMTS systems are Northern Digital Inc. (NDI, Canada), Polhemus Inc. (USA), and Ascension Technology Corp. (USA).

### 2.2.2 Coil Sensor

For the measurement of the AC magnetic field, the most common sensor used in surgical navigations is the coil sensor [25]. This sensor consists of a small solenoid of millimeter size, whose principle of operation is based on the law of electromagnetic induction.

When the sensor is immersed in a magnetic field of intensity  $B$ , an electromotive force is induced, proportional to the variation of the magnetic flux  $\Phi$  within the sensor, expressed by the Faraday-Newman-Lenz law:

$$e = -N \frac{d\Phi}{dt} = -N \cdot S \cdot \frac{dB}{dt} = -\mu_0 \cdot N \cdot S \cdot \frac{dH}{dt} \quad (1.1)$$

where  $N$  is the number of turns, and  $S$  is the section of the sensor. Since the sensor moves slowly, it could be assumed that  $S$  is constant. The sensitivity is proportional to the number of turns and the sensor surface, so it can easily be increased by varying these parameters. However, due to the small size required by surgical applications, sensitivity is very limited. An effective and commonly used way is to insert a ferromagnetic core inside the sensor, in order to increase its magnetic permeability, so to increase the amount of flow lines that are chained with sensor surface. (1.1) then becomes:

$$e = -\mu_0 \cdot \mu_r \cdot N \cdot S \cdot \frac{dH}{dt} \quad (1.2)$$

The relative magnetic permeability  $\mu_r$  can reach very high values, increasing the sensitivity by up to three orders of magnitude. However, the actual magnetic permeability

of the core also differs greatly from that of the ferromagnetic material, depending on the geometry of the core, according to the following formula:

$$\mu_c = \frac{\mu_r}{1 + K(\mu_r - 1)} \quad (1.3)$$

where K is the demagnetization coefficient, derived as

$$K \cong \frac{D_c^2}{l_c^2} \cdot \ln\left(\frac{2l_c}{D_c} - 1\right) \quad (1.4)$$

with  $D_c$  and  $l_c$  diameter and length of the ferromagnetic core. From the previous expressions it can be observed that a long and thin nucleus is preferable to one with a large section and reduced length (Figure 2.3). It is recommended  $l_c$  to be in the range  $[1.1 l, 1.4 l]$ .

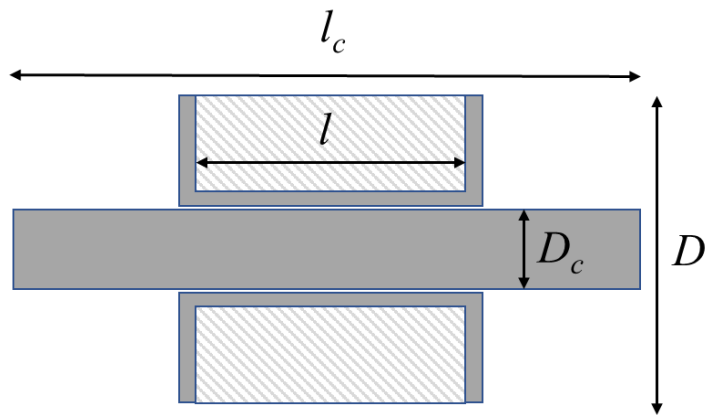


Figure 2.3 Size of a typical ferromagnetic core for a coil sensor ( $l_c$  - core length,  $l$  - sensor length,  $D_c$  - core diameter,  $D$  - sensor diameter).

The detectivity of the sensor is limited by thermal noise

$$V_T = 2\sqrt{k_B \cdot T \cdot \Delta f \cdot R} \quad [V] \quad (1.5)$$

which depends on the resistance  $R$  [ $\Omega$ ] of the winding, the temperature  $T$  [K], the frequency band  $\Delta f$  [Hz], and the Boltzman constant  $k_B = 1.38 \cdot 10^{-23}$  [ $WsK^{-1}$ ].

This type of sensor, being symmetrical with respect to its axis, has five degrees of freedom, and it does not provide information about the roll angle. To overcome the lack of information related to the roll angle, two coil sensors are often used, in orthogonal configuration in order to cancel the mutual inductance,

### 2.2.3 Modeling the Transmitting Coils of the FG

The magnetic field produced by the FG can be obtained by considering the transmitting coils as magnetic dipoles, since the wavelength of the generated magnetic fields is higher than the considered tracking volume. Hence, the magnetic moment produced by the  $i$ -th transmitting coil can be expressed as a function of coil characteristics and excitation signal [26]–[28]

$$\begin{aligned} \mathbf{m}_{tx,i} &= m_{tx,i} \hat{\mathbf{n}}_{tx,i}, \\ m_{tx,i} &= N_{tx,i} S_{tx,i} I_{ti}, \\ S_{tx,i} &= \pi r_{tx,i}^2 \end{aligned} \tag{1.6}$$

where  $\hat{\mathbf{n}}_{tx,i}$  is the versor orthogonal to the surface  $S_{tx,i}$  of the  $i$ -th coil, and  $r_{tx,i}$ ,  $N_{tx,i}$  and  $I_{ti}$  denote the coil radius, the number of turns and the RMS value of the excitation current, respectively. In FG design, both same size and current were considered for all transmitting coils, but due to uncertainty in system parameters, small differences were observed in real quantity values. Indeed, these parameters are indicated with subscript  $i$  in the following formulas to take into account the mismatch between coils.

The RMS magnetic field generated by the  $i$ -th transmitting coil in a generic point  $\mathbf{p}_s = [x, y, z]^T$  is [26]–[28]

$$\begin{aligned} \mathbf{B}_i(\mathbf{p}_s, I_{ti}) &= B_{ix} \hat{\mathbf{x}} + B_{iy} \hat{\mathbf{y}} + B_{iz} \hat{\mathbf{z}} = \\ &= \frac{\mu_0}{4\pi} \frac{m_{tx,i}}{d_i^3} [3(\hat{\mathbf{n}}_{tx,i} \cdot \hat{\mathbf{n}}_{d,i}) \hat{\mathbf{n}}_{d,i} - \hat{\mathbf{n}}_{tx,i}] \end{aligned} \tag{1.7}$$

where  $d_i = |\mathbf{d}_i|$ , with  $\mathbf{d}_i = \mathbf{p}_s - \mathbf{p}_{tx,i}$  represents the vector distance between  $\mathbf{p}_s$  and the center  $\mathbf{p}_{tx,i}$  of the  $i$ -th transmitting coil, and  $\hat{\mathbf{n}}_{d,i}$  is its associated versor.

By considering a homogeneous magnetic flux on the surface of sensing coil  $S_s$ , it is possible to evaluate the induced voltage in the  $i$ -th coil by means of the following expression

$$\tilde{v}_i = 2\pi f_i N_s S_s \mathbf{B}_i \cdot \hat{\mathbf{n}}_s \quad (1.8)$$

where  $N_s$  is the number of coil sensor turns and  $\hat{\mathbf{n}}_s = [\cos(\alpha_s) \cos(\beta_s), \sin(\alpha_s) \cos(\beta_s), \sin(\beta_s)]^T$  is the versor orthogonal to the sensor surface (Figure 2.4).

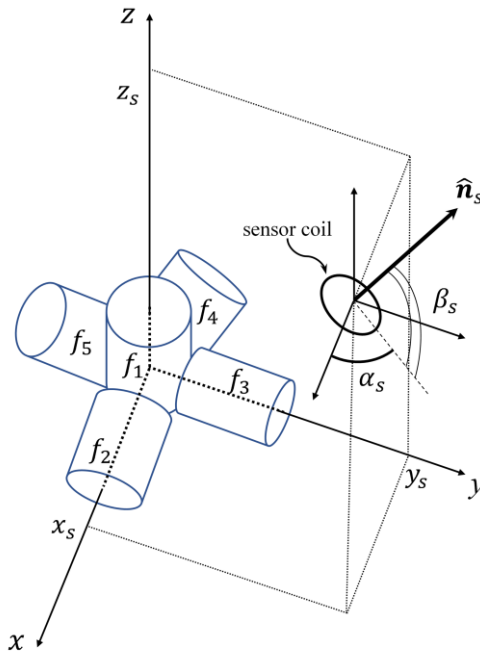


Figure 2.4 FG reference system. Image source: [29].

It is important to consider crosstalk effects due to mutual induction among the transmitting coils. Hence, the crosstalk matrix was calculated [30]

$$\mathbf{C} = \begin{bmatrix} 1 & C_{12} & \cdots & C_{1n} \\ C_{21} & 1 & \cdots & C_{2n} \\ \vdots & \vdots & \ddots & \vdots \\ C_{n1} & C_{n2} & \cdots & 1 \end{bmatrix} \quad (1.9)$$

where  $C_{ij} = \frac{I_{ij}}{I_{jj}}$  is the crosstalk coefficient which is defined as the ratio between the current  $I_{ij}$  in the  $j$ -th coil induced at frequency  $f_i$  and excitation current  $I_{jj}$  in the  $j$ -th coil at the frequency  $f_j$ , considering a generic FG with an arbitrary number  $n$  of transmitting coils. (1.8) can be rewritten in the following way

$$\tilde{v}_i = 2\pi f_i N_s S_s \sum_{j=1}^n C_{ij} \mathbf{B}_j \cdot \hat{\mathbf{n}}_s \quad (1.10)$$

which takes into account the magnetic fields at the same frequency  $f_i$  induced in all transmitting coils by the  $i$ -th coil.

We can rewrite (1.10) in matrix notation:

$$\tilde{\mathbf{v}} = \begin{bmatrix} \tilde{v}_1 \\ \vdots \\ \tilde{v}_n \end{bmatrix} = \mathbf{CAB}\hat{\mathbf{n}}_s = \mathbf{H}\hat{\mathbf{n}}_s \quad (1.11)$$

where

$$\mathbf{A} = \begin{bmatrix} \alpha_1 & 0 & \cdots & 0 \\ 0 & \alpha_2 & \cdots & 0 \\ \vdots & \vdots & \ddots & \vdots \\ 0 & 0 & \cdots & \alpha_n \end{bmatrix} \quad (1.12)$$

is the  $R^{n \times n}$  matrix of sensor sensitivities at each frequency, with  $\alpha_i = 2\pi f_i N_s S_s$ , and

$$\mathbf{B}(\mathbf{p}_s) = \begin{bmatrix} B_{1x} & B_{1y} & B_{1z} \\ \vdots & \vdots & \vdots \\ B_{nx} & B_{ny} & B_{nz} \end{bmatrix} \quad (1.13)$$

is the  $R^{n \times 3}$  matrix of the generated magnetic fields. It is convenient to define  $\mathbf{H} = \mathbf{AB}$ .

# *Chapter 3*

---

## *System Overview and Performance Analysis<sup>1</sup>*

In order to meet the need of accurate long-range tracking systems for surgical navigation, MASMEC Biomed company (Italy), in collaboration with Polytechnic of Bari, has developed an innovative EMTS to be integrated in Imaging Guided Surgery (IGS) systems, to overcome the main limitations of commercial EMTSs in medical use, enhancing the state-of-the-art by increasing the tracking volume, thus obtaining accurate estimation of sensor pose beyond 0.5 m from the FG [28], [29], [32], [33].

In Section 3.1, the basic working principle of the prototype of EMTS is described, and the experimental setup for its characterization is illustrated. Section 3.2 describes several improvements with respect to a previous version of the system, which led to enhanced system performances in terms of noise level reduction. In Section 3.3 several tests are performed on the system to assess the performance in terms of signal repeatability and drift, and their effect on position repeatability is quantified in Section 3.4, along with a comparison with the Aurora system, which represents the state of the art of commercial EMTSs. Finally, conclusions are drawn in Section 3.5.

---

<sup>1</sup> This Chapter is based on papers [31] and [32].

### 3.1 Prototype of the realized EMTS

The system has been carefully presented and partially characterized in [31], [33], [34], where the position of the sensor was reconstructed using triangulation and the piecewise linear interpolation technique.

It is composed of three main components:

- a magnetic field generator (FG).
- a small coil sensor (Aurora – NDI) [35], which has sizes of 0.9 mm diameter and 12 mm length.
- a control unit for data acquisition and signal processing, as shown in Figure 1a.

The system architecture is shown in Figure 3.1: the signals produced by a signal generator are amplified by means of five OPA 544 (Texas Instruments), providing the excitation currents for the five transmitting coils. The whole AC magnetic flux induces a voltage in the magnetic sensor, dependent on the position and the orientation of the sensor; the induced voltage is then digitalized and filtered through five Butterworth band-pass filter with bandwidth of 50 Hz, obtaining five RMS voltage components,  $V_i$ ,  $i = 1, \dots, 5$ , relating to the different excitation frequencies. These components are then used for the estimation of sensor pose by means of a suitable reconstruction algorithm. The sampling parameters are listed in Table 3.2.

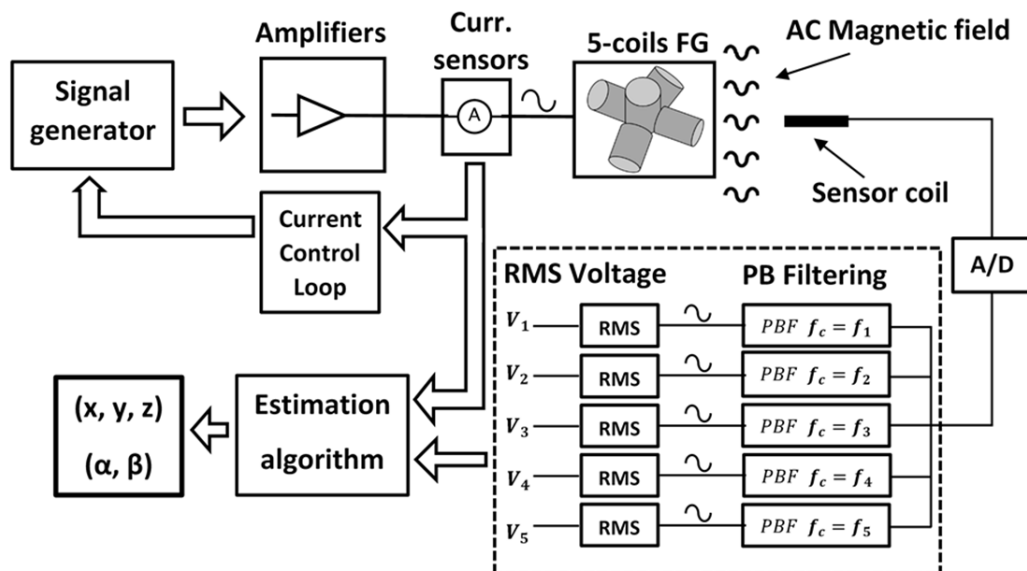


Figure 3.1 Principle of operation of the developed EMTS. Image source: [29].

The experimental setup used to assess system performance, is shown in Figure 3.2. It consists of *i*) the FG prototype, *ii*) the Aurora coil sensor, *iii*) a MELFA RV-2FB-D robot (by Mitsubishi) having a position repeatability error of 0.02 mm [36] for the movement of the magnetic sensor along a user defined trajectory, and *iv*) the data acquisition (DAQ) system. The DAQ system, based on PXI technology, is composed of the following devices, inside a NI PXIe-1065 chassis: *i*) a NI PXI-4461 (24 bit) is used for the acquisition of the induced voltage; *ii*) a NI PXI-6052E (16 bit, with a maximum sampling rate of 333 kS/s.) is used for the acquisition of the five excitation currents; *iii*) a NI PXI-6713 is used for the generation of current signals. The devices employed for data acquisition (DAQ) and signal conditioning are listed in Table 3.1. The sampling frequency of the DAQ devices is set to 50 kHz, with 2500 samples/s for each channel, hence RMS voltage components, and consequently the sensor pose estimate, are updated with a frequency of 20 Hz (see [32] for details about data acquisition devices and parameters), which is adequate for many surgical navigation procedures.

Table 3.1 DAQ and signal conditioning devices.

Device	Description
<b>NI PXIe-1065</b>	Chassis which contains the devices for DAQ system
<b>NI PXI-4461</b>	24-bit device for acquisition of sensor induced voltage
<b>NI PXI-6713</b>	16-bit device for the generation of current signals
<b>NI PXI-6052E</b>	16-bit device for acquisition of signals from current sensors
<b>LA 55-P (LEM)</b>	Hall effect sensors for measurement of excitation currents
<b>OPA 544 (AD)</b>	Power amplifiers for the generation of the excitation currents.

A suitable control software, developed in LabVIEW<sup>®</sup> (by National Instruments Corp.), manages the DAQ system and the movement of the robot, it allows to perform automatic tests and measurements, it provides real-time parameters to monitor the system state, and it allows the storing of the data sets for subsequent offline processing for performance analysis; LabVIEW is largely used to control and monitor industrial equipment and processes and for the creation of test and measurement systems [37]–[39].

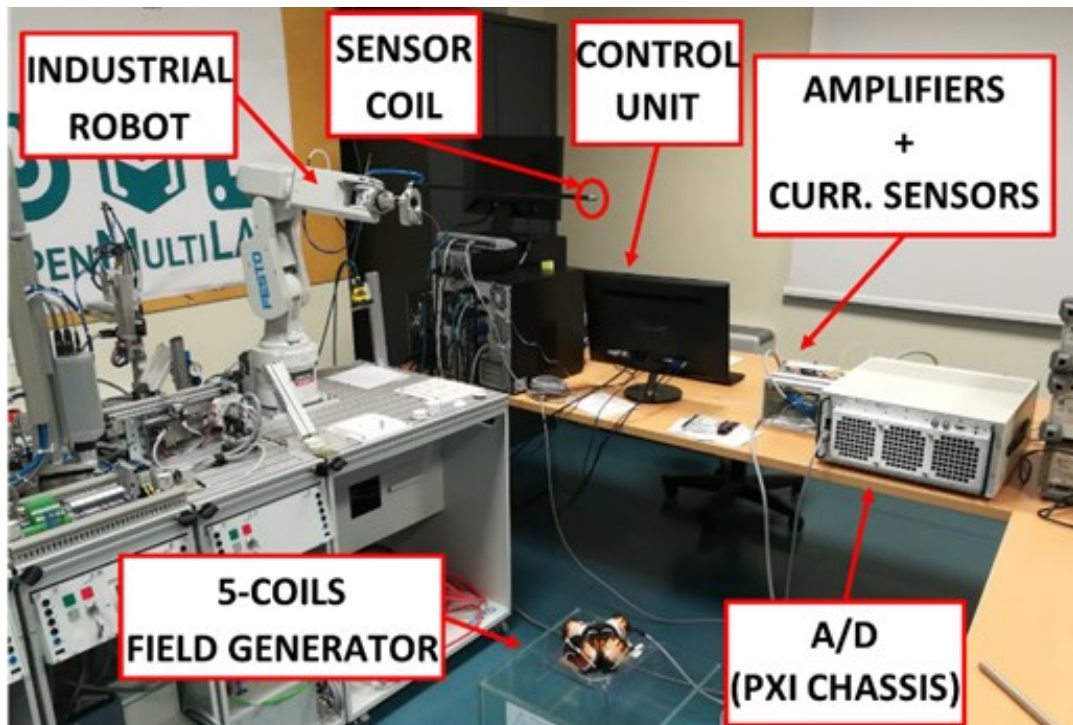


Figure 3.2 Experimental setup for system characterization. Image source: [40].

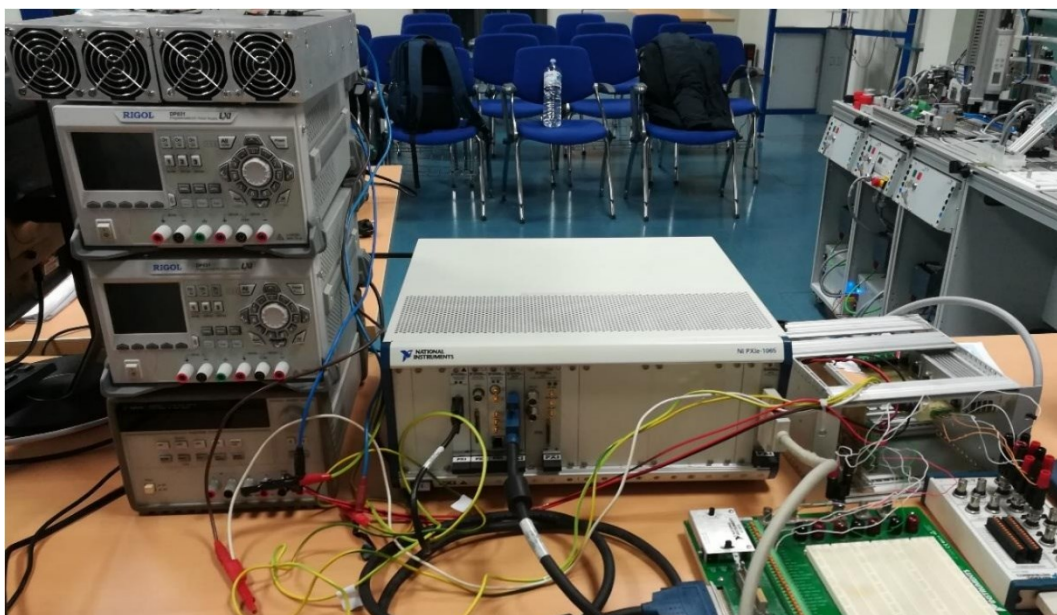


Figure 3.3 - Experimental setup: hardware DAQ based on PXI technology for signal acquisition and generation.

### 3.1.1 Field Generator

The FG consists of a support base of plastic material, to avoid EM interference, on which five transmitting coils are arranged in space along five different directions, such as to minimize crosstalk effects due to mutual inductances and to maximize the area covered by the generated magnetic field, as shown Figure 3.4. Three coils are arranged orthogonally to each other, directed along the three Cartesian axes; the other two are orthogonal to each other and inclined by  $45^\circ$  with respect to the support plane (Figure 3.4).

Each coil has total length of 50 mm, internal radius of 17 mm, external radius of 27 mm, and 315 turns. The transmitting coils are simultaneously powered by sinusoidal currents at different frequencies  $f_i, i = 1, \dots, 5$ , in the range of 1 kHz - 5 kHz, with a gap of about 1 kHz, according to the Frequency Division Multiplexing (FDM) technique, thus generating five AC magnetic fields. FDM enhances the use of time resources and does not require a synchronization device, unlike Time Division Multiplexing (TDM).

According to the IEEE Standard C95.1-2005 [41], [42], which defines the security levels for human exposure to electromagnetic fields, the amplitude of the total generated magnetic field must not exceed the limit value of 0.2 mT. Hence, all coils parameters (such as length, internal and external radiuses and turns number) were designed accordingly, and excitation currents in each coil were limited to 1 A rms, as detailed in [34]. In this way, the threshold of 0.2 mT was respected from a distance of about 15 cm from the center of the field generator.

The selected excitation currents must assure the generation of a magnetic field measurable in points far from the FG, up to 1 m. Hence, a power factor (PF) correction capacitor is connected in series to each coil in order to work in resonance conditions; in this way it is possible to generate fields of high intensity with a low power absorption, using lower currents [43]. The capacitance  $C_i$  of the single PF correction capacitor is obtained by reversing the formula:

$$f_{i_{ris}} = \frac{1}{2\pi\sqrt{LC_i}}$$

where  $f_{i_{ris}}$  is the desired resonance frequency and  $L$  is the transmitting coil inductance ( $\approx 6.2$  mH). The actual capacities of the PF correction capacitors differ from those calculated by eq. (2.1), so a shift of the resonance frequencies is obtained. In addition, due to the skin effect, each transmitting coil presents a different resistance, due to the different frequencies used for FDM technique: as the frequency increases, the current

density is greater on the surface of the conductor, causing an increase of coil resistance. Table 2.1 shows the resonance frequencies and resistances for each excitation channel.

*Table 2.1 - Resonance frequencies and resistors of each coil.*

Nominal frequency [kHz]	$f_{ris}$ [Hz]	$\text{Re}\{Z(f)\}$ [ $\Omega$ ]
1	972.5	1.83
2	2057.5	2.39
3	3070	3.31
4	3700	4.60
5	4750	6.25



*Figure 3.4 Arrangement of the five coils. Image source: [31].*

A current control loop was developed to stabilize the magnetic field amplitude and to avoid errors in position estimation due to magnetic field variations, mainly due to thermal and electric drift [44] of transmitting coils and electronics of the FG. RMS current values in each coil,  $I_i$ ,  $i = 1, \dots, 5$ , are measured by means of five Hall effect sensors (LA 55-P - LEM). Moreover, to furtherly improve current stability, the current in the  $i$ -th coil is filtered, choosing the component  $I_{ii}$  at the frequency  $f_i$  as feedback variable, as detailed in [31]. This ensures more stability and reduces drift effects.

### 3.1.2 Coil Sensor

The AC magnetic field generated by the FG is measured by means of a coil sensor, of the type described in Section 2.2.2, small enough to ensure its insertion into surgical instruments and sufficiently sensitive to magnetic fields of reduced intensity. In particular, a 5 DoF (Degrees-of-freedom) coil sensor was used, produced by NDI (No. 610057) and designed for the Aurora system, but also integrable in other systems. It is a shielded sensor, very robust to interference, with a nominal resistance of  $83 \Omega$ . The frequency response of the sensor is linear in the range 1-30 kHz, with a sensitivity of about  $0.1142 \frac{V}{T \cdot Hz}$  [45].

During the experiments presented in this dissertation, the sensor was placed inside a 3D printed PLA (Polylactic acid) housing. PLA is derived from plant substances and does not generate interference when immersed in the magnetic field. The housing is then inserted on the end of a carbon fiber bar with a length of about 50 cm. The other end is attached to the end effector of an industrial robot used for the movement of the sensor; thanks to the length of the bar, the interference caused by the robot is highly reduced.

## 3.2 Hardware Development

An experimental setup was developed and described in [31] to characterize the system. In this Section, the setup has been carefully examined, leading to new developments, in order to reduce the measurement noise.

### 3.2.1 Coherent Sampling

The voltage from the coil sensor is sampled and processed in not overlapping observation windows. Leakage errors in the acquisition of periodic signals can be reduced by performing a coherent sampling; where the observation window must contain an integer number of signal cycles. First, let us define the following parameters for the acquisition section:

- Sampling Frequency:  $f_s = 60 \text{ kHz}$ ;
- Samples in the observation window:  $N_s = 3000 \text{ samples}$ ;
- Update Frequency for RMS values calculation:  $f_{\text{update}} = f_s / N_s = 20 \text{ Hz}$ ;
- Update period:  $T_{up} = 1 / f_{up} = 50 \text{ ms}$ ;
- Frequency and period of the  $i$ -th, coil, with  $i = 1, \dots, 5$ :  $T_i = 1 / f_i$ .

Table 3.2 Sampling parameters.

Parameter	Value
Sampling frequency	$f_s = 50$ kHz
Number of samples in the observation window	$N_s = 2500$ samples
Update frequency for RMS values calculation	$f_{up} = f_s/N_s = 20$ Hz
Update period	$T_{up} = 1/f_{up} = 50$ ms

The following condition ensures coherent sampling:

$$T_{up}/T_i = f_i/f_{up} = k \quad (3.1)$$

where  $k$  is integer. Hence  $f_i$  must be a multiple of 20 Hz and, considering also the resonance condition for each coil, the frequencies listed in Table 3.3 were used in FG signal generation.

Table 3.3 Frequencies used for FG signal generation to obtain synchronous sampling.

Coil	Frequency (Hz)
1	980
2	2060
3	3060
4	3680
5	4740

### 3.2.2 DAQ Synchronization

In [31], the impact of spectral leakage errors has been shown, and remedial actions have been performed. However, by analyzing the spectrum of the currents flowing in the transmitting coils, spectral leakage was still observed. This phenomenon was also observed in the time domain: the rms current value was affected by a periodic oscillation, whose frequency increased with signal frequency. A careful analysis has led us to identify this error as a result of non-coherent sampling. Indeed, even though the signal frequencies

were chosen according to their coherent sampling condition, the DAQ device was not able to sample at the proper frequency, due to its finite resolution, causing a frequency mismatch. Moreover, there was a clock mismatch between the generation and the acquisition devices. Hence, we finely tuned the sampling frequency, still maintaining the coherent sampling condition, and synchronized the time bases of the generation and acquisition devices through the routing of the clock signal. Finally, we set the sampling frequency  $f_s = 50$  kHz and the number of samples per channel  $N_s = 2500$ . The results show an improved field stability of more than 4 times, with standard deviations of about 0.007% of the FG current of 1 A rms.

### 3.2.3 Analysis of the Electronic Board

The NI PXIe-1065 (National Instrument, Austin, TX, USA) chassis has been configured with two boards for the generation and acquisition of signals: the analog output device produces five signals, which are amplified by five OPA 544 (Analog Devices, Norwood, MA, USA) and power the transmitting coils; the analog input device is used to acquire the signal from the coil sensor and the five transmitting current signals by means of Hall effect sensors LA 55-P (LEM International SA, Plan-les-Ouates, Switzerland).

Experimental results have highlighted a conductive coupling effect due to common power and ground returns, adding noise to the measurement of the sensor's induced voltage. To avoid this effect, separated power and ground returns have been provided, reducing the voltage noise by more than 6 dB.

### 3.2.4 Improved DAQ Devices

In the previous experimental setup, a NI PXI-6052E (National Instrument, Austin, TX, USA) device with 16-bit resolution and low noise was used to acquire both the sensor voltage and the current sensors signal. Due to the low amplitude of induced voltage, an INA 114 was used to amplify the signal.

Experimental tests have shown that the instrumentation amplifier provides noise in the measurement process. In order to reduce this effect, a 24-bit DAQ device (NI PXI-4461) (National Instrument, Austin, TX, USA) was used for the acquisition of the voltage induced on the coil sensor, allowing for the removal of the amplifier. It presented an input range of  $\pm 0.316$  V<sub>pk</sub> at 30 dB gain, with a LSB (least significant bit) of about 38 nV, more than 80 times lower than the PXI-6052E.

### 3.2.5 Cable's Shielding

With the aim of evaluating the noise floor of the acquiring device, the voltage measured on the sensor with the FG turned off was also acquired.

In this case, the voltage noise is mainly due to Johnson noise having power spectral density (PSD) given by  $4kTR$ . By considering  $T = 296$  K and  $R = 80 \Omega$  (corresponding to the resistance of coil sensor), noise power density is  $-179$  dB/Hz, or  $1.14$  nV/ $\sqrt{\text{Hz}}$ .

The noise PSD of the PXI-4461 is  $-162$  dB/Hz, or  $8$  nV/ $\sqrt{\text{Hz}}$ . Therefore, when the sensor is connected to the analog input channel with FG turned off, a noise floor of about  $-162$  dB/Hz should be measured. Instead, experimental results showed a value of about  $-145$  dB/Hz. Consequently, there was an error source that increased the measurement noise.

In order to reduce noise, proper shielding was considered. Careful experimentation showed that using a shielded cable of about 2 m to connect the coil sensor to the DAQ device, the best results are obtained by connecting the cable shield to the chassis ground with a short wire, taking care to make the path as short as possible. This has allowed to reduce the noise floor to  $-162$  dB/Hz, as expected.

## 3.3 Performance Analysis

### 3.3.1 Induced Voltage Repeatability

To analyze the effect of the improvements discussed in Section 3.2, the same experimental tests executed in [20] have been performed, and the obtained results have been compared.

The FG was supplied with currents of 1 A rms for each channel, and two baselines for sensor positioning were defined, respectively at 0.7 m and 1 m from the FG, along the  $z$ -axis of the reference system (Figure 3.5). For each position, 200 measurements of the five rms voltage components  $V_i$ , as well as the rms currents  $I_i$ ,  $i = 1, \dots, 5$ , were executed, and the mean  $\bar{V}_i$  and standard deviation (SD)  $\sigma_{v_i}$  were calculated. The sampling frequency,  $f_s = 50$  kHz, was selected, and  $N_s = 2500$  samples were acquired; therefore, the rms values were updated with a frequency  $f_{up} = \frac{f_s}{N_s} = 20$  Hz, which is the minimum rate appropriate for surgical navigation. The measurements have been performed keeping the sensor oriented along the  $x$ -axis, parallel to the coil powered at  $f_2$ .

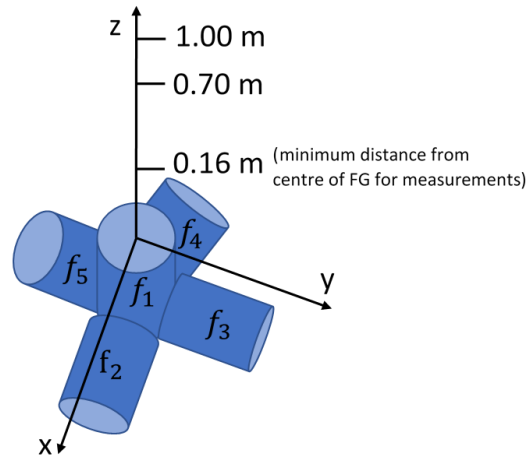


Figure 3.5 Coordinate system with reference to the field generator (FG). Image source: [32].

Since the INA 114 instrumentation amplifier has been removed in the new hardware development, the magnitudes of the induced voltages were different. Hence, to correctly compare the effect of hardware changes, the relative SD values were considered, defined as:

$$\sigma_{v,rel_i} = \frac{\sigma_{v_i}}{\bar{V}_i} \quad (3.2)$$

Table 3.4 lists the relative SD of the induced voltage, at 0.7 m and 1 m, obtained before and after the hardware improvement. An overall noise reduction of about 70% for almost all channels can be observed. Moreover, it can be observed that some channels present a relative SD significantly lower than others. In particular, the first and third channels present higher values, due to the coupling between the coil sensor and each transmitting coil, which depends on sensor orientation and transmitting coils arrangement, which affect mutual induction and the concatenated magnetic flux.

Table 3.4 Relative SD of the induced voltage at 0.7 m and 1 m from FG, before and after hardware improvement, and their relative reduction. Results are expressed as percentage.

	Distance (m)	$f_1$	$f_2$	$f_3$	$f_4$	$f_5$
<b>Before improvement</b>	<b>0.7</b>	19.75	0.15	1.53	0.08	0.11
	<b>1.0</b>	13.90	0.40	6.95	0.19	0.31
<b>After improvement</b>	<b>0.7</b>	1.13	0.04	1.06	0.03	0.03
	<b>1.0</b>	3.03	0.13	1.09	0.10	0.07
<b>Relative reduction</b>	<b>0.7</b>	94	73	31	62	72
	<b>1.0</b>	78	68	84	47	77

### 3.3.2 Induced Voltage Drift

The current which flows in each transmitting coil causes the heating of the coil, with consequent variations of coils resistance which result in magnetic field amplitude variations. Hence, for each coil, a current control loop has been implemented [31], to keep the magnetic field amplitude stable over time. The control system is based on the use of the five Hall effect sensors LA 55-P, to measure the current in each transmitting coil.

Despite the current control system, experiments have shown a significant drift of voltage components, as shown in Figure 3.6, representing the voltage values acquired in 82 min, after a system warm-up of about 30 min, with the sensor placed in a fixed position at 0.7 m along the z-axis.

It can be noticed that, after about 50 min, the first three channels seem to converge, whereas the fifth starts to decrease and the fourth channel is still increasing. Therefore, it is not possible to predict how the drift will affect the system.

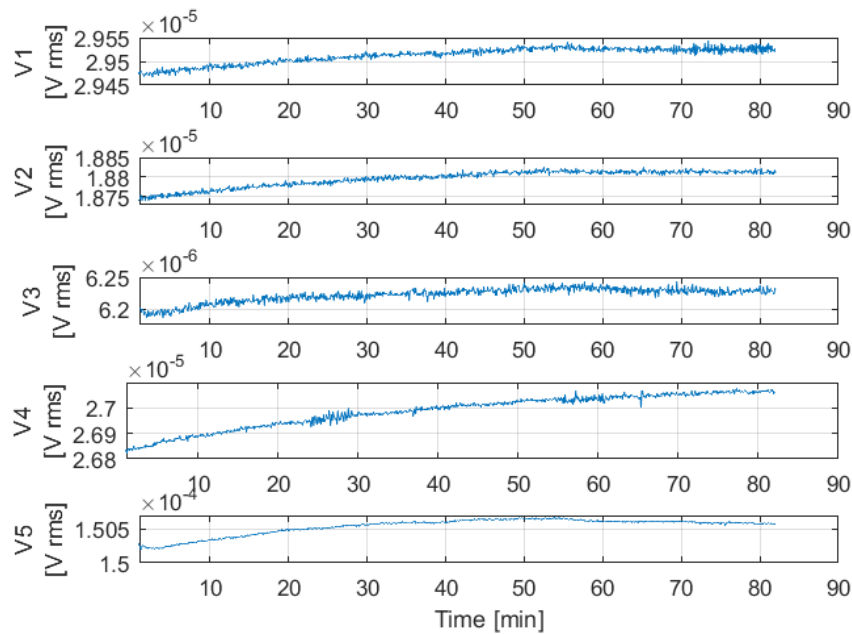


Figure 3.6 Voltage drift vs time; current loop turned on. Image source: [32].

To investigate the cause of the drift phenomena, additional voltage acquisitions have been performed. The current control loop was turned on, employing  $I_i$  as regulated variable [Appendix A], and only one channel has been powered with a current of 1 A rms, keeping the other channels turned off. A multimeter, model HP 34401A, has been inserted in series with the active transmitting coil, to provide a reference measurement of the excitation current. The acquisition started after a zero warm-up time.

Figure 3.7 shows the comparison between the current measured with the Hall effect sensor and with the multimeter, related to the third transmitting coil. We can observe that the current measured with the Hall effect sensor converges after a very short time, while the current measured with the multimeter drifts over time.

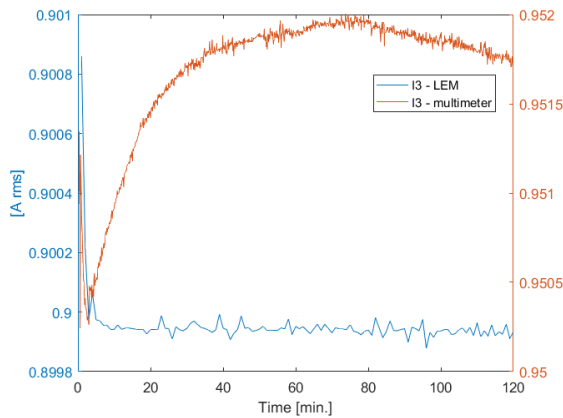


Figure 3.7 Current measured with a Hall effect sensor and with a multimeter – channel 3.

Image source: [32].

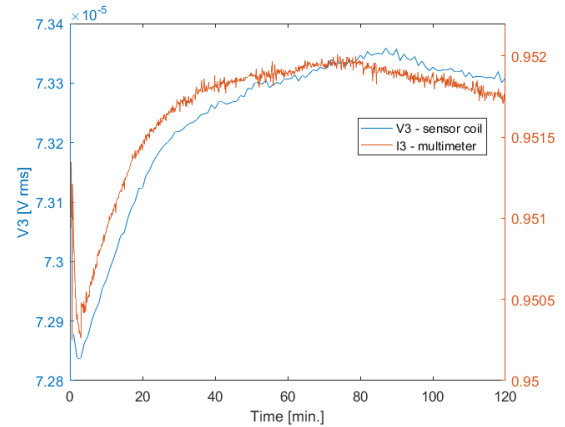


Figure 3.8 Voltage induced in the coil sensor and current measured with a multimeter –channel 3.

Image source: [32].

In Figure 3.8 we can observe that there is a correlation between the voltage drift of the coil sensor and the current drift of the field generator measured by the multimeter, which present similar behavior. We can therefore assume that the drift is due either to the Hall effect sensor, or the shunt resistor at its output, or both. In fact, the control loop varies the excitation current, in order to keep constant the current measured with the Hall effect sensor, which is affected by drift errors; hence, the measured current is stable, while the actual current drifts over time, causing a drift of the induced voltage.

In order to quantify and reduce the voltage drift, several experiments have been executed. In particular, five acquisitions have been performed, which differ in the choice of the regulated variable for the current control loop [Appendix A]. For each acquisition, the sensor has been sequentially placed in six positions by means of the robotic arm, at different distances from the FG, from about 250 mm to 750 mm along the  $z$ -axis. The voltage drift is higher when the sensor is closer to the FG, so it is important to quantify it as the distance varies. For each position,  $M = 100$  measurements of the induced voltage have been performed, and the mean value was computed to reduce the noise. Each acquisition has been executed for a period of 120 minutes, starting after a zero warm-up time. The results have shown that the drift was approximately the same at all distances, in percentage terms. Moreover, the system performed better when choosing  $I_t'''$  as regulated variable [Appendix A], because the voltage drift reached a stable value for all channels, within 0.03%, 0.50%, 0.10%, 0.25% and 0.01% of the final value, respectively, after a warm-up time of about 50 min.

### 3.3.3 Excitation Currents Noise Quantification

Noise in excitation currents affects magnetic field stability and, consequently, system performance in terms of pose estimation. As shown in Figure 3.1, a current control loop was developed to improve magnetic field amplitude stability; for this aim the RMS currents which flow in each coil,  $I_i$ ,  $i = 1, \dots, 5$ , are measured by means of five Hall effect sensors (LA 55-P - LEM). Moreover, the stability of the magnetic field was improved further by filtering the current powering the  $i$ -th coil and selecting the component  $I_{ii}$  at the frequency  $f_i$  as a feedback variable (see [31] for details).

Figure 3.9 show the excitation currents for each transmitting coil, in a period of 101 s, and the standard deviation (std) calculated in non-overlapped windows of 1 s (containing 20 measurements each). In this Section we simulate and analyze the effect of excitation currents noise on the total noise of sensor voltage measurement, by employing a model of the magnetic field.

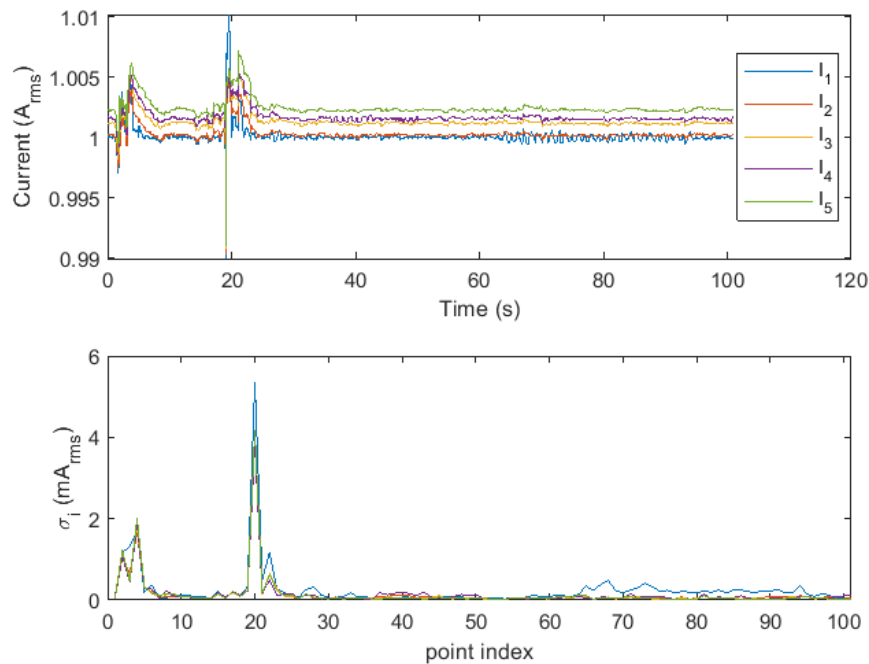


Figure 3.9 Excitation current and std of each transmitting coil. Image source: [29].

## 3.4 Validation

Validation tests were carried out to evaluate the performance of the proposed system in terms of the repeatability of the sensor position estimation. The results were obtained by means of the post-processing of the acquired data, and not in real-time.

### 3.4.1 Repeatability Error Evaluation through Gradients

To evaluate the repeatability error, the standard deviation of repeated measurements of the sensor position  $\mathbf{r} = [x, y, z]^T$  was calculated. The magnetic sensor measured the generated magnetic field, returning five rms components, denoted as  $\mathbf{v} = [v_1, \dots, v_5]^T$ . These were affected by errors, assumed to be uncorrelated, with diagonal covariance

$$\mathbf{C}_v = \begin{bmatrix} \sigma_{v_1}^2 & \dots & 0 \\ \vdots & \ddots & \vdots \\ 0 & \dots & \sigma_{v_5}^2 \end{bmatrix} \quad (3.3)$$

The position standard deviation  $\sigma_r = [\sigma_x, \sigma_y, \sigma_z]^T$  can be calculated by the propagation of the voltage standard deviation  $\sigma_v = [\sigma_{v_1}, \dots, \sigma_{v_5}]^T$ , as follows.

Let  $\mathbf{g} = [g_1, g_2, g_3, g_4, g_5]^T: X \subseteq \mathbb{R}^3 \rightarrow \mathbb{R}^5$  be the function relating  $\mathbf{r}$  and  $\mathbf{v}$ :

$$\mathbf{v} = \mathbf{g}(\mathbf{r}) \quad (3.4)$$

Relation (3.4) is sampled experimentally by placing the sensor on a regular grid of  $N_p$  points  $\mathbf{r}_i, i = 1, \dots, N_p$ , obtaining voltages  $\mathbf{v}_i$ .

The variation of  $\mathbf{g}(\mathbf{r})$  in the neighborhood of a point  $\mathbf{r}_i$  can be evaluated by means of the gradients  $\nabla \mathbf{g}_j(\mathbf{r}_i)$ , defined as:

$$\nabla \mathbf{g}_j(\mathbf{r}_i) = \left[ \frac{\partial g_j}{\partial x}(\mathbf{r}_i), \frac{\partial g_j}{\partial y}(\mathbf{r}_i), \frac{\partial g_j}{\partial z}(\mathbf{r}_i) \right]; \quad (3.5)$$

$$j = 1..5, i = 1..N_p$$

The partial derivatives are estimated experimentally by the ratios  $\frac{\Delta v_j}{\Delta x}$ ,  $\frac{\Delta v_j}{\Delta y}$  and  $\frac{\Delta v_j}{\Delta z}$ , by assuming small variations in the sensor position.

Then, the Jacobian matrix  $\mathbf{J}_g(\mathbf{r}_i) \in \mathbb{R}^{5 \times 3}$  can be calculated, defined as:

$$\mathbf{J}_g(\mathbf{r}_i) = \begin{bmatrix} \nabla \mathbf{g}_1(\mathbf{r}_i) \\ \dots \\ \nabla \mathbf{g}_5(\mathbf{r}_i) \end{bmatrix}. \quad (3.6)$$

To evaluate the relation between small changes of  $\mathbf{r}$  and  $\mathbf{v}$ , it is useful to linearize (3.4), obtaining

$$\mathbf{v} \simeq \mathbf{g}(\mathbf{r}_i) + \mathbf{J}_g(\mathbf{r}_i)(\mathbf{r} - \mathbf{r}_i) \quad (3.7)$$

We can invert (3.7) by means of the Moore–Penrose pseudoinverse of the Jacobian matrix,  $\mathbf{J}_g^+(\mathbf{r}_i) \in R^{3 \times 5}$ , in order to estimate  $\mathbf{r}$  from  $\mathbf{v}$ :

$$\mathbf{r} \simeq \mathbf{r}_i + \mathbf{J}_g^+(\mathbf{r}_i) (\mathbf{v} - \mathbf{v}_i). \quad (3.8)$$

By using (3.8), the position covariance  $\mathbf{C}_{r_i}$  can be calculated from the covariance of voltage components,  $\mathbf{C}_{v_i}$ :

$$\mathbf{C}_{r_i} \simeq \mathbf{J}_g^+ \mathbf{C}_{v_i} \mathbf{J}_g^{+T} \quad (3.9)$$

Finally, the variance of position coordinates can be found on the diagonal of  $\mathbf{C}_{r_i}$ , after substituting (3.3) into (3.9):

$$\sigma_{r_i}^{\circ 2} \simeq \mathbf{J}_g^+(\mathbf{r}_i)^{\circ 2} \sigma_{v_i}^{\circ 2} \quad (3.10)$$

where  $\circ$  is the Hadamard power operator, and  $\circ 2$  denotes the element-wise square. The square root of  $\sigma_{r_i}^{\circ 2}$  obtained in (3.10) allows to estimate the standard deviation of each coordinate.

It should be noted that the obtained result can be applied to any position reconstruction algorithm, as long as it can be linearized for error propagation purposes.

The same method can be applied to estimate the effects of the residual drift of voltage measurements, by means of (3.8).

### 3.4.2 Test Protocol and Position Repeatability Estimation

A suitable test protocol was defined to evaluate the system performance in a wide operating volume.

Preliminary experiments were executed to evaluate the repeatability of the system for three different sensor orientations, with its axis aligned along the  $x$ -,  $y$ -, and  $z$ -axis of the reference system of Figure 3.5, evaluating the repeatability in several positions along the  $z$ -axis.

In particular, for each sensor orientation, the sensor has been placed in five locations along the  $z$ -axis, 100 mm apart, at a range of about 150 to 550 mm from the FG. For each position, 100 voltage measurements have been performed, and the mean and standard deviation have been computed. Moreover, for each position, the voltage gradients (3.5) have been calculated as finite differences between the mean voltage measured at  $\mathbf{r}_i$  and the ones measured at a small distance of 5 mm moving along the  $x$ -,  $y$ - or  $z$ -axis, separately. Then, we obtained five different Jacobian matrices and the correspondent components of the pseudoinverse matrices  $\mathbf{J}_g^+(\mathbf{r}_i)$ , for each sensor orientation. Afterwards, the position SD has been estimated by means of (3.10). The results are shown in Figure 3.10. It can be noted that the repeatability changes as the orientation varies.

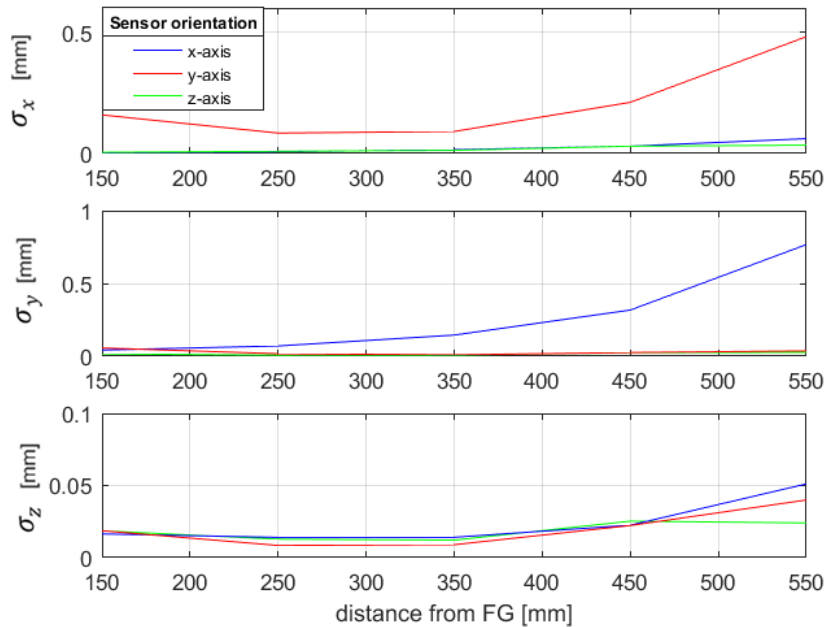


Figure 3.10 Position repeatability obtained with the estimation through gradients for different orientations of the sensor—EMTS prototype. Image source: [32].

In a subsequent analysis, the repeatability error of a single sensor orientation was studied at more positions over the range, to investigate the effect of the distance from the field generator on the position repeatability. In particular, a middle orientation has been chosen, so that the axis of the sensor formed an angle of  $-30^\circ$  in the  $xz$ -plane; in this case, it was possible to approach the condition where the orientation provided worse repeatability.

The sensor was placed in 55 different points along the  $z$ -axis, with a step of 10 mm, in the range of about 160 to 700 mm from the FG. The same test protocol of previous experimental tests was applied, thus obtaining 55 different Jacobian matrices and the corresponding components of the pseudoinverse matrices  $\mathbf{J}_g^+(\mathbf{r}_i)$ , shown in Figure 3.11.

Basically, each component of  $\mathbf{J}_g^+(\mathbf{r}_i)$  represents the system sensitivity of a position coordinate when each voltage component changes.

Afterwards, the position SD was estimated by means of (3.10). The test has been executed after a warm-up time of 1 hour. The obtained results, shown in Figure 3.12, show low position repeatability errors along the  $x$ -,  $y$ - and  $z$ -axis, of about 0.2 mm, within the limit suitable for surgical navigation, of about 1–2 mm in several applications [13], [46]. Moreover, it can be noticed that the position standard deviation increased with the distance from the FG, as was expected, since the amplitude of the magnetic fields, the gradients and the signal to noise ratio of the sensor output were lower at a greater distance from the FG. This was also confirmed by the increasing behavior of the pseudoinverse observed in Figure 3.11. Indeed, its dependence on position allows one to evaluate, at different distances, the sensitivity of the position error to measurements errors on each channel. For example, channel 1 exhibited a lower sensitivity to errors overall. These considerations may be useful to assess the performance of the transmitting coil of the FG relevant to each channel, which is affected by its distance from the coil sensor. This aspect will be discussed in detail in Chapter 4.

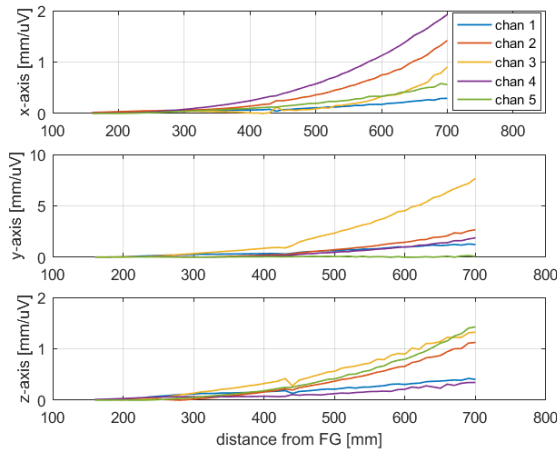


Figure 3.11 Elements of the pseudoinverse of the Jacobian matrix vs distance from the FG.  
Image source: [32].

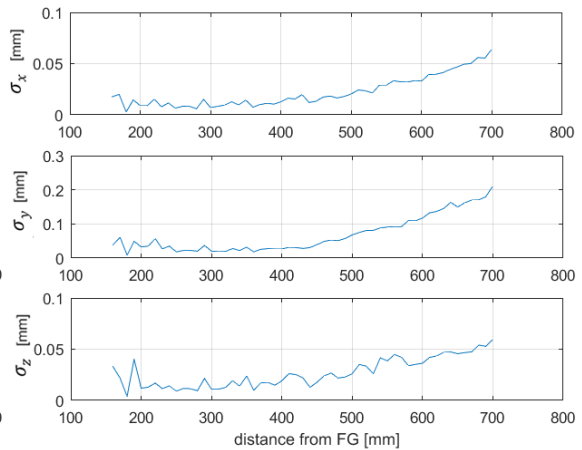


Figure 3.12 Position repeatability obtained with the estimation through gradients.  
Image source: [32].

Four additional experimental tests have been performed by considering further sensor positions to evaluate the position repeatability in a larger working volume, as shown in Figure 3.13. The obtained results are similar to the ones presented in Figure 3.12.

For example, Figure 3.14 shows the SD for  $(x, y) = (0, -250)$  mm, obtained by varying the  $z$  coordinate on the trajectory labeled “acq. 2” in Figure 3.13.

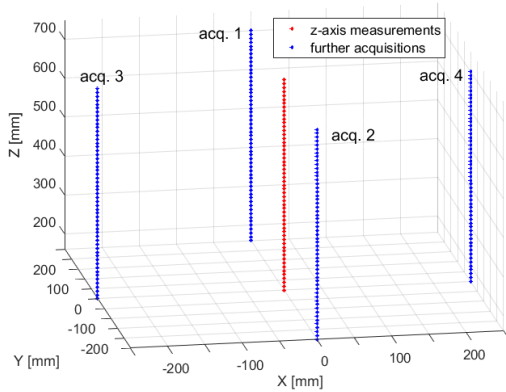


Figure 3.13 Sensor positions of four additional experimental tests. The red points represent the sensor position of first acquisition where all points lie on the z-axis. Image source: [32].

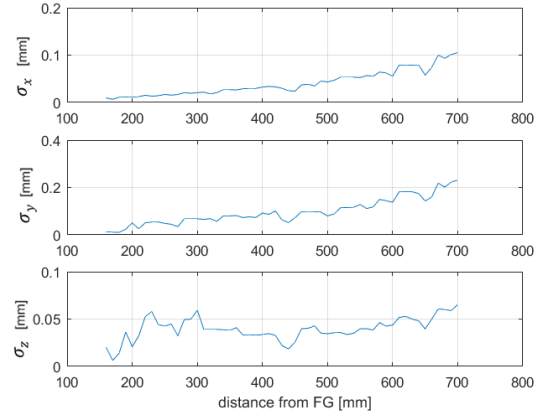


Figure 3.14 Position repeatability obtained with the estimation through gradients for the trajectory labeled "acq. 2". Image source: [32].

### 3.4.3 Analysis of Voltage Drift

In order to quantify the effect of the drift on the system accuracy, we repeated, after 90 min, the experimental test described in Section 3.4.2, keeping the whole system turned on. Then, the voltage differences between the two sets of experiments,  $\Delta v_i = [\Delta v_{1i}, \dots, \Delta v_{5i}]^T$ , have been measured in each of the 58 points, for each channel, and the position errors  $\mathbf{e}_{r_i} = [e_{x_i}, e_{y_i}, e_{z_i}]^T$  have been estimated by means of (3.8), where  $\mathbf{J}_g^+(\mathbf{r}_i)$  are the same as those calculated in Section 3.4.2.

Figure 3.15 shows the position error contribution given by the residual drift of the voltage measurements and is the result of (3.8) and the values of the elements of the pseudoinverse of the Jacobian matrix, which are shown in Figure 3.11. These array elements represent the sensitivity of the position error and repeatability to the errors of the voltage components, such as drift and noise. It can be observed that the position errors are of the order of 0.3 mm, meeting the specifications required for surgical navigation in many applications [13], [46].

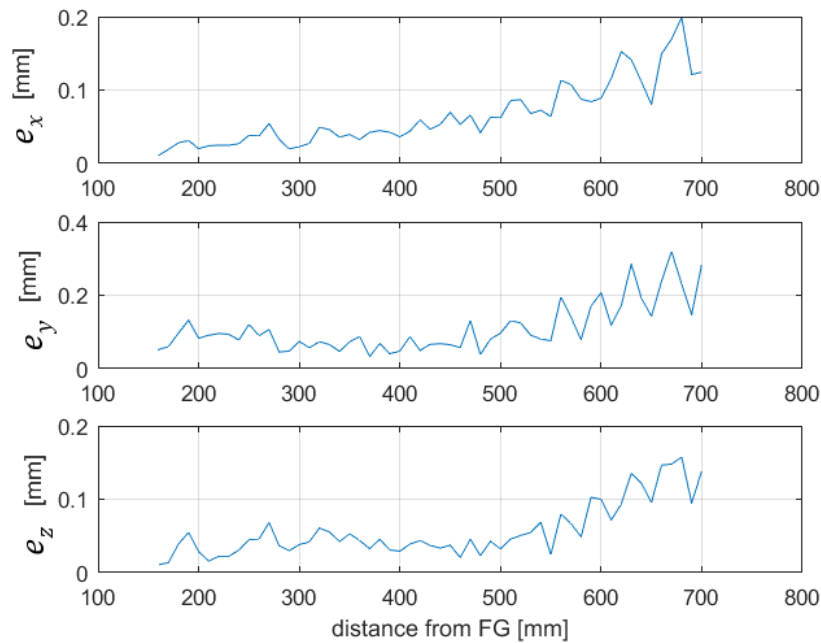


Figure 3.15 Position errors caused by drift, obtained by repeating the same measurements after 90 min and applying the estimation through gradients. Image source: [32].

### 3.4.4 Comparison with the State of the Art: the Aurora system

Aurora systems (NDI) are the most used EMTSs in surgical navigation. To compare the repeatability error of the proposed system with the state of the art, the same experimental tests described in Section 3.4.2 have been performed by using the Aurora PFG 20-20 system [47]. This system consisted of: i) a Planar Field Generator, ii) a Sensor Interface Unit that amplifies and digitizes the electrical signals from the sensors, iii) a System Control Unit that controls the FG, collects information from the Sensor Unit Interfaces, calculates the position and orientation of each sensor and interfaces with the host computer, iv) a Five DoF (Degrees of Freedom) electromagnetic sensor.

The Five DoF sensor has been placed in 51 points along the z-axis of the PFG 20-20, with a distance ranging from about 160 to 660 mm, which is the maximum distance from the FG indicated in the Aurora specifications. Figure 3.16 shows the SD of 100 measurements at each distance, obtained with both Aurora and the proposed system. It can be observed that the repeatability errors of the Aurora system are one order of magnitude greater than the ones obtained with the proposed system. Of course, different results could be obtained when applying a position reconstruction algorithm instead of the proposed error propagation method, as will be shown in Section 5.3; still, these results

are valuable and provide an indication of the effect of some error sources on position estimation, leading to identify spatial regions where repeatability is higher than others.

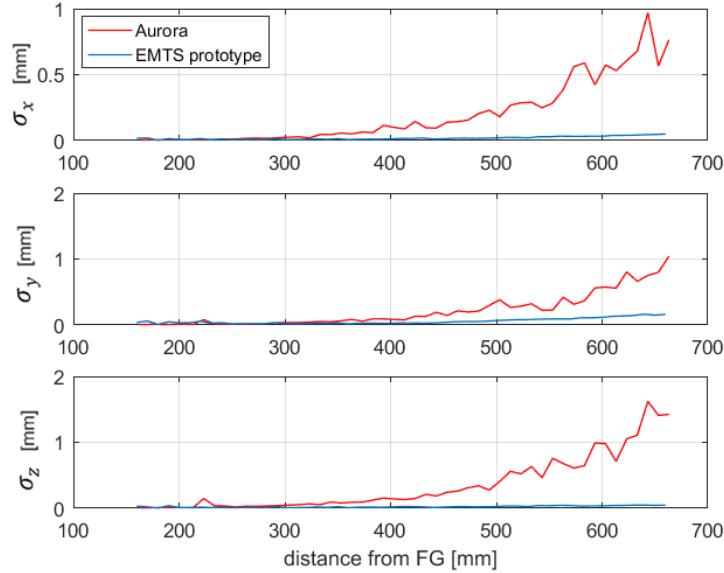


Figure 3.16 Comparison between the SD of the Aurora system and the EMTS prototype. Image source: [32].

Moreover, further measurements have been performed, according to the sensor positions indicated in Figure 3.13, to explore a larger volume. The results obtained in these new positions confirm the ones presented in Figure 3.14, as can be seen, for example, in Figure 3.17, which shows the repeatability on the trajectory labeled “acq. 2”.

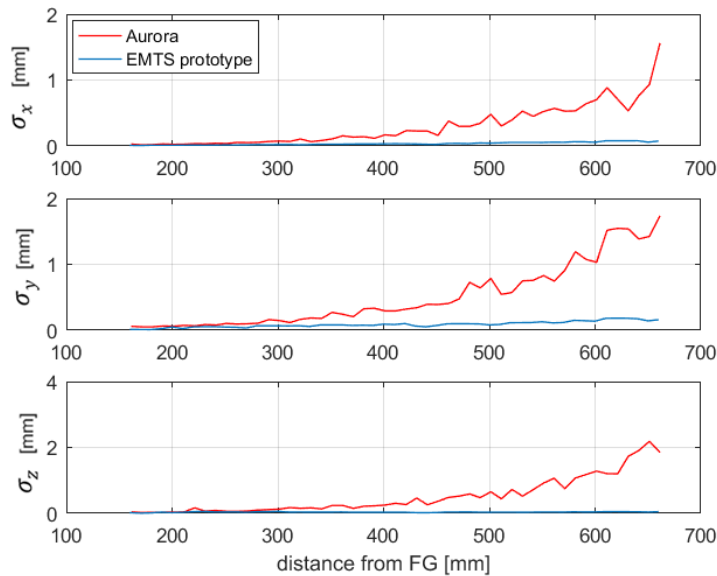


Figure 3.17 Comparison between the SD of the Aurora system and the EMTS prototype obtained along the trajectory “acq. 2”. Image source: [32].

### 3.4.5 Effect of Excitation Currents Noise

Several error sources contribute to sensor voltage noise. Main contributors considered in this study are the measurement and acquisition noise  $\sigma_{acq}$ , and the FG repeatability error  $\sigma_B(\mathbf{p}_s, \mathbf{I}_{tx})$  due to current noise  $\sigma_I$ , where  $\mathbf{I}_{tx}$  is the  $n \times 1$  vector containing the excitation currents.

We assume that they both contribute independently to the sensor voltage noise  $\sigma_v$ , so we can write:

$$\sigma_v = \sqrt{\sigma_B^2 + \sigma_{acq}^2} \quad (3.11)$$

From the model described in Section 2.2.3, it is clear that the magnetic field, and consequently the induced voltage, linearly depends on excitation currents; hence, current noise contributes to voltage noise, and this contribution increases when the sensor is closer to the FG. In fact,  $\sigma_{acq}$  is approximately the same in the whole working volume, since it depends on the measurement devices and on the Johnson noise of the sensor, whereas  $\sigma_B$  depends on sensor pose and excitation currents. In Section 3.3.1 we quantified the acquisition noise by obtaining  $\sigma_{acq} \cong 20 \text{ nV}$  on each channel.

Figure 3.18 shows the noise contribution  $\sigma_B$  in some points of the tracking volume, obtained by applying the dipole model and considering a current noise  $\sigma_I = 0.07 \text{ mA}$  for the 1<sup>st</sup> coil, as obtained from experimental data, and with the sensor aligned along  $z$ -axis. It can be noted the increasement of noise near the FG. It must be said that, beyond 400 mm, the noise is lower than 22 nV, which is comparable with the measurement noise  $\sigma_{acq} = 20 \text{ nV}$ . Hence beyond 400 mm the noise produced by the current noise is quite negligible, instead when the sensor is closer to the FG, magnetic field noise reaches higher values. The same considerations can be made for the other transmitting coils. Hence, to obtain an accurate estimation of sensor pose, it is important to compensate this effect (as will be shown in Section 5.4).

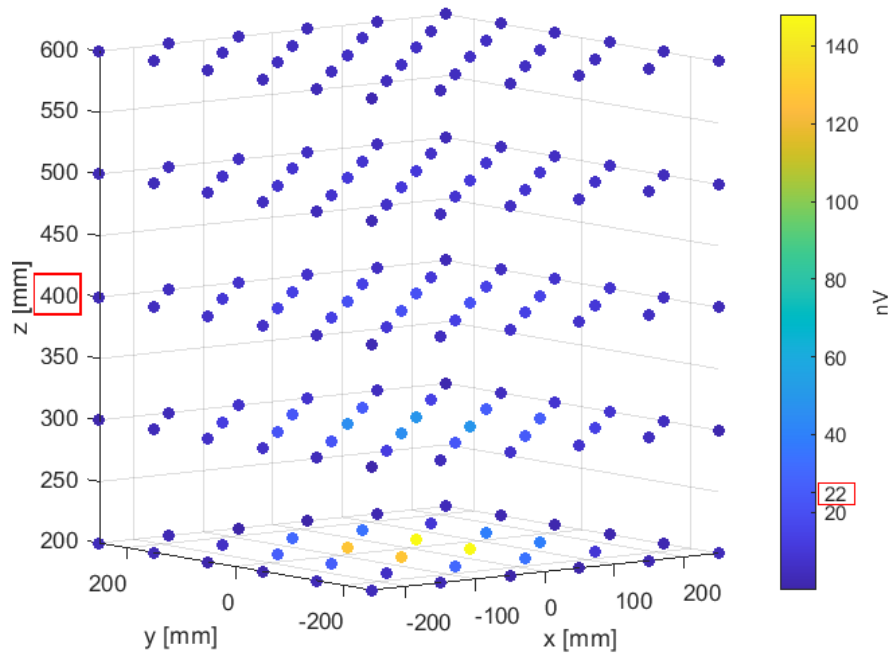


Figure 3.18  $\sigma_B$  obtained by simulated data, considering a current noise  $\sigma_I = 0.07 \text{ mA}$  in the 1st coil – sensor aligned along z-axis. Image source: [29].

### 3.5 Chapter Conclusions

In this Chapter we illustrated a method to evaluate the repeatability of electromagnetic tracking systems, and we applied it to a prototype of EMTSs that has been developed with the purpose of overcoming the limitation of current commercial systems, providing an accurate tracking of surgical tools far from the field generator.

We presented the experimental setup used to characterize the system, by defining a test protocol based on employing a high repeatability industrial robotic arm to move the sensor, thus providing accurate position references.

Several hardware improvements have been described, which led to enhanced system performances in terms of noise level reduction in both signal generation and in the measurement process, as shown by experimental tests. The analysis of experimental results has highlighted the presence of drift in voltage components, whose effect has been quantified and related to the variation of the sensor position. The repeatability error in sensor position estimation has been evaluated through the propagation of the voltage measurement error, at different distances from the FG, from about 160 mm to 700 mm, and the performances have been compared with results obtained from the tests executed on the Aurora system, obtaining SD values lower than 0.2 mm at 700 mm from the FG.

## Chapter 3

The analysis methodology is based on the experimental measurement of field gradients, on the evaluation of coil sensor voltage noise and drift, and on the linear approximation of the voltage-position relation, which lead to an error propagation formula. The proposed analysis has the advantage of relating the overall system performance to that of identifiable components which can be separately analyzed and optimized, on the one hand, and compared among different EMTSs, on the other.



# Chapter 4

---

## *FG Configuration Analysis from Magnetic Field Gradients<sup>2</sup>*

Performance assessing and measurement accuracy estimation are crucial phases in device characterization and different methods were developed for accurate uncertainty evaluation [50], [51]. In EMTSs used in surgical navigation, particular importance is devoted to evaluation of position repeatability error evaluation. In Chapter 3, several system improvements have been discussed in order to increase the repeatability of the induced voltage. In fact, voltage repeatability significantly affects systems performance in estimating sensor position. Hence, it is important to quantify the effect of the voltage repeatability error on position RMS error.

In Section 3.4.1 it was assumed that the orientation of the sensor does not change. Actually, the  $j$ -th transmitting coil generates an AC magnetic field at the frequency  $f_j$ , whose RMS value can be expressed in the reference system of Figure 2.4 as

$$\begin{aligned} \mathbf{B}_j &= B_{j_x} \hat{\mathbf{x}} + B_{j_y} \hat{\mathbf{y}} + B_{j_z} \hat{\mathbf{z}} \\ j &= 1, \dots, 5 \end{aligned} \tag{4.1}$$

---

<sup>2</sup> This Chapter is based on papers [48] and [49].

The MS returns a voltage proportional to the concatenated magnetic flux, which varies with the orientation; so, for different orientations of the sensor, different gradients are obtained, leading to different position RMS error. Hence, it is important to evaluate the position RMS error as the orientation changes.

In this Chapter,  $B_{j_x}$ ,  $B_{j_y}$ ,  $B_{j_z}$  are individually evaluated by orienting the MS along x-, y-, z-axis respectively, so that the concatenated flux is only due to the magnetic field component directed along the given axis.

This Chapter is structured as follows. In Section 4.1 the protocol for the assessment of position repeatability error and the experimental tests performed on the system are described, and the results are discussed. Section 4.2 analyses the magnetic field gradient and related them to the position accuracy in the tracking volume. In Section 4.3 the results obtained by applying the magnetic dipole approximation are compared with experimental results of Section 4.2. Finally, conclusions are drawn in Section 4.4.

## 4.1 Assessment of Position RMS Error by using Experimental Data

In order to evaluate the position RMS error through error propagation as described in Section 3.4.1, in this Section three different experimental tests have been performed, in each of which the sensor was oriented according to one of the three axes. For each test, in order to explore a relatively large volume, the sensor has been placed by means of the industrial robot in a regular grid of  $N_p = n_x \cdot n_y \cdot n_z$  points  $\mathbf{r}_i, i = 1, \dots, N_p$ , where  $n_x = 5$ ,  $n_y = 6$ ,  $n_z = 5$  are the number of points along x-, y- and z-axis, respectively, with a step of 100 mm in each direction, for a total of  $N_p=150$  points. The measurement volume is shown in Figure 4.1.

In each point  $\mathbf{r}_i$ ,  $M=100$  measurements of the induced voltage have been performed, and the mean  $\bar{\mathbf{v}}_i = [\bar{v}_{i_1}, \dots, \bar{v}_{i_5}]^T$  and standard deviation  $\sigma_{\mathbf{v}_i} = [\sigma_{v_{i_1}}, \dots, \sigma_{v_{i_5}}]^T$  have been calculated. Afterwards, the partial derivatives (3.5) are estimated experimentally as finite differences  $\Delta v/\Delta x$ ,  $\Delta v/\Delta y$ ,  $\Delta v/\Delta z$ , between the voltage measured at  $\mathbf{r}_i$ , and the ones measured at a small distance of 5 mm moving along the x-, y- or z-axis, separately. All voltage measurements are averaged  $M=100$  in order to reduce the measurement noise.

Finally, the standard deviation (SD) of the position has been estimated by means of (3.10). This method requires  $4 \times N_p$  points for each experiment.

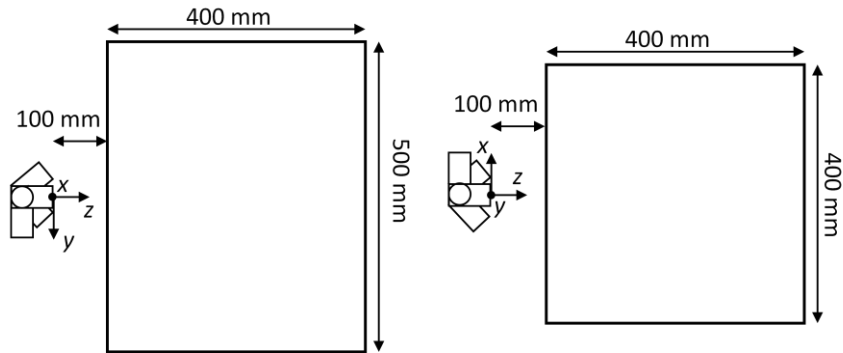


Figure 4.1 Measurement volume. Image source: [48].

### 4.1.1 Results

For each point of the grid, the RMS error, also called mean radial spherical error in the 3D localization context, has been calculated as  $\sigma_{r_i} = \sqrt{\sigma_{x_i}^2 + \sigma_{y_i}^2 + \sigma_{z_i}^2}$ . Figure 4.2, Figure 4.3, and Figure 4.4, show the results for the sensor aligned along x-, y- and z-axis, respectively.

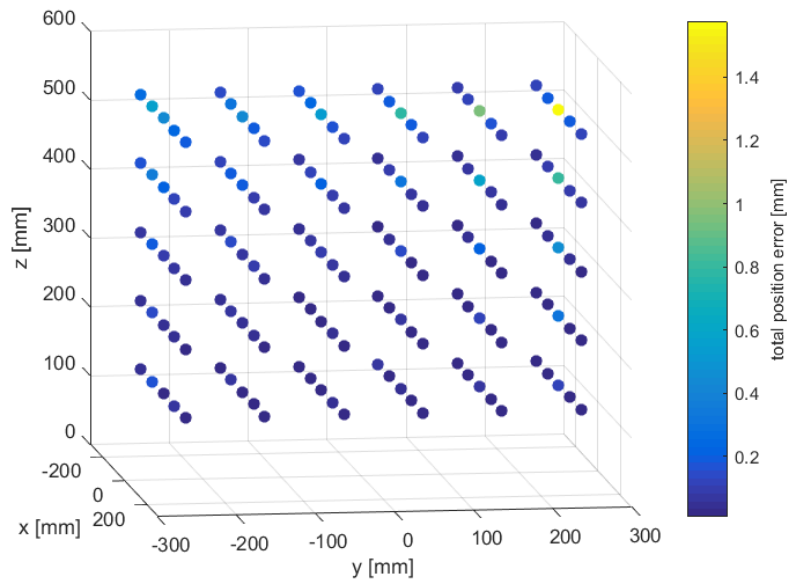


Figure 4.2 Position RMS error with sensor aligned along x-axis. Image source: [48].

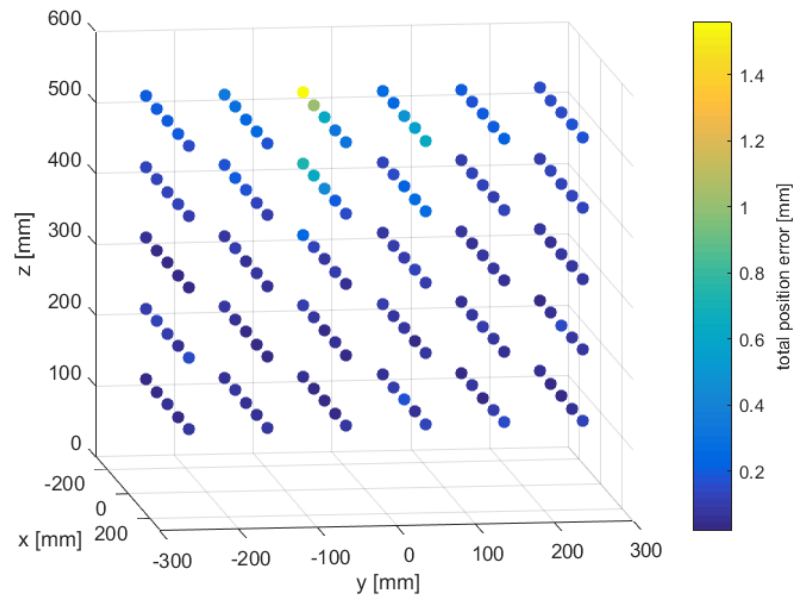


Figure 4.3 Position RMS error with sensor aligned along y-axis. Image source: [48].

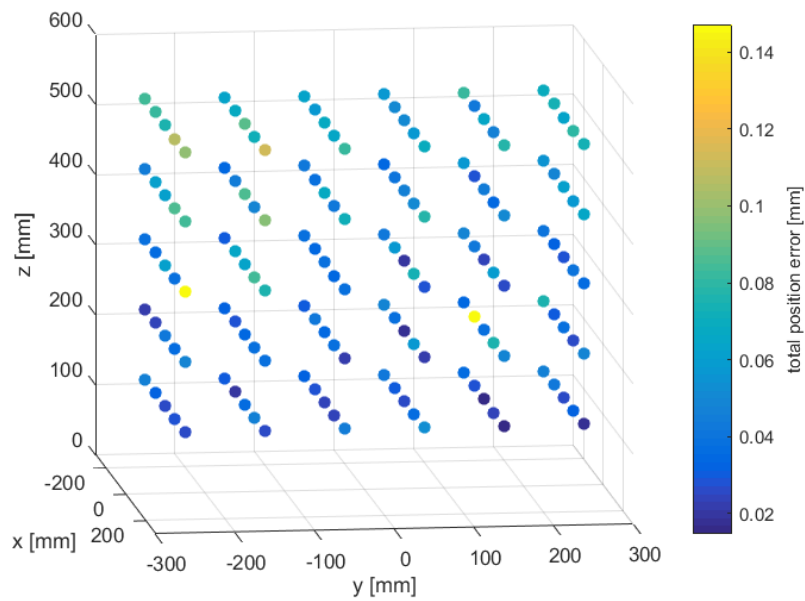


Figure 4.4 Position RMS error with sensor aligned along z-axis. Image source: [48].

It can be noted that, when the sensor is aligned along z-axis, the error is very small throughout the volume, less than about 0.14 mm, while for y-axis and z-axis it is one order of magnitude greater. Moreover, the error increase with the distance from the FG.

Figure 4.5 and Figure 4.7 show the position error versus the point index, separately for each  $z$ -plane, for better visualization. The grid has been scanned by increasing the  $x$ -coordinate, then the  $y$ -coordinate and finally the  $z$ -coordinate; hence, each plane contains  $n_x \cdot n_y = 30$  points.

Figure 4.5 shows the error when the sensor is aligned along  $x$ -axis. It can be observed the presence of peaks, in correspondence of  $x = 0$  mm, i.e., on the plane formed by main axis of coils 1 and 3 (see Figure 3.4), whose amplitude increases as the  $y$ -coordinate increases. In these spatial regions, the voltage gradients are low and the sensitivity to position variation is lower. Moreover, there seems to be a symmetry with respect to the  $yz$ -plane. Similar considerations apply when the sensor is aligned along  $y$ -axis, changing the role of  $x$  and  $y$ , as shown in Figure 4.6, where peaks can be seen in correspondence of  $y = 50$  mm.

Figure 4.7, relevant to a sensor oriented along  $z$ -axis, shows a lower RMS error.

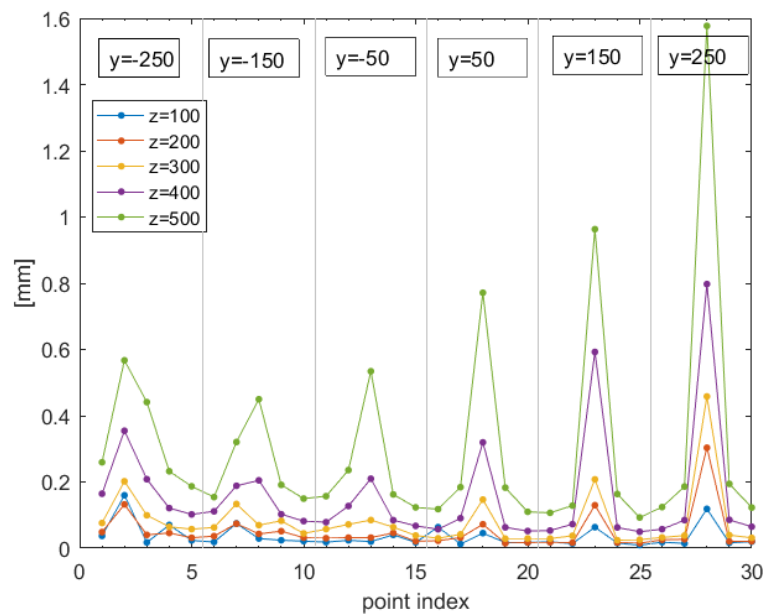


Figure 4.5 Position RMS error with sensor aligned along  $x$ -axis, for each  $z$ -plane. Image source:[48].

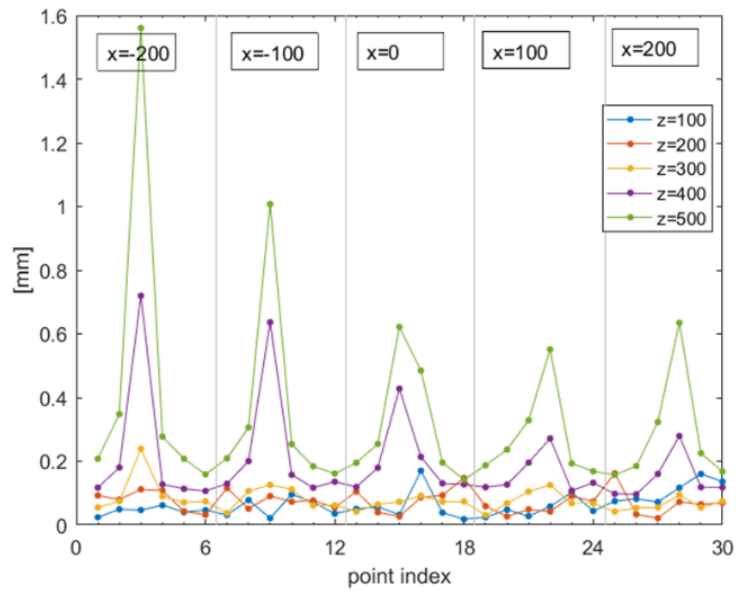


Figure 4.6 Position RMS error with sensor aligned along y-axis, for each z-plane.

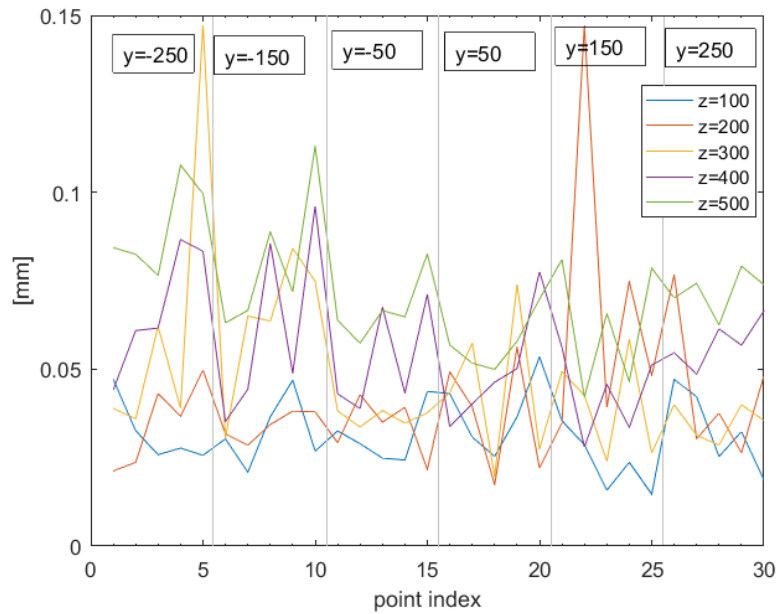


Figure 4.7 Position RMS error with sensor aligned along z-axis, for each z-plane. Image source: [48].

From the above considerations emerges that the position error is higher when the sensor is oriented with its axis on the  $xy$  plane. In order to better understand this behavior, Figure 4.8 shows the  $x$ -,  $y$ - and  $z$ -component of the position RMS error, when the sensor is aligned along  $x$ -axis.

It can be noted that, when the sensor is aligned along  $x$ -axis, the error of the  $y$ -component is higher, whereas the error of the  $x$ -component is lower; vice-versa when the sensor is aligned along  $y$ -axis. The error of the  $z$ -component is very low in both cases. Moreover, here too it can be observed the presence of peaks, in correspondence of  $x = 0$  mm ( $y = 50$  mm) when the sensor is aligned along  $x$ -axis ( $y$ -axis): except for those peaks, RMS error is always  $\leq 0.6$  mm, which is slightly higher than SD values obtained in Section 3.4.2: there, in fact, the sensor was more oriented toward the FG, and not in the  $xy$ -plane thus presenting errors similar to those of Figure 4.7.

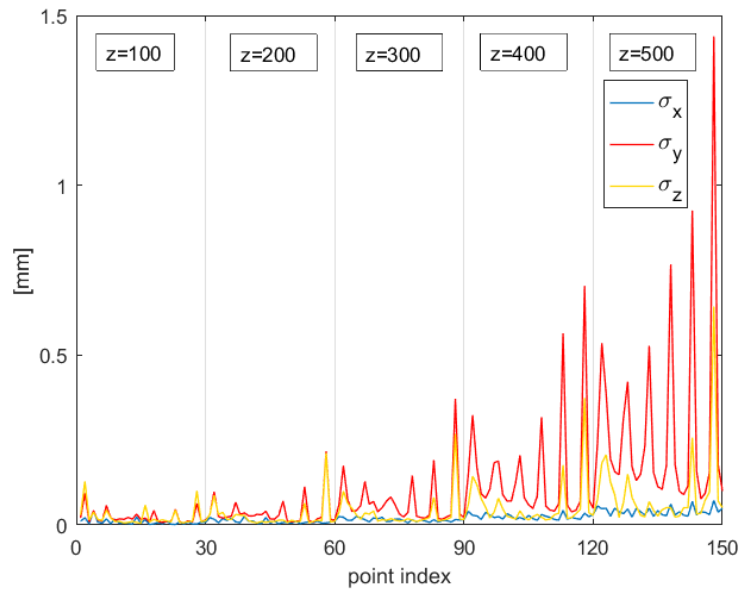


Figure 4.8  $x$ -,  $y$ - and  $z$ -component of the position RMS error with sensor aligned along  $x$ -axis. Image source: [48].

Hence, we can conclude that there are some regions of the space where the position RMS error is lower than others. Moreover, position RMS error is lower when the sensor axis is aligned with the  $z$ -axis of the reference system. This suggests that the system performs better when the sensor is oriented towards the FG.

Overall, the RMS error is quite small and can be compared with the specification required for surgical navigation in many applications [13], [46], [52].

## 4.2 Analysis of Magnetic Field Gradients

The pseudoinverse of the Jacobian matrix introduced in Section 3.4.1 gives important information about what to expect in terms of accuracy in different regions of the tracking volume. From the results of the previous Section 4.1.1, we observed some regions where

the position RMS error is lower than others, as well as the presence of peaks. We believe it depends on the voltage gradients or, equivalently, on the magnetic field gradients, which are represented by the Jacobian matrix and are influenced by the arrangement of the transmitting coils.

In order to investigate this hypothesis, in Figure 4.9, Figure 4.10, and Figure 4.11, the element of the pseudoinverse of the Jacobian matrix are shown for the MS oriented along  $x$ -,  $y$ -, and  $z$ -axis, respectively, thus considering both  $B_x$ ,  $B_y$ , and  $B_z$  components of the magnetic field, whereas in Section 3.4 only one orientation of the sensor was considered. It can be noted that the gradients generally increase when the distance from the FG increase, according to magnetic field model and to previous results. The gradients related to  $B_z$  are much lower than the others, confirming that the increased error obtained for orientation along  $x$ - and  $y$ -axis is due to higher gradients of the magnetic field, rather than to higher voltage noise. By comparing Figure 4.9 and Figure 4.10, a symmetry between the gradients along  $x$ - and  $y$ -axis is observed, in accordance with previous results. Moreover, the peaks shown in previous results can be here related to peaks in the pseudoinverse of the Jacobian matrix.

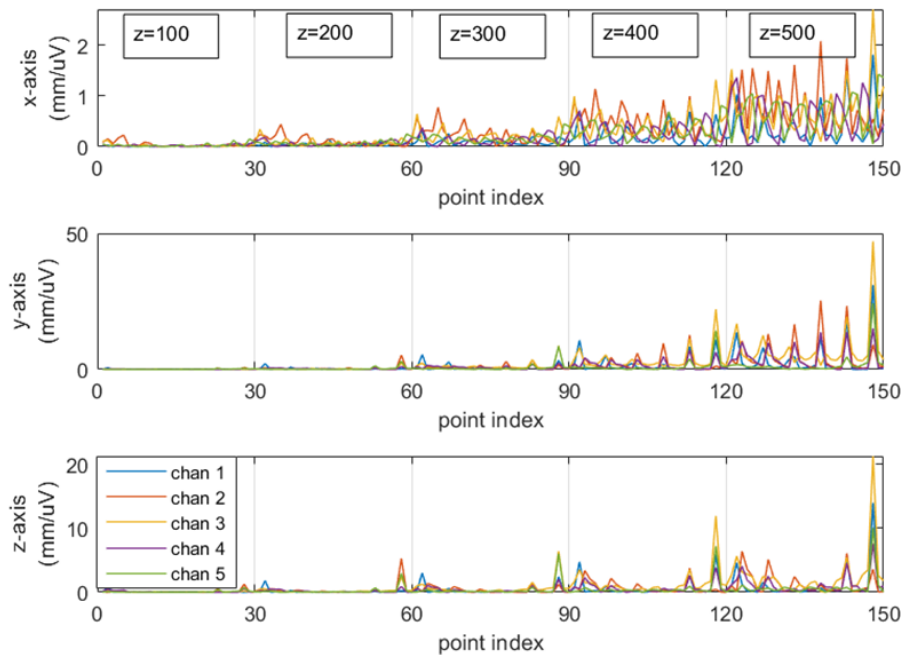


Figure 4.9 Elements of the pseudoinverse of the Jacobian matrix with sensor aligned along  $x$ -axis, thus measuring  $B_x$  component of the magnetic field.

## Chapter 4

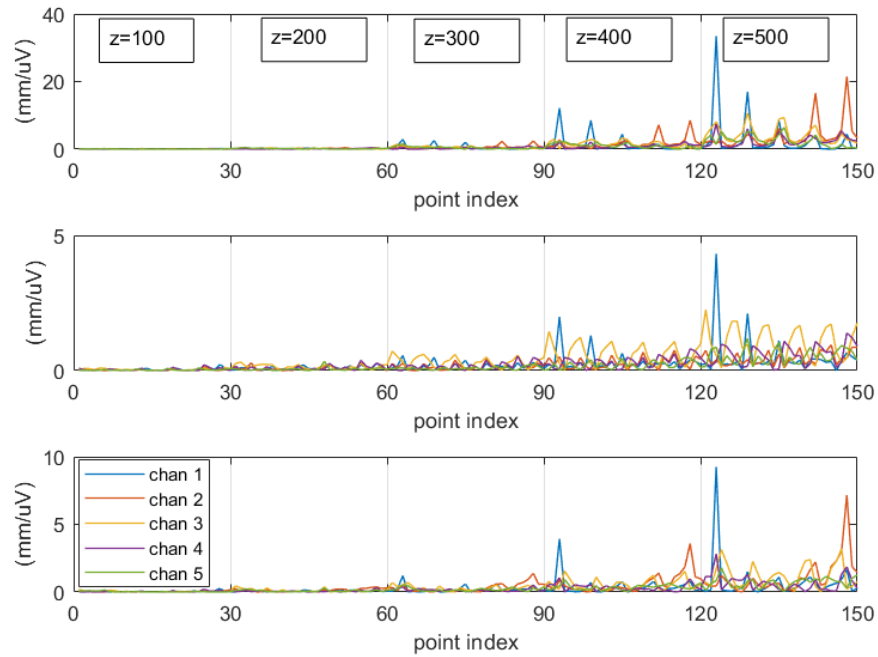


Figure 4.10 Elements of the pseudoinverse of the Jacobian matrix with sensor aligned along y-axis, thus measuring  $B_y$  component of the magnetic field. Point indexes are reshaped: first along x-axis, then along y-axis.

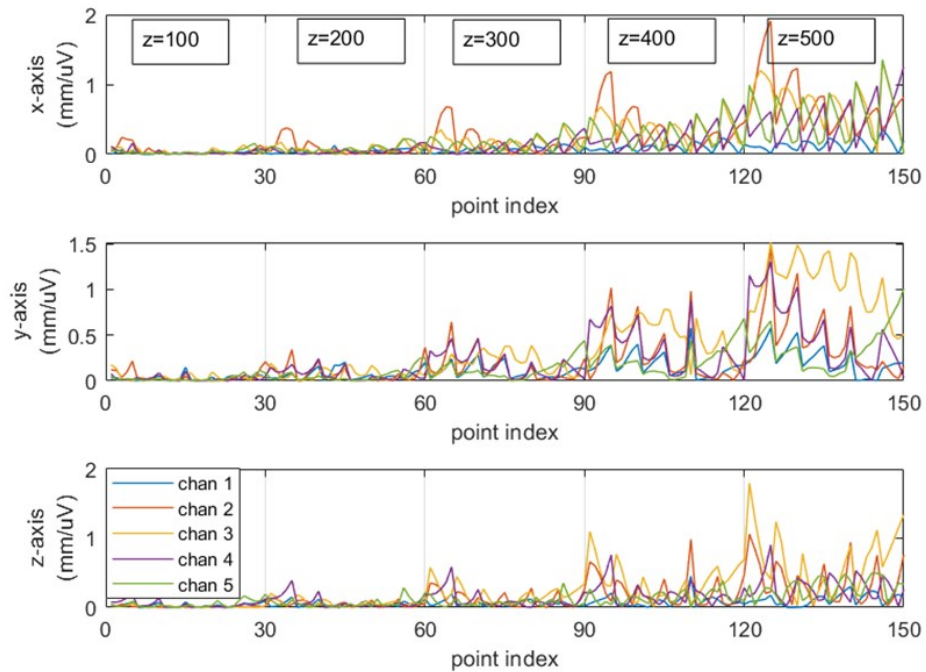


Figure 4.11 Elements of the pseudoinverse of the Jacobian matrix with sensor aligned along z-axis, thus measuring  $B_z$  component of the magnetic field.

### 4.3 Assessment of Position RMS Error by using Magnetic Field Model

In this Section we evaluate the position repeatability error of the system by applying the method described in Section 4.1 and using the magnetic field model proposed in Section 2.2.3 to compute the gradients, instead of estimating them experimentally. The accuracy of the magnetic field model described in Section 2.2.3 depends on the uncertainty of the nominal values of system parameters. To improve the model accuracy the magnetic field model has been fitted by using the experimental data of first test performed in [48]. A set of optimized parameters was obtained by finding minimum of unconstrained multivariable function by using an algorithm based on Nelder-Mead simplex method [53]. The following cost function was used

$$F(\theta) = \sum_{j=1}^{N_p} [\mathbf{v}_j - \tilde{\mathbf{v}}_j(\theta)]^2 \quad (1)$$

representing the squared error between the induced voltage  $\mathbf{v}_j, j = 1, \dots, N_p$ , measured in the  $N_p$  grid points, and the voltage  $\tilde{\mathbf{v}}_j$  obtained by employing the model at the same points. Best estimate  $\hat{\theta} = \arg \min F(\theta)$ , was calculated where  $\theta = [\mathbf{p}_{tx,1}^T, \dots, \mathbf{p}_{tx,5}^T, I_1, \dots, I_5, S_s]^T$  contains the positions of the transmitting coils, the excitation currents and the surface of the coil sensor that is directly proportional to the sensitivity of the sensor.

The procedure described in Section 4.1 was applied to the optimized model, using the set of  $N_p$  points of the first experiment. For each grid point  $\mathbf{r}_k$ , the induced voltage  $\tilde{\mathbf{v}}_k$  was calculated, along with the three corresponding points along  $x$ -,  $y$ -, and  $z$ - axes for the calculation of the partial derivatives of (3.5), with the same step of 5 mm, as previously described. Finally, the position SD was estimated by means of (3.10). This method requires  $N_p$  measurement points only. It should also be clarified that the voltage SD values used for position SD estimation are the same in both cases were the magnetic field model and the experimental method were used.

### 4.3.1 Results

Figure 4.12 shows estimation of position repeatability error obtained by using magnetic field model.

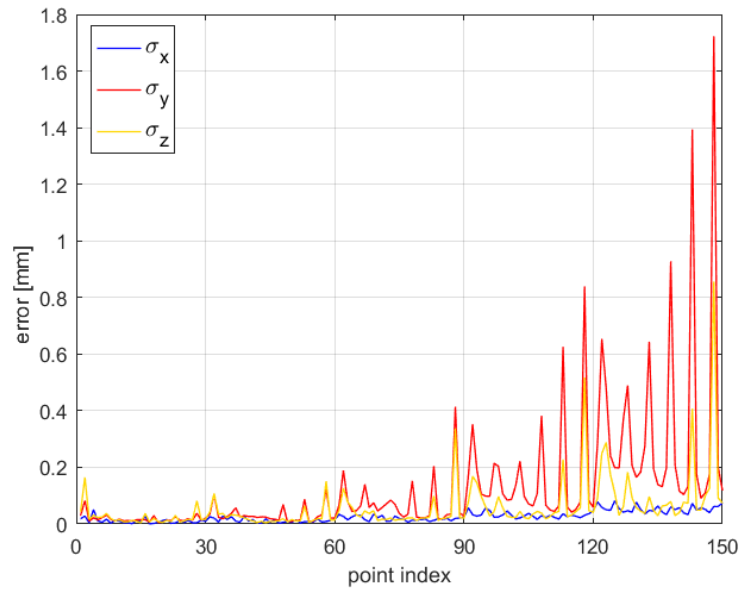


Figure 4.12 Estimation of position repeatability error by magnetic dipole model – 1<sup>st</sup> test, sensor aligned along x-axis. Image source: [49].

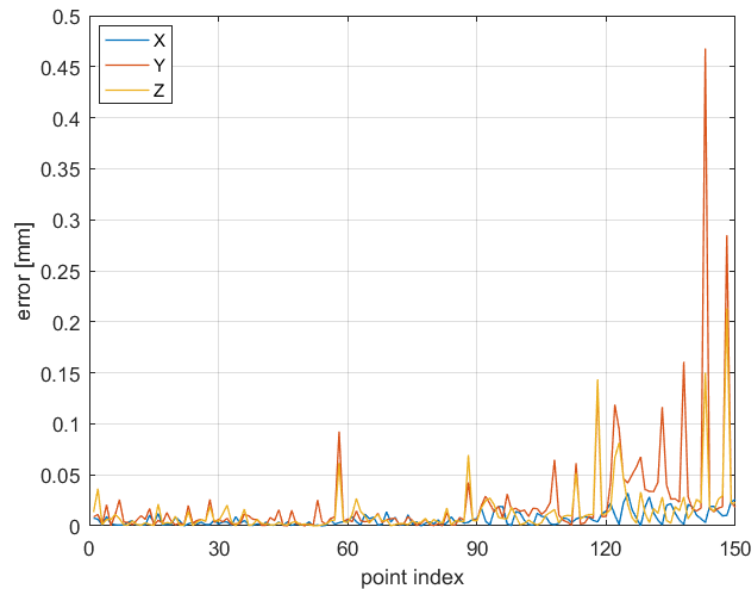


Figure 4.13 Difference between position SD obtained by using magnetic dipole model and experimental data with error propagation error method – 1<sup>st</sup> test, sensor aligned along x-axis. Image source: [49].

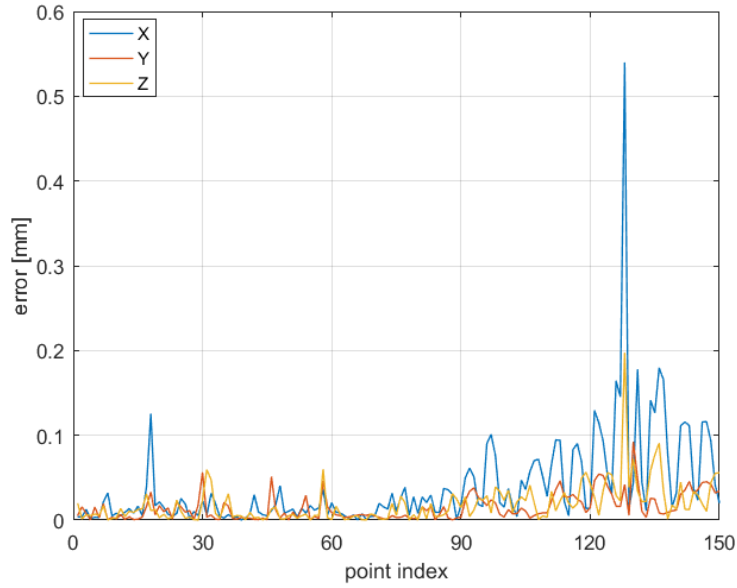


Figure 4.14 Difference between position SD obtained by using magnetic dipole model and experimental data with error propagation error method – 2<sup>nd</sup> test, sensor aligned along y-axis. Image source: [49].

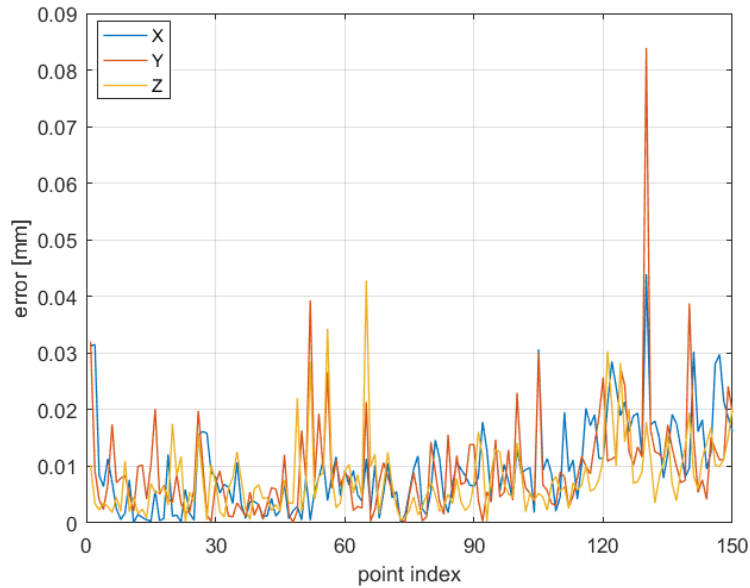


Figure 4.15 Difference between position SD obtained by using magnetic dipole model and experimental data with error propagation error method – 3<sup>rd</sup> test, sensor aligned along z-axis. Image source: [49].

Figure 4.13 shows the difference between the SD values obtained by using the model and the experimental data. It can be observed that, except for two outlier peaks, the error is always below 0.15 mm, with a mean value less than 0.05 mm. These estimation errors

are lower than about one order of magnitude with respect to the accuracy required for surgical applications [13], [46], [52].

Position SD values obtained by varying the orientation of the sensor, according to the experimental tests described in Section 4.1, were estimated still using the model obtained by fitting the data of the first experiment. Figure 4.14 and Figure 4.15 show the difference between SD obtained by using the magnetic dipole model and experimental data used in propagation error method. Same considerations as above can be made.

### 4.4 Chapter Conclusions

We showed the analysis conducted on an EMTS prototype for surgical navigation, in order to assess the position RMS error due to random components, through propagation of the voltage measurement error, in a volume of 400 mm x 500 mm x 400 mm, for different orientations of the magnetic sensor. The obtained results show good overall system performance in the considered tracking volume, particularly when the sensor is oriented along the z-axis of the FG's reference system, meeting the specifications required for surgical applications. Some interesting aspects have been highlighted, showing the presence of regions where the position error is higher, which is due to magnetic field gradients, or equivalently induced voltage gradients, which are responsible for increased or reduced accuracy in the tracking volume. Further studies should be conducted, exploring all the space around the field generator, to find spatial regions where the system performs better and in order to furtherly investigate the correlation between the coils' arrangement and the position error. Chapter 6 will propose a solution to study the effect of system parameters and FG configuration on tracking accuracy.

The same estimation procedure based on propagation of the voltage measurement error was applied again by using data obtained with a model of the magnetic field where the coils are approximated as magnetic dipoles. We optimized the parameters of the model by fitting experimental data and we estimated position repeatability error. The comparison with the results obtained from experimental data show good accuracy of the proposed method, with maximum differences of 0.15 mm between the two methods. Finally, we tested the method with sensor orientations different from the set of data used to fit the model, obtaining the same order of accuracy. This method is very useful for fast performance evaluation of different systems, since the use of a magnetic field model requires four times less data, and it results independent from the particular number and arrangement of the coils of the FG. Moreover, the error propagation-based approach does not require the development of an algorithm for position reconstruction, since it only needs voltage measurements.



# *Chapter 5*

---

## *Accuracy of Position Reconstruction<sup>3</sup>*

Measurement accuracy evaluation is a crucial phase in system performance assessment and many methods were developed for accurate uncertainty estimation [50], [51], [54]. A very complex issue for tracking systems is to develop suitable techniques or mathematical models to convert raw sensor data into position and orientation measurements with appropriate accuracy. In Chapter 4, the performances of the system were assessed in terms of position repeatability by propagating the voltage repeatability, employing a technique that does not require the reconstruction of sensor position.

This Chapter aims to develop a suitable technique to provide sensor pose estimation. The performance of EMTSs in terms of accuracy and repeatability of position and orientation is evaluated, since medical procedures require accuracy of few millimeters. This Chapter is organized as follows. In Section 5.1 we describe two techniques for sensor position and orientation estimation. In Section 5.2 we analyze the results of simulations performed to compare the two techniques, and we propose a new method to reduce pose estimation error, evaluating its performance on experimental data in Section 5.3. Section 5.4 proposes a method to compensate the effect of magnetic field noise due to noise in excitation current. Finally, conclusions are drawn in Section 5.5.

---

<sup>3</sup> This Chapter is based on papers [28] and [29].

## 5.1 Position Reconstruction Algorithm

In this Section an efficient reconstruction algorithm, to obtain accurate estimation of the instrument position, was developed and tested. Usually, a set of equations is derived by employing a model of the magnetic field, mainly based on magnetic dipole [27], [55], or mutual inductance [26], thus obtaining the pose of the sensor by means of the measured induced voltage in the measurement volume. Alternative techniques, which use interpolation algorithm on few calibration points, without employing a magnetic field model, can also be used [33].

We consider a technique similar to the one presented in [27], where a mobile active coil generates an AC magnetic field which induces a voltage in a set of 17 fixed passive coils. However, in our case, we must consider the different configuration of the EMTS, which has a passive sensor instead of an active one, and much less fixed coils, which are powered with different frequencies according to FDM. Two techniques are presented here to reconstruct the position and orientation of the coil sensor, which are at the base of a third proposed technique. In the next Section their performances are analyzed and compared.

The two base reconstruction methods rely on solving an optimization problem. In particular, the minimization of two different cost functions was analyzed.

### 1) Full cost function

$$F_f(\theta_1) = \left\| \mathbf{v} - (\tilde{\mathbf{v}}(\theta_1)^{\circ 2})^{\circ \frac{1}{2}} \right\|_2^2 = \left\| \mathbf{v} - ((\mathbf{H}\hat{\mathbf{n}}_s)^{\circ 2})^{\circ \frac{1}{2}} \right\|_2^2 \quad (5.1)$$

representing the squared error between the measured induced voltage  $\mathbf{v}$  and the voltage  $\tilde{\mathbf{v}}$  obtained by employing the model of Section 2.2.3, where  $\circ$  denotes the Hadamard power operator, used here to obtain the absolute value of the voltage components. It is a nonlinear problem with five variables,  $\theta_1 = [\mathbf{p}_s^T, \alpha_s, \beta_s]^T$ .

### 2) Concentrated cost function

$$F_c(\theta_2) = \|(\mathbf{I} - \mathbf{P}_H)\mathbf{v}\|_2^2 \quad (5.2)$$

where  $\mathbf{P}_H = \mathbf{H}\mathbf{H}^+$ , and  $\mathbf{H}^+$  is the Moore-Penrose pseudoinverse of  $\mathbf{H}$ . (5.2) is obtained by substituting in (5.1) the least-squares solution of the problem (1.11), which is given by

$$\hat{\mathbf{n}}_s = \mathbf{H}^+ \mathbf{v} \quad (5.3)$$

(5.2) is a nonlinear function of  $\theta_2 = \mathbf{p}_s$ , and represents, in comparison to (5.1), an optimization problem with only three variables instead of five.  $\hat{\mathbf{n}}_s$  is then obtained via (5.3) after solving (5.2).

We must note that, when using the second technique, a problem arises due the fact that the measurements  $\mathbf{v}$  are RMS values, all positive, whereas the model (1.11) returns values with sign, according to the orientation of the sensor. In fact, if we replace  $\mathbf{v}$  in (5.3) with its absolute value,  $\hat{\mathbf{n}}_s$  will not be estimated well, and (5.2) will return wrong results. This issue is not discussed in [27]. Hence, in order to overcome this problem, (5.2) is modified as follows

$$F_c(\theta_2) = \|(\mathbf{I} - \mathbf{P}_H)(\mathbf{S} \circ \mathbf{v})\|_2^2 \quad (5.4)$$

where  $\circ$  denotes the Hadamard product operator, and (5.3) is modified as follows

$$\hat{\mathbf{n}}_s = \mathbf{H}^+(\mathbf{S} \circ \mathbf{v}) \quad (5.5)$$

where  $\mathbf{S}$  is a  $R^{n \times 1}$  vector containing the signs  $s_i \in \{-1, 1\}$  of each voltage component.  $\mathbf{S}$  is estimated, for each measurement point, by computing  $F_c$  for all the  $2^{n-1}$  combinations of the signs (the other  $2^{n-1}$  are redundant) and choosing the vector that returns the minimum value. We verified that this step is computationally feasible for  $n = 5$  used in the experimentation.

As will be clear in the next Section, both the full and the concentrated cost functions have advantages and drawbacks, hence we propose a third improved technique in which the result of the estimation by means of the concentrated cost function is used as a starting point for full cost estimation.

## 5.2 Validation of the Reconstruction Algorithms

To solve both (5.1) and (5.4) we use the Levenberg–Marquardt algorithm, which needs to be initialized with a first guess of the parameters. When tracking an instrument in a medical scenario, the trajectory is continuous and, in each instant, the algorithm is initialized with the estimation obtained in the previous instant. However, if an estimation error occurs, it can affect the estimation of the subsequent point. Hence, in this Section we evaluate the robustness of the two already known cost functions with respect to errors

in the parameters by performing several simulations in a large tracking volume, and compare their performance with the third proposed combined technique.

We consider a 3D grid of 500 mm x 500 mm x 800 mm, with a step of 100 mm along  $x$ - and  $y$ -axis, in the range  $[-250, 250]$  mm, and a step of 200 mm along  $z$ -axis, in the range  $[100, 900]$  mm. For each point, we provide the voltage measurements  $\mathbf{v}$  by means of (1.11), for nine different orientations of the sensors: the  $x$ -,  $y$ - and  $z$ -axes, and the bisectors of first and second quadrant, respectively, for the  $xy$ -,  $xz$ - and  $yz$ -planes. For each simulation, we employ the two cost functions by initializing the algorithm with the true value of the parameter with the addition of a perturbation.

In particular, the following cases are considered:

- a) orientation perturbation:  $\mathbf{e}_{\alpha_s} = 3^\circ$ .
- b) position perturbation:  $\mathbf{e}_{p_s} = \left[ \sqrt{\frac{100}{3}}, \sqrt{\frac{100}{3}}, \sqrt{\frac{100}{3}} \right]^T$  mm, which satisfies  $\|\mathbf{e}_{p_s}\| = 10$  mm.
- c) combination of *a)* and *b)*.

Obviously, the orientation perturbation will not affect  $F_C$  because the function is not directly dependent on sensor orientation. Moreover, case *a)* will not introduce estimation errors; for the same reason, case *c)* and case *b)* should produce the same results when  $F_C$  is used.

Before starting the simulation tests, the magnetic field model was fitted by using the experimental data collected in few points of the measurement volume to improve the model accuracy. The parameter values found in this preliminary phase were  $\boldsymbol{\theta} = [\mathbf{p}_{tx,1}^T, \dots, \mathbf{p}_{tx,5}^T, \hat{\mathbf{n}}_{tx,1}^T, \dots, \hat{\mathbf{n}}_{tx,5}^T, I_1, \dots, I_5, S_s]^T$ , which include the positions and the direction vectors of the transmitting coils, the excitation currents and the area of the coil sensor that is directly proportional to the sensitivity of the sensor. In Section 4.3, the set of optimized parameters  $\hat{\boldsymbol{\theta}}$  was obtained by finding the minimum of unconstrained multivariable function, i.e.  $\hat{\boldsymbol{\theta}} = \arg \min F(\boldsymbol{\theta})$ , by using an algorithm based on Nelder-Mead simplex method [53]. Here, in order to avoid local minima corresponding to a wrong parameter  $\boldsymbol{\theta}$ , we defined constraints for  $\boldsymbol{\theta}$  and we solved the optimization problem by using an interior point algorithm [56]. The following cost function was used

$$F(\boldsymbol{\theta}) = \sum_{j=1}^{N_p} \left\| (\tilde{\mathbf{v}}_j(\boldsymbol{\theta}) - \mathbf{v}_j) \circ \tilde{\mathbf{v}}_j(\boldsymbol{\theta})^{\circ-1} \right\|_1 \quad (5.6)$$

representing the squared relative error between the induced voltage  $\mathbf{v}_j$ ,  $j = 1, \dots, N_p$ , measured in the  $N_p$  fitting points, and the voltage  $\tilde{\mathbf{v}}_j$  obtained by applying the model in the same points.

### 5.2.1 Case *a*: Orientation Perturbation

Figure 5.1 and Figure 5.2 show the simulation results for case *a*), when the sensor is oriented along  $x$ -axis (the following conclusions are the same for other orientations) and angle  $\alpha_s$  is perturbed. The position index corresponds to a scanning path in which position is increased along  $x$ -axis at first, then along  $y$ - and finally  $z$ -axis. The errors for  $F_C$  are not shown, because orientation and position errors are negligible. It can be noted that also for  $F_f$  the orientation and position error is negligible, except for some peaks with high amplitude, where the reconstruction of both position and orientation is not accurate. These peaks are due to the convergence to local minima.

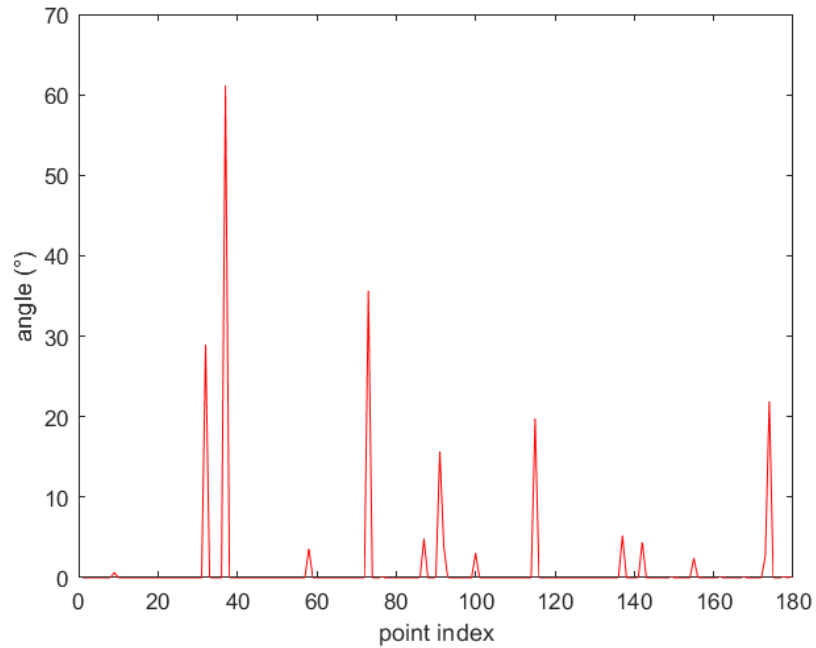


Figure 5.1 Orientation estimation error as function of point index, for a perturbation of  $3^\circ$  from the true value of  $\alpha_s$ , obtained using  $F_f$  with sensor aligned along  $x$ -axis. Image source: [28].

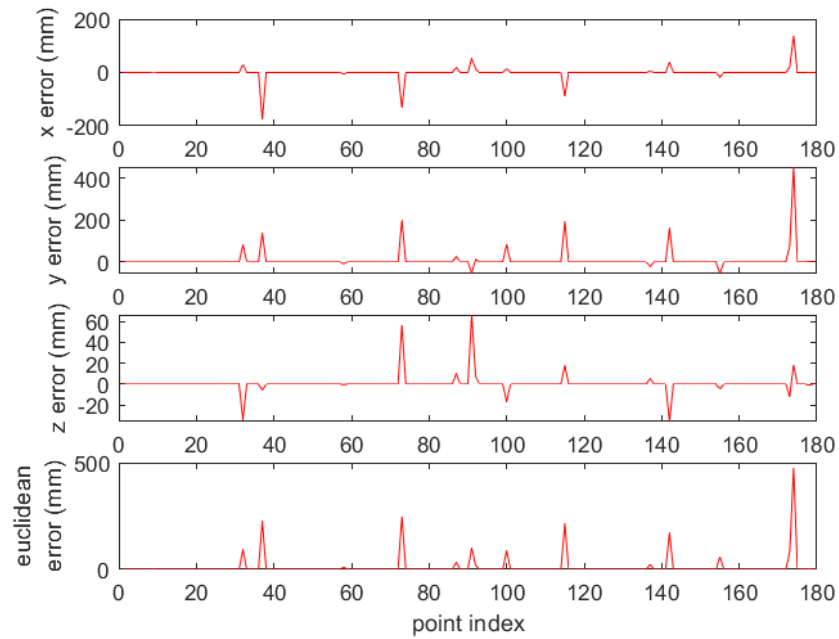


Figure 5.2 Position estimation error as function of point index, for a perturbation of  $3^\circ$  from the true value of  $\alpha_s$ , obtained using  $F_f$  with sensor aligned along  $x$ -axis. Image source: [28].

### 5.2.2 Case b: Position Perturbation

Figure 5.3 and Figure 5.4 show the results for case  $b$ ), when the sensor is oriented along  $x$ -axis. It can be noted that when using  $F_C$  the orientation error is no longer zero as it was for orientation perturbation, with an orientation error higher near the FG, which decreases below  $0.5^\circ$  as we go beyond 0.3 m from the FG (after position index 36). The position error for  $F_C$  is not zero as well, but it is below 4 mm almost everywhere. We can note a periodicity in both orientation and position error, which we have attributed to sensor movement along  $x$ -coordinate; moreover, this periodicity seems not to be affected by the distance from the FG. Finally, we should note that  $F_f$  presents fewer estimation error peaks with respect to case  $a$ ), with lower amplitude, for both orientation and position estimation.

This represents an interesting result, because it shows that we should prefer  $F_f$  minimization due to the absence of error in most of the points, but the presence of high estimation errors in a few points is problematic considering that they may be the starting points for subsequent estimation along the trajectory, leading the position and orientation reconstruction to diverge significantly.

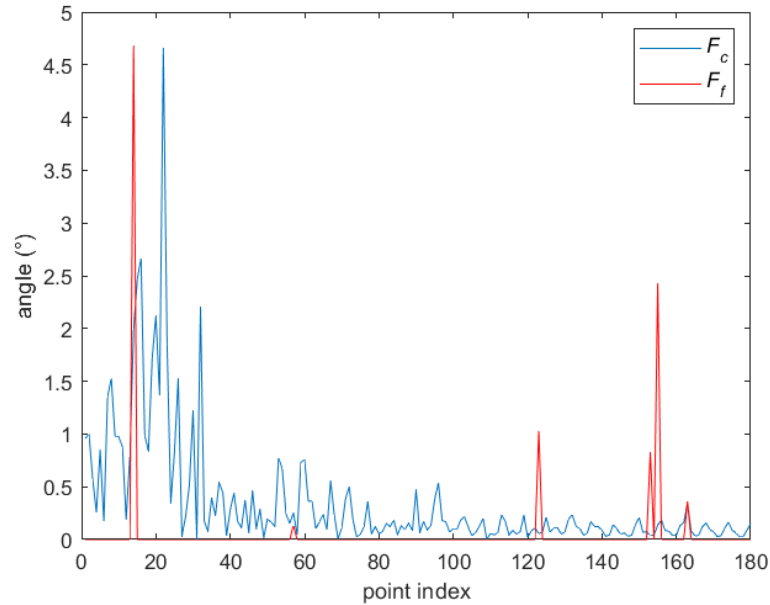


Figure 5.3 Orientation estimation error as function of point index, for a perturbation of 10 mm from the true value of  $\mathbf{p}_s$  with sensor aligned along  $x$ -axis; comparison between  $F_c$  and  $F_f$ . Image source:[28].

### 5.2.3 Case c: Orientation and Position Perturbation

From the above considerations, we can say that  $F_f$  is more sensible to orientation perturbations of  $3^\circ$  than to position perturbations of 10 mm, whereas  $F_c$  is sensible only to position perturbations. Hence, it seems reasonable to combine the two methods to improve estimation accuracy. In particular, we can use  $F_c$  to estimate sensor orientation in a more robust way (less prone to large errors), which is then used as the starting point for  $F_f$  minimization (that reduces estimation error if the initial guess is near the minimum): this reduces the occurrence of large orientation estimation errors, especially when an orientation perturbation occurs.

We tested the proposed technique for case c). The results, reported in Figure 5.5 and Figure 5.6, show an improvement when using the  $F_c+F_f$  solution, which presents fewer error peaks and lower error amplitude. The errors for  $F_f$  and  $F_c+F_f$  are negligible, except for the peaks. Note that the errors for  $F_c$  are the same as in Figure 5.3 and Figure 5.4.

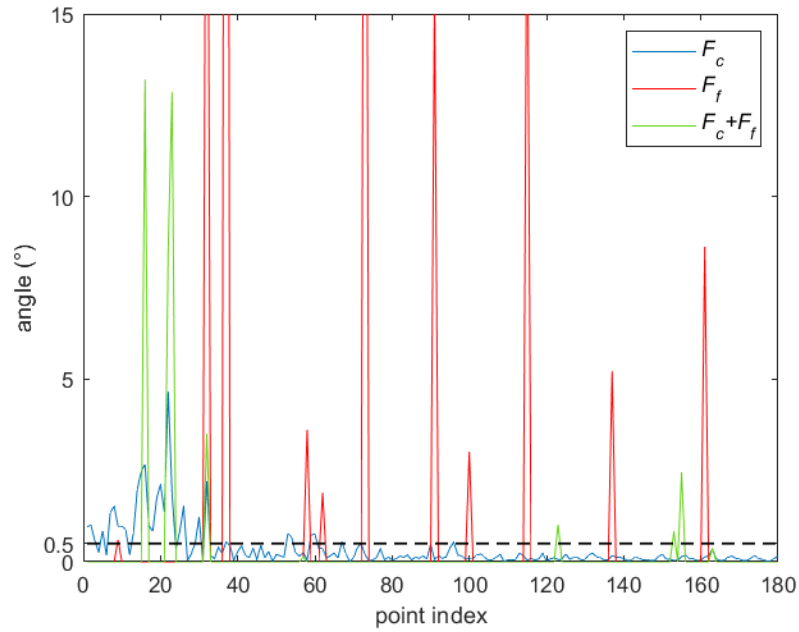


Figure 5.4 Orientation estimation error as function of point index, for a perturbation of  $3^\circ$  from the true value of  $\alpha_s$  and of 10 mm from the true value of  $\mathbf{p}_s$ ; comparison between  $F_c$ ,  $F_f$  and  $F_c + F_f$ . The peaks not shown for  $F_f$  are up to  $60^\circ$ . Image source: [28].

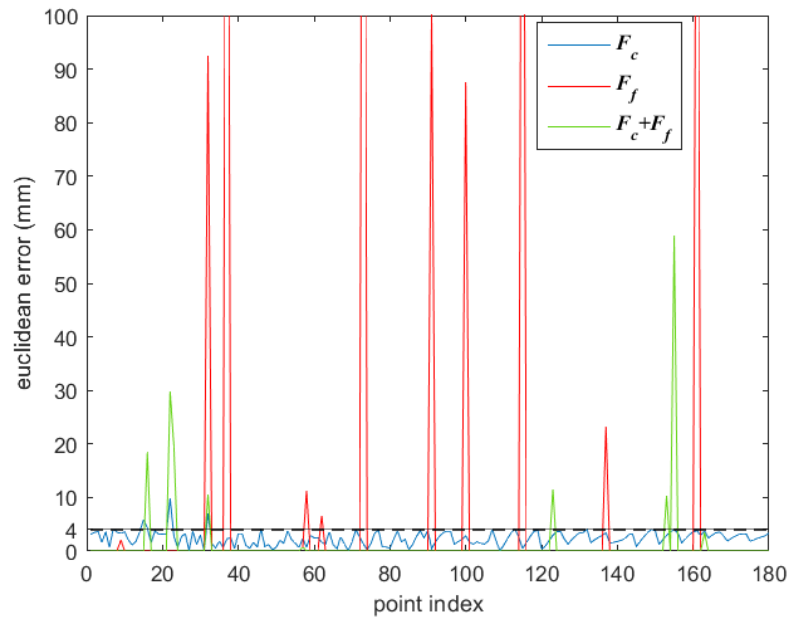


Figure 5.5 Position estimation error as a function of point index, for a perturbation of  $3^\circ$  from the true value of  $\alpha_s$  and of 10 mm from the true value of  $\mathbf{p}_s$ ; comparison between  $F_c$ ,  $F_f$  and  $F_c + F_f$ . The peaks not shown for  $F_f$  are up to 250 mm. Image source: [28].

### 5.3 Experimental Results

We now apply the algorithm  $F_c + F_f$  on experimental data from the EMTS prototype for the reconstruction of a straight-line trajectory along the  $x$ -axis, at a height of 600 mm from the FG. To simulate a real scenario, we add to the initialization position and orientation of the first point, a position and orientation error of 10 mm and  $3^\circ$ , respectively.

In Figure 5.7, Figure 5.8, and Figure 5.9, the results for the experimental data are shown: position errors are quite low, with a mean of about 6.5 mm, and a mean orientation error of about  $2.4^\circ$ . We can note the presence of offset errors both in position and orientation estimation. This result can be improved by performing a calibration of the system before the navigation procedure. The red plots in Figure 5.7, Figure 5.8, and Figure 5.9, show the results obtained by considering the position and orientation errors in the first point of the trajectory (which we assume to be known) and performing a linear transformation for each subsequent point. The calibrated trajectory presents a mean position and orientation error of 2.2 mm and  $0.5^\circ$ , respectively. This procedure can be generalized by placing the sensor in few calibration points in the measurement volume, with known position and orientation [57].

That result should be appreciated in relation to the large distance from the FG. For example, in the areas of percutaneous punctures a mean accuracy of 6 mm or lower seems feasible for good systems [13].

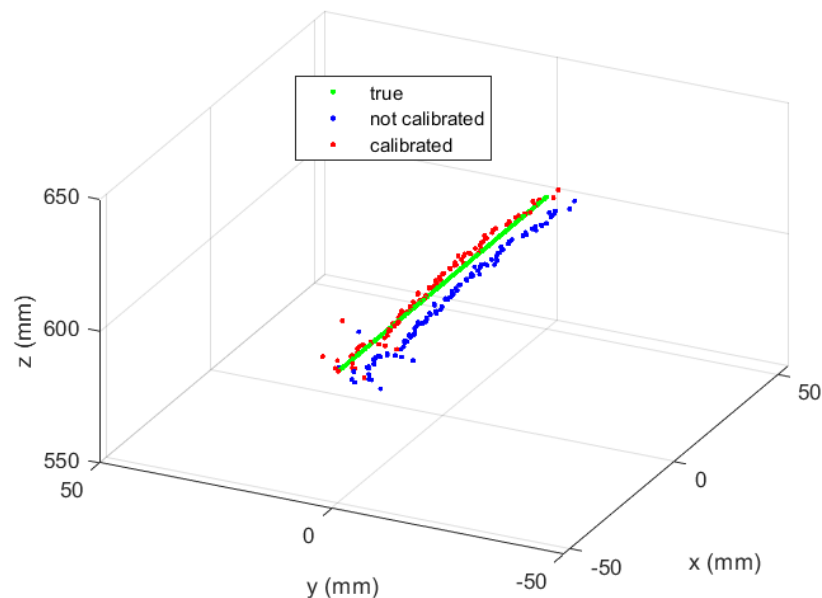


Figure 5.6 Trajectory estimated by using  $F_c + F_f$  on experimental data. Image source: [28].

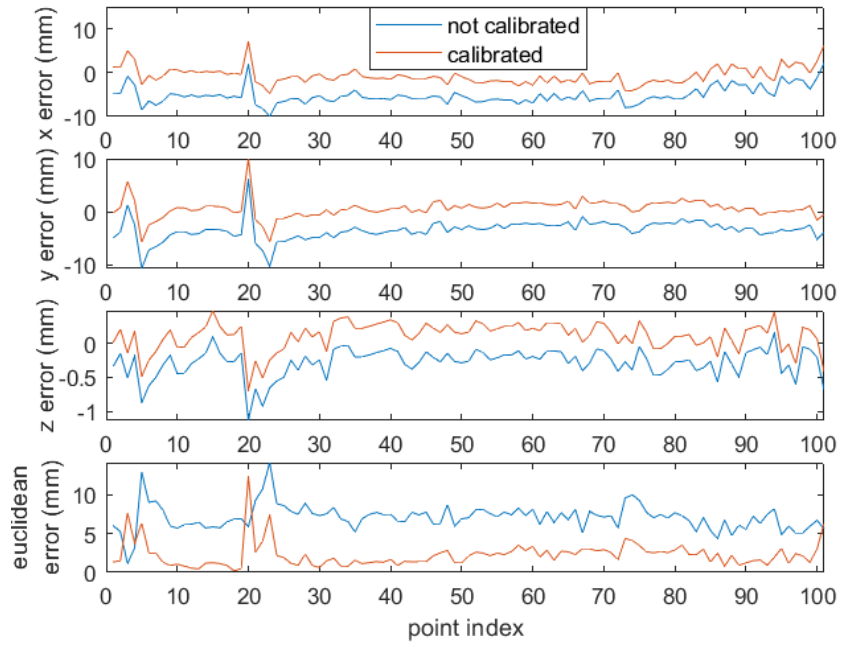


Figure 5.7 Position errors in estimating a trajectory by using  $F_c + F_f$  on experimental data. Image source: [28].

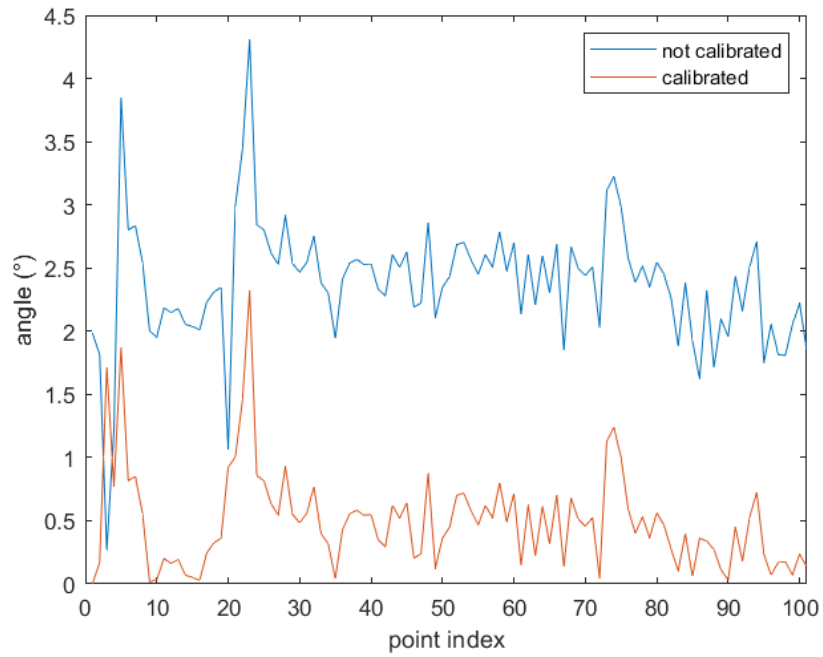


Figure 5.8 Orientation errors in estimating a trajectory by using  $F_c + F_f$  on experimental data. Image source: [28].

Finally, we want to evaluate position repeatability, in order to validate the techniques presented in our previous works [32], [48].

We move again the sensor in the same positions of the trajectory of Figure 5.7, and for each point we perform 20 repeated measurements of the induced voltage. Figure 5.9 shows the std (standard deviation) of the position and orientation error for each point of the trajectory. To summarize the std of all position components, we have calculated the position Euclidean error and its std averaged over all position indices, obtaining 1 mm. The mean orientation repeatability was about  $0.25^\circ$ . These results confirm what we obtained in Section 4.1.1, where position repeatability errors less than 1.6 mm were obtained for different sensor orientations at a distance of 0.5 m, thus assessing the high repeatability of the system. Note that the repeatability error is higher than that obtained in Section 3.4.4 by propagation of voltage measurement noise, and it is comparable with the performance of the Aurora system.

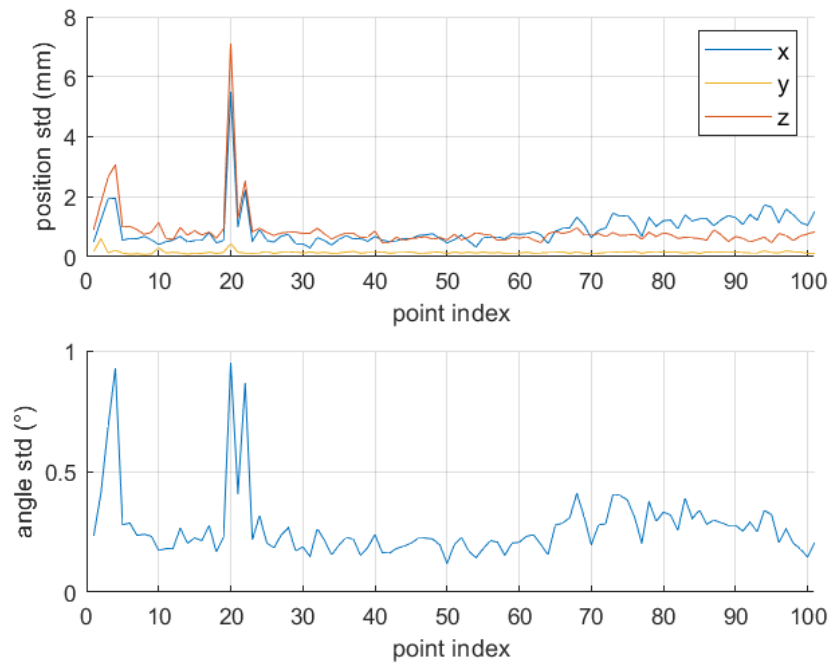


Figure 5.9 Position and orientation repeatability error in estimating a trajectory by using  $F_c + F_f$  on experimental data. Image source: [28].

## 5.4 Compensation of Excitation Currents Noise

In the previous Section, the minimization of the following cost function was analyzed

$$F(\boldsymbol{\theta}) = \|\mathbf{v} - \tilde{\mathbf{v}}(\boldsymbol{\theta})\|_2^2 \quad (5.7)$$

which represents the squared error between the induced voltage  $\mathbf{v}$  measured from coil sensor and the voltage  $\tilde{\mathbf{v}}$  obtained by applying (1.11). However, this cost function depends

only on the five variables  $\boldsymbol{\theta} = [\boldsymbol{p}_s^T, \alpha_s, \beta_s]^T$ , without considering excitation currents: in this way, variations in currents are difficult to detect and to compensate by the algorithm.

In this Section we modify the cost function and the related model by including the currents vector  $\boldsymbol{I}_{tx}$  in the field model, since we measure them in the control loop.

Hence (5.7) is modified as follows:

$$F(\boldsymbol{\theta}, \boldsymbol{I}_{tx}) = \|\boldsymbol{v} - \tilde{\boldsymbol{v}}(\boldsymbol{\theta}, \boldsymbol{I}_{tx})\|_2^2 \quad (5.8)$$

The minimum of (5.8), i.e.  $\hat{\boldsymbol{\theta}} = \arg \min F(\boldsymbol{\theta}, \boldsymbol{I}_{tx})$ , is then obtained by using the Levenberg–Marquardt algorithm.

In this Section we compare the performance of (5.8) with (5.7), applying the algorithm first on simulated data and then on experimental data.

#### 5.4.1 Simulated Data: Currents Noise

In order to validate the correctness of the proposed method, three linear trajectories along  $x$ -axis, at three different distances from the FG, which are 200 mm, 400 mm, 600 mm, with the sensor oriented along  $z$ -axis were considered, and the position error obtained by applying (5.7) and (5.8) are shown in Figure 5.10. Measurement data are obtained by applying the model (1.11) and adding a zero-mean Gaussian noise with  $\sigma_I = 0.07 \text{ mA}$  to excitation currents of each transmitting coil. It can be observed that, in absence of further error sources, such as  $\sigma_{acc}$ , (5.8) is able to reconstruct sensor position with high accuracy, while (5.7) presents not negligible errors. Moreover, when applying (5.7), errors are lower when the sensor is closer to the FG, despite the higher noise  $\sigma_B$  (as seen in Figure 3.18): in fact, it can be easily found that the relative position error  $\frac{\sigma_p}{p}$  is preserved, since it depends on constant magnetic field noise  $\frac{\sigma_B}{V} = \frac{\sigma_I}{I}$ , and therefore the absolute position error increases with distance.

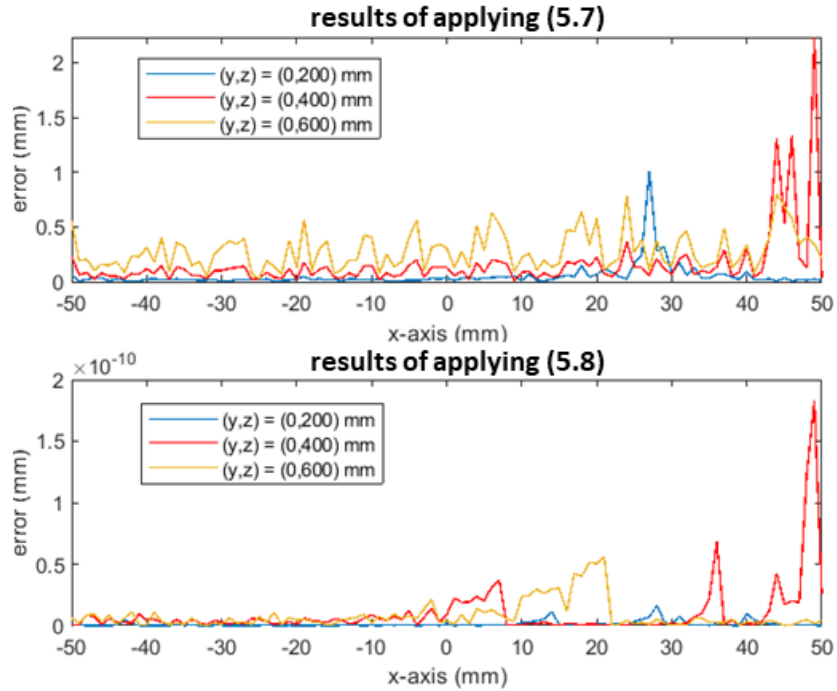


Figure 5.10 Euclidean position error obtained by applying (5.7) and (5.8) to simulated data. A zero-mean Gaussian Noise with  $\sigma_1 = 0.07$  mA was added to excitation currents of each transmitting coil. The sensor is aligned along z-axis.

### 5.4.2 Simulated Data: both Currents and Measurement Noise

We now repeat the simulation in Section 5.4.1, by adding also a zero-mean Gaussian Noise with  $\sigma_{acq} = 20$  nV to the induced voltage, simulating the acquisition process. The results, shown in Figure 5.11, highlight the better performance of (5.8), in particular near the FG, at less than 400 mm, where  $\sigma_B$  is predominant, confirming the considerations already made. This is a valuable result, also considering the state-of-the-art of commercial EMTSs, whose tracking distance does not exceed 500 mm.

Finally, we must note that the measurement noise  $\sigma_{acq}$  is predominant at 600 mm, as already shown in Figure 3.18, limiting the accuracy achievable from the system. Hence it is crucial to reduce it, as shown in Section 3.2.

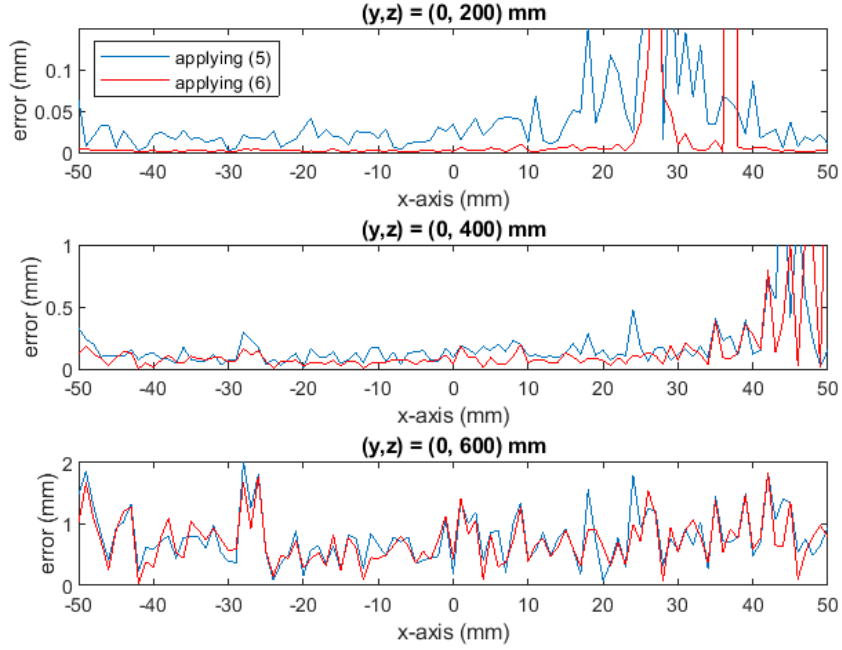


Figure 5.11 Euclidean position error obtained by applying (5.7) and (5.8) to simulated data. A zero-mean Gaussian Noise with  $\sigma_I = 0.07 \text{ mA}$  was added to excitation currents of each transmitting coil, and a zero-mean Gaussian Noise with  $\sigma_{acq} = 20 \text{ nV}$  to the induced voltage. The sensor is aligned along  $z$ -axis. Peaks are cut off for better visualization. Image source: [29].

By comparing the result of Figure 5.10 and Figure 5.11 for the application of (5.8), it is shown that in the latter case the error is not negligible. That results can be explained with the simple additive model of measurement and acquisition error. In fact, the voltage induced from the  $i$ -th coil, obtained by employing (1.11), is

$$\hat{v}_i = \tilde{v}_i(\boldsymbol{\theta}, I_{ii}(t)) + e_{acq_i}(t) \quad (5.9)$$

Then, for a given value of  $\boldsymbol{\theta}$ , the minimized cost function is

$$F(\boldsymbol{\theta}, \hat{\mathbf{I}}_{tx}) = \sum_{i=1}^5 [\hat{v}_i - \tilde{v}_i(\boldsymbol{\theta}, \hat{I}_{ii})]^2 = \sum_{i=1}^5 [e_{acq_i}(t)]^2 \quad (5.10)$$

Hence, when  $e_{acq_i}(t)$  is not zero, there is a difference between true and estimated parameters value.

### 5.4.3 Experimental Data

We now apply (5.7) and (5.8) to experimental data, obtained moving the sensor along the linear trajectory of the previous simulations, at  $z = 600 \text{ mm}$ . In order to reduce errors due to uncertainty in the model parameters, we performed a fitting of the model on few experimental points.

The results of (5.7) and (5.8) are shown in Figure 5.12. It is evident the reduction of the position error peaks at indexes 3 and 20, related to high values of  $\sigma_i$  (Figure 3.9), of about 70%. This good result is due to the inclusion of the value of excitation currents in cost function (5.8), allowing to reduce errors due to excitation currents variations. Overall, a mean position error of 3 mm is achieved. Obviously, other sources of error and the approximation of coils to magnetic dipoles increase experimental position error with respect to simulations. Finally, position accuracy can be further improved by applying some calibration procedures to reduce systematic errors, as shown in [28], [57]; further studies will regard the development of a suitable calibration protocol and the implementation of techniques to reduce the effect of other sources of error, such as the measurement and acquisition noise.

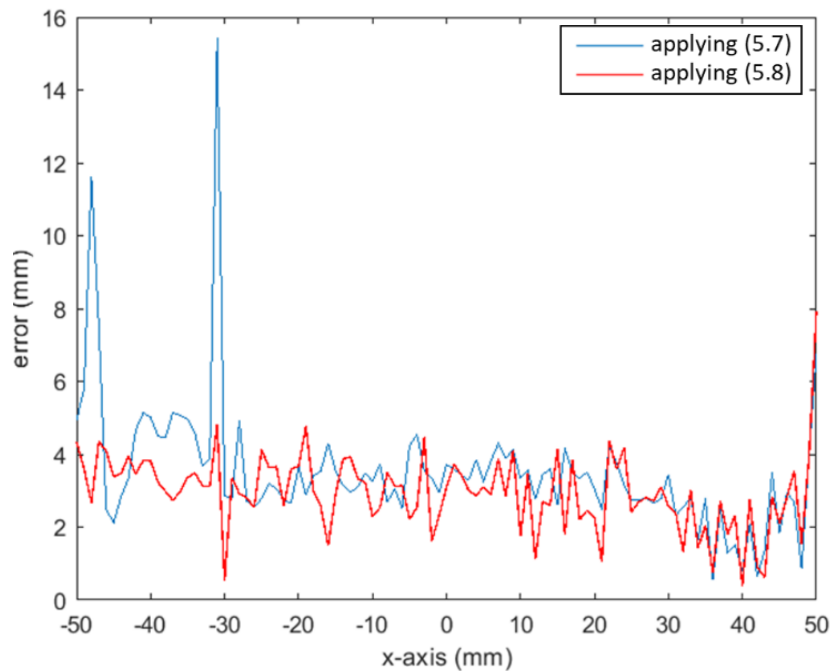


Figure 5.12 Euclidean position error obtained by applying (5.7) and (5.8) to real data, at 600 mm from the FG. The sensor is aligned along z-axis.

## 5.5 Chapter Conclusions

In this Section we illustrated a position reconstruction algorithm which relies on the magnetic dipole model approximation, and the results of position and angle estimation obtained by using two different cost functions were analyzed. In particular, one function encompasses all the position and angle parameters of the sensor, and the other one is a concentrated version in which the angle estimation sub-problem is solved with the linear least square method. To apply the two methods to the developed EMTS prototype, the specific parameters of system configuration were taken into account. The performance of the two techniques was analyzed and compared in a large measurement volume. The results obtained with the two estimation methods in terms of robustness and pose errors, allowed us to propose a new technique in which the best characteristic of both were easily combined. The analysis was performed by using simulated as well as experimental data. The results shows that a mean position error of 2.2 mm, and a mean orientation error of  $0.5^\circ$  is reached in a large volume with a distance from the FG center higher than 600 mm. In the same condition mean repeatability errors of 1 mm and  $0.25^\circ$ , respectively are obtained, which constitutes a noteworthy achievement, and satisfies the accuracy requirements of many surgical procedures [13].

Additionally, we analyzed the effect of variations in transmitting coils' excitation currents, which cause magnetic field variations, resulting in noise in the induced voltage measured by the coil sensor. We quantified this effect by performing several simulations on the EMTS prototype. We then proposed a solution to reduce this unwanted effect, by introducing the measurement of excitation currents in the developed position reconstruction algorithm. We performed different tests both on simulated and experimental data, proving the effectiveness and robustness of the proposed solution.

Further analysis can be conducted on the system, at different position and orientations in the tracking volume. Moreover, the magnetic field model is a valuable tool to investigate several aspects of the system, analyzing how changes of system parameters affect overall performance.

# *Chapter 6*

---

## *A Virtual Platform for Real-Time Performance Analysis of EMTSs<sup>4</sup>*

Tracking distance and accuracy are crucial, and they should be taken into account during the development of a surgical navigation systems. Many aspects affect system performance, and engineers and manufacturers should consider all of them, since also a small accuracy or distance increase is a valuable achievement in this field.

In this Chapter we propose a virtual platform for assessing the performance of EMTSs for surgical navigation, showing in real time how the various sources of error affect the accuracy of tracking distance estimation. This platform provides a useful tool for supporting engineers during design and prototyping of EMTSs.

This Chapter is structured as follows: the main sources of error in EMTSs, and the importance of knowing them during system developing, are discussed in Section 6.1; the virtual platform, developed to provide a tool to analyze system performance during the prototyping phase, is illustrated in Section 6.3; in Section 6.4 the developed virtual platform is evaluated by simulated and experimental tests performed on the EMTS prototype; conclusions are drawn in Section 6.5.

---

<sup>4</sup> This chapter is based on paper [40].

## 6.1 Sources of Error

EMTSs reconstruct the position and orientation of the sensor based on the magnetic field measured by the sensor. Therefore, it is important that the magnetic field does not undergo alterations with respect to the conditions in which it was calibrated by the manufacturer and remains stable over time. Modelling the magnetic field and the various sources of error is crucial in many applications, allowing to implement ad-hoc algorithms for automated error compensation [58], [59]. EMTSs tracking accuracy can be affected by several sources of error, which can be divided into static errors and dynamic errors [13], [46], [60].

**Static errors** occur when the sensor is placed in a given position, maintaining a fixed orientation. They are in turn classified as follows.

- Systematic errors: they are due to distortions of the magnetic field generated by *i)* the presence of metal objects in the surrounding environment, which can produce eddy currents induced by the variable field (mainly in AC systems), which generate secondary magnetic fields that add up to the main magnetic field; *ii)* ferromagnetic materials which, immersed in the main field, orient their domains causing a magnetization that modifies the field lines; and *iii)* power supply currents of the EMTS itself or of other electronic medical devices present in the operating room that can also cause a distortion of the magnetic field. These errors can be reduced by appropriate calibration techniques [57].
- Random errors (also referred to as jitter [13], [61]): these errors, mainly due to noise, reduce the repeatability of the system.

**Dynamic errors** change over time, and they are mainly caused by variations in external EM fields, due to the movement of external organs, such as conductive, ferromagnetic, and electrical materials, which cause field distortions that are extremely difficult to compensate. The movement of the sensor itself is also a source of dynamic error, depending on its speed.

It must also be considered that tracking accuracy depends on the design of the FG and the choice of the position reconstruction algorithm. Moreover, the non-ideality of the electronic components of the tracking system itself affects the performance of the system. In fact, the generated field is never perfectly stable due to the intrinsic limits of the FG, and the measurement and acquisition process is subject to noise, which cannot be totally eliminated. For the reduction of random and dynamic errors, suitable filtering techniques and synchronization of the sampling frequency are particularly useful [32]. The implementation of the Kalman filter can also significantly reduce random errors [27].

## 6.2 Assessment Protocols

As seen in Section 6.1, there are several sources of error that affect the performance of electromagnetic navigation systems and it is important to quantify their effects. During the development phase of the system, the manufacturer performs an assessment of position and orientation errors by performing a characterization in terms of accuracy and repeatability, in order to ensure compliance with certain technical specifications; this is done through ad hoc techniques chosen by the manufacturer. However, it is necessary to standardize protocols that define a measurement setup, a generally valid data collection method and an evaluation criterion, in order to evaluate and compare measurement errors of different systems.

Below, the main evaluation protocols in literature are listed, divided according to the type of phantom used [23]:

- Planar phantom: i) it consists of a perforated plate with holes of known size is used, inside which the sensor is placed, thus measuring its position and orientation; ii) another approach is to move a rigid body -on which the sensor is fixed- on a plane, keeping the height of the plane constant, thus evaluating the position error as the deviation from the plane of the phantom. These methods are meant to be repeated at different heights.
- Cubic phantom: it is a cube of known size is used, with holes of different depth and inclination. The position and orientation error can thus be evaluated by exploring a 3D operating volume.
- Mobile Phantom: it allows to evaluate the dynamic distortions generated during the movement of the sensor, through the use of pendulums or rotating plates.
- Robots: this protocol involves the use of robots to move the sensors, providing reference positions and orientations and acquiring data automatically. This approach allows to achieve greater accuracy, but it generates interference with the surrounding environment, and it is much more complex and expensive than other phantoms.
- Other phantoms.

Among the categories presented we can mention two protocols that are considered as standard:

- i.* The Hummel protocol [62], which uses a planar phantom with a perforated plate.
- ii.* Wilson's protocol [63], which uses a cubic phantom.

Other works have also attempted to produce standard evaluation protocols. For example, [64] proposes a simple and repeatable protocol for determining static and dynamic errors. An evaluation of static errors is carried out using a cubic plexiglass phantom, proposing future developments in the evaluation of dynamic errors.

In the next Section a virtual platform is presented, to provide a tool for the characterization and assessment of EMTSSs. It is designed to be used in combination with the robotic arm used in previous Sections, but can also be used in simulation mode without the need of the physical system, so that all parameters can be studied quickly and with much less hardware requirements.

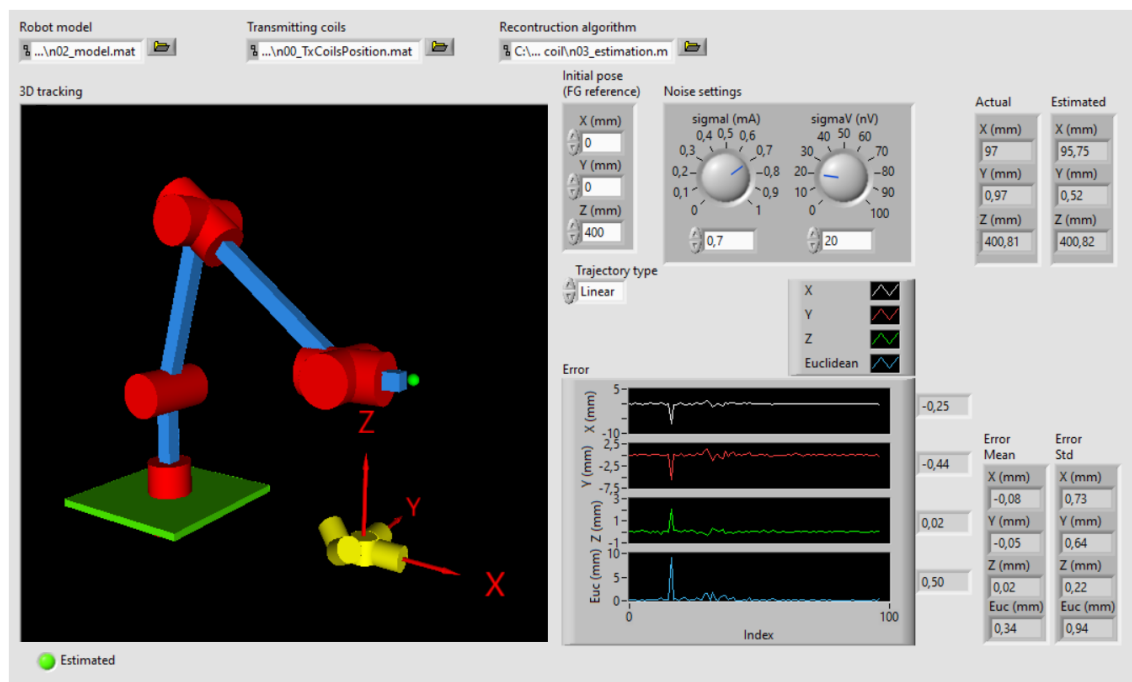


Figure 6.1 Virtual platform developed in LabVIEW, during the execution of a simulation. On the left: the model of the MELFA robot is shown during the movement; the green point is the position estimate provided by the algorithm, and FG reference system is shown in red. On the top: the noise settings section and the trajectory definition are shown. At the bottom: real-time statistics of position error are provided. Image source: [40].

### 6.3 Virtual Platform

The virtual platform is developed in LabVIEW<sup>®</sup> software (by National Instruments Corp.), which is largely used to control and monitor industrial equipment and processes, and for the creation of test and measurement systems [37], [39]. It offers a real-time feedback of tracking accuracy (Figure 6.1) and it provides an intuitive and user-friendly interface.

It is designed to be used in combination with a robot to move the sensor and provide accurate position references. The platform is composed of five main sections, which are described in the following subsections. The functioning of the platform is illustrated in Figure 6.2. The model of the EMTS is defined in an external file and imported into the platform, and the user defines the trajectory for sensor movement. Two different modalities can be performed: *i)* in the experimental mode, the platform connects to the DAQ device and the induced signal in the magnetic sensor is acquired as it is moved by the robot along the defined trajectory, *ii)* in the simulation mode, the signal of the magnetic sensor is simulated by employing a model of the magnetic field; in both cases, noise can be added to the signal. Finally, the position of the sensor is estimated by means of a suitable reconstruction algorithm, providing real-time 3D representation and error statistics.

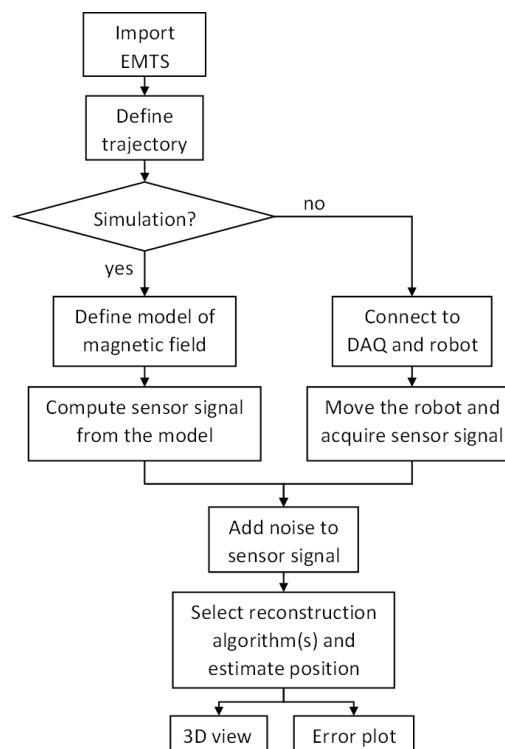


Figure 6.2. Scheme of the functioning of the virtual platform. Image source: [40].

### 6.3.1 3D View and Real-Time Tracking Statistic

Tracking systems provide the surgeon with the real-time estimate of sensor position, which is shown on a screen in front of the surgeon, where is also displayed the patient's anatomic area. 2D and 3D views are commonly used; in particular, the latter is more

difficult to interpret, but seems to guarantee greater precision [65]. Hence, the platform provides a 3D view of tracking, where the actual and estimated position are displayed.

Moreover, real-time feedback of system performance becomes particularly useful when analyzing how a system responds to different inputs. Many design errors can be quickly avoided by real-time feedback. Hence, real-time plot and statistics of position tracking errors are provided during experiments. In particular, the position error along each cartesian axis, computed as the difference between the estimated position and the one provided by the robot, is shown on a graph, and its mean value and standard deviation are displayed. For example, the peak error in Figure 6.1 suggests performing a deeper exploration of the correspondent space region. All tracking results and statistics can be easily exported for further elaboration in Matlab or other software.

### 6.3.2 EMTS Model Import

- The number and arrangement of the transmitting coils, as well as their electrical properties, highly affect system performance [66]. Often the transmitting coils must be placed inside a well-defined space due to practical needs, such as the configuration of the clinical environment, weight limitations, or application requirements. Moreover, the tracking volume is usually proportional to the dimension of the FG (i.e., the magnetic field intensity) [13]. Hence the platform provides the import of a MAT-file (binary MATLAB<sup>®</sup> file) containing the geometrical arrangement and the electrical properties of the transmitting coils of the FG, in order to test different FG layouts, as well as the parameters of the coil sensor. In Section 6.4.2, two different FG configurations will be compared to illustrate this functionality.
- The assessment of tracking accuracy is a mandatory step in EMTSs developing, and different types of protocols have been defined [13], most commonly employing phantoms such as board and cube phantoms, as well as moving phantoms to assess dynamic performance. In addition, robots are also used to move the sensor, providing accurate position references, and allowing automatic and repeatable test; on the other side, robotic components can cause interference in the tracking volume, and they are quite expensive. In [28], the authors used a carbon fiber rod, held by the robot gripper, with the magnetic sensor positioned at the tip, in order to distance the sensor from the metallic components of the robot. The cinematics of the simulated robot (shown in Figure 6.1) is based on a real robot, model RV-2FB-D from Mitsubishi, which was employed in this research to move the sensor; however the platform provides the import of a file containing the model (i.e., the geometry of joints and links) of any robot.

Both the FG and the robot are displayed in the 3D scene of the platform, by means of the LabVIEW Robotics Toolkit. The FG shown in Figure 6.1 represents the EMTS described in Section 6.4.3.

### 6.3.3 Reconstruction Algorithm and Magnetic Field Model

Different techniques can be used to reconstruct the position of the sensor in an EMTS based on Frequency Division Multiplexing.

In [33], a suitable **interpolation algorithm** has been used to reconstruct the position of the sensor in a small space. The sensor is placed in  $M$  different calibration positions, and the voltage from the sensors are measured; then, position estimation is based on interpolation between calibration points by using Delaunay triangulation and linear interpolation. This technique requires measurements of the magnetic field in a dense grid to reach adequate accuracy, it does not allow extrapolation, and it is time-consuming, thus it could be applied only to small regions in the tracking volume.

Other algorithms are based on *i)* a model of the magnetic field obtained by approximating the coils as **magnetic dipoles**, or on *ii)* a model obtained by considering the **mutual inductance** between the transmitting coil and the coil sensor, which are considered as circular filaments [55]. Both models require the knowledge of the geometrical parameters of the coils, and the electrical quantities (i.e., current and voltage) of the transmitting coils, but do not need as many measurements as the interpolation method. Moreover, they could be used to compute the magnetic field (and therefore the induced voltage) in the whole tracking volume, allowing to perform experiments in a simulated environment.

Hence, the platform provides the possibility to choose an arbitrary reconstruction algorithm (developed in Matlab), or to track the sensor simultaneously with two or more reconstruction techniques, to compare their performance in different scenarios.

In this Section, to model the magnetic field produced by the FG and to reconstruct sensor position, we employ the **dipole model** described in Section 2.2.3.

### 6.3.4 Experimental or Simulation Mode

The platform allows to control and perform both simulation and experimental tests.

**Simulation mode** - The aforementioned models allow to carry out experiments on a simulated environment, resulting in a valuable tool for EMTSs design. It is possible to

define the FG and the coil sensor (Section 6.3.2), the position reconstruction algorithm (Section 6.3.3), and custom trajectories along which to move the sensor.

**Experimental mode** – It is possible to define a trajectory, move the robot and acquire data from the Data Acquisition (DAQ) device. The 3D scene will show the real-time movement of the robot, along with the tracked position (the green dot in Figure 6.1).

**Hybrid mode** – It is possible to import experimental data acquired during past experiments, and to run a simulation test showing the tracking results, also simulating the actual acquisition time of the related experiment.

### 6.3.5 Noise Section

The voltage noise in the sensor signal highly affects tracking accuracy. Several error sources contribute to sensor voltage noise, and two main contributions can be considered (all noise components are intended as standard deviation of RMS quantities): *i)* the measurement and acquisition noise  $\sigma_{acq}$ , and *ii)* the FG noise  $\sigma_B(\mathbf{p}_s, \sigma_I)$ . The last one depends on the position  $\mathbf{p}_s$  of the sensor relative to the FG and is due to excitation current noise  $\sigma_I$ . The voltage noise  $\sigma_v$  can be expressed as:

$$\sigma_v = \sqrt{\sigma_B^2 + \sigma_{acq}^2} \quad (6.1)$$

where it has been assumed that  $\sigma_B$  and  $\sigma_{acq}$  both contribute independently. Note that

- $\sigma_{acq}$  is approximately constant in the whole working volume, since it depends on the measurement devices and on the Johnson noise of the sensor. Experimentally, it has been measured  $\sigma_{acq} \cong 20$  nV for each frequency component.
- $\sigma_B$  depends on sensor pose and excitation currents, hence it is related to  $\sigma_I$ , and its contribution is higher when the sensor is closer to the FG. Moreover,  $\sigma_I$  can differ between each transmitting coil. Experimentally, it has been measured  $\sigma_I \cong 0.07$  mA as an average value among transmitting coils. In [29], a technique to compensate the effect of  $\sigma_I$  on the position error has been proposed.

The effect of these noise components must be considered during simulations. Hence, the platform includes a section to set the noise components ( $\sigma_{acq}$  is a scalar,  $\sigma_I$  is a  $n \times 1$  vector), to be added in simulations and also during real-time experiments, to investigate how a certain source of error affects tracking accuracy. For instance, a discussion about the selection of the DAQ device depending on the noise is carried out in Section 6.4.1.

## 6.4 Validation

The proposed platform is suitable for the assessment of virtual EMTSs during simulation, as well as the developed EMTS prototypes. In Sections 6.4.1 and 6.4.2 we employ the platform for a practical case, showing its usefulness in assisting engineers during EMTS design and characterization, and in Section 6.4.3 we illustrate some tests performed on the real EMTS.

### 6.4.1 DAQ Device Selection

The platform can support engineers during DAQ device selection by using the noise section described in Section 6.3.5. When setting up the measurement chain to acquire the signal from the coil sensor, it is important to select the DAQ device according to the accuracy requirements of the system. Frequency sampling and noise are two main parameters to be considered [32], which affect system accuracy. In particular, the noise floor indicated in the datasheet of the DAQ device is added to the induced voltage, thus it directly affects position repeatability and accuracy [32]. In this way, the choice of a low-noise DAQ device can be evaluated for the purpose of improving performance.

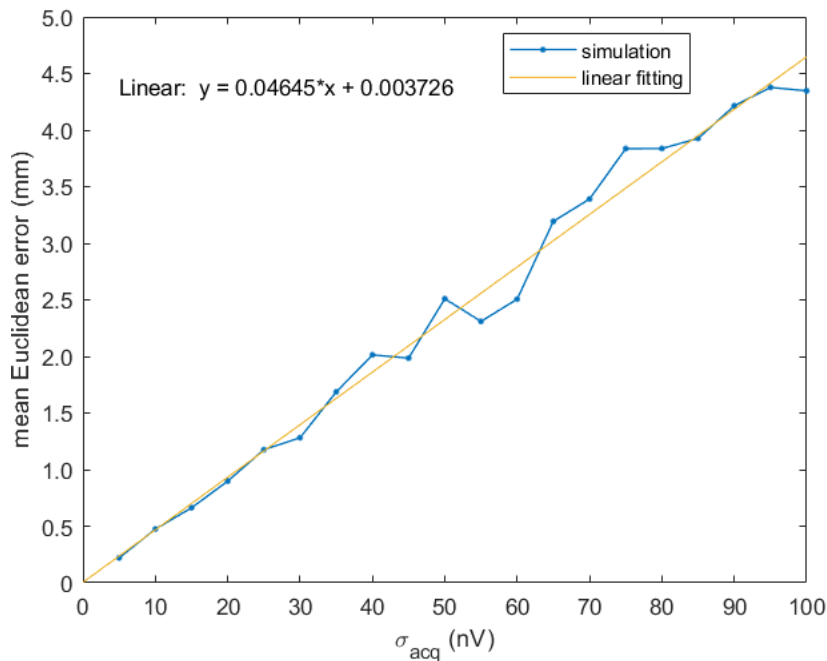


Figure 6.3. Mean Euclidean position error vs.  $\sigma_{acq}$ , assuming  $\sigma_I=0.07$  mA. Image source: [40].

In this Section, we performed some simulations: the RMS induced voltage was simulated by applying (1.11), then adding a voltage noise component to simulate the noise

floor of the DAQ device. Figure 6.3 shows the results, where the mean of the Euclidean position error over a linear trajectory (101 points at 600 mm from the FG) is plotted versus a range of selected  $\sigma_{acq}$ , considering a fixed current noise of  $\sigma_I = 0.07$  mA. As expected, it can be observed an increasing error with  $\sigma_{acq}$ ; moreover, the behaviour is quite linear. A mean Euclidean error below 2 mm is obtained if using a DAQ device with  $\sigma_{acq}$  lower than 40 nV. This information could be particularly useful when choosing components, considering the trade-off between increased cost and required accuracy.

### 6.4.2 FG Configuration Optimization

As said in Section 6.3.2, the platform allows to test different FG configurations, to evaluate the influence of the number, arrangement, and electrical properties of the transmitting coils on system performance. In this Section we compare the performance of two FG configurations: one representing the EMTS prototype (Figure 6.1), and one flat FG composed of six coplanar transmitting coils (Figure 6.4). The coils of the two configurations are identical in their geometrical and electrical parameters, except for their position and orientation in space.

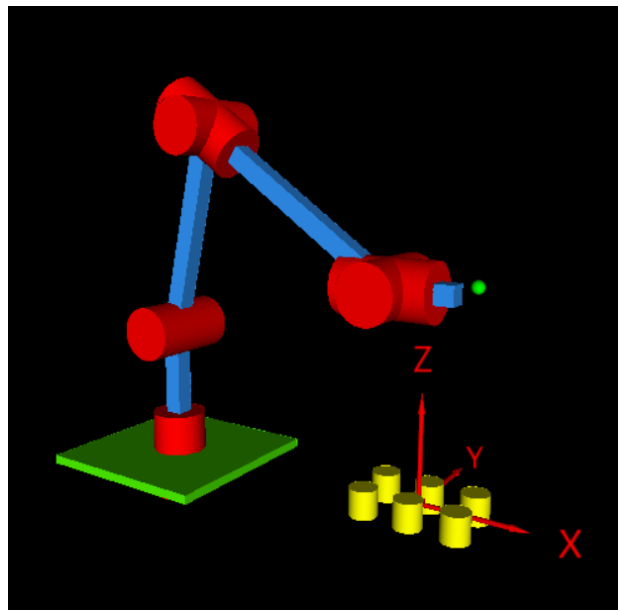


Figure 6.4. Flat FG configuration, obtained by modifying the number of transmitting coils and their position and orientation. The FG reference system is shown in red. Image source: [40].

Figure 6.5 shows the position error along each axes, obtained by keeping the sensor with a fixed orientation along the z-axis, and moving it along the x-axis along a linear trajectory of 101 points, with a step of 1 mm, from point  $(x, y, z)=(-50, 0, 600)$  to  $(x, y, z)=(50, 0, 600)$ , considering the reference system of the FGs. The RMS induced voltage

was simulated by applying (1.11), assuming an acquisition frequency of 20 Hz. Current and voltage noise of  $\sigma_I = 0.07$  mA and  $\sigma_{acq} = 20$  nV were added to each channel.

It can be noted higher accuracy in the 5-coils FG configuration, whereas the 6-coils FG exhibits higher position error, in particular along x- and y-axes. This suggests that further investigation should be performed to understand the cause of the error in that configuration, to avoid it during the realization of the FG.

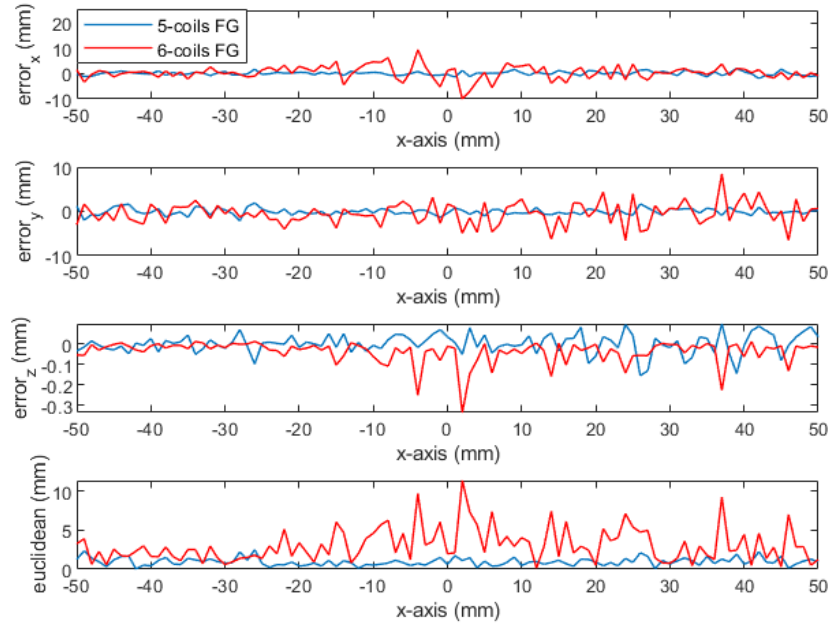


Figure 6.5. Comparison of position error of the two FG configurations. Image source: [40].

### 6.4.3 Comparison with Experimental Test on the EMTS Prototype

The results obtained from the simulations performed with the platform must be comparable with the ones obtained with an actual FG, in order to validate its effectiveness in assisting the system designers.

The EM coil sensor was moved by the robot along the trajectory defined in Section 6.4.2 (which is the same presented in 5.4.3) and the RMS induced voltage was measured with a frequency of 20 Hz, as suitable for real-time surgical. The same trajectory was performed on both simulated and experimental data. For the simulation,  $\sigma_I = 0.07$  mA and  $\sigma_V = 20$  nV were considered for each channel, as quantified from the experimental data.

Figure 6.6 shows the obtained results. The position error obtained in both simulated and experimental case are comparable, with a mean Euclidean position error of about 1

mm and 2 mm, respectively, which is suitable for many surgical procedures [13]. The difference is due to the approximation of the coils with magnetic dipoles, and to uncertainty in parameters. This result validates the performance of the platform in simulating real tracking, providing a valuable tool during system design and prototyping.

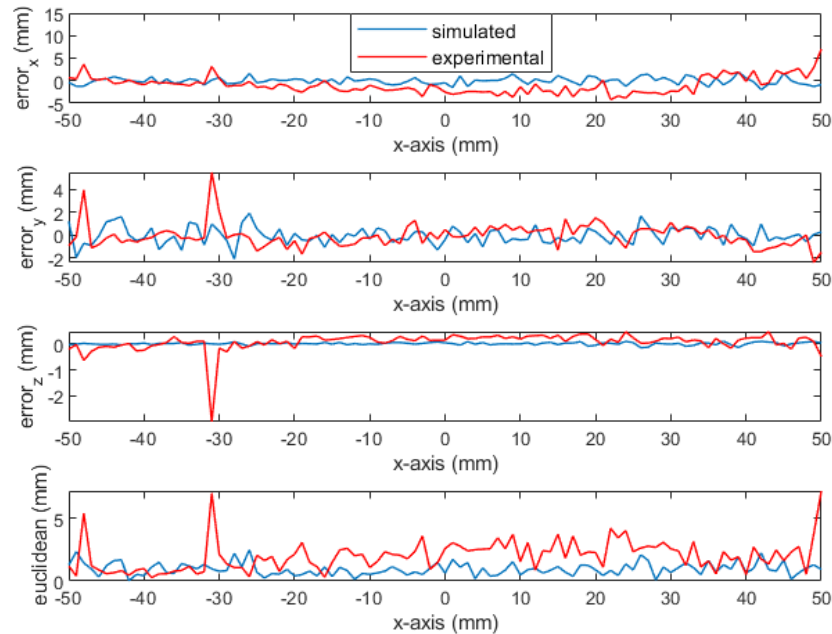


Figure 6.6. Position error from simulated (blue line) and experimental data (red line) obtained by moving the MELFA robot along a linear trajectory at a distance of 600 mm from the FG. The sensor is aligned along z-axis. Image source: [40].

## 6.5 Chapter Conclusions

Several sources of error affect EMTSs, and the high accuracy required from surgical application is highly influenced by the design and arrangement of the transmitting coils of the FG. Many design errors can be quickly identified and avoided by real-time feedback. In this Chapter we illustrated the main features of a virtual platform, which permits to analyze system performance by adding noise components and simulating error sources, hence the robustness and the accuracy of the system and its weaknesses can be studied. Moreover, it can be particularly useful for system prototyping, by investigating the effects of system parameters (geometrical and electrical ones) on tracking accuracy.

The usefulness of the platform was demonstrated by performing simulations related to some practical cases. Finally, it was validated by comparing simulation tests with that performed on the real EMTS prototype, obtaining a mean Euclidean position error of

about 2 mm at a distance of 600 mm from the FG, comparable with the position error of 1 mm obtained by simulations.

Further development will regard an improved graphic and user interface, the inclusion of other sources of error (magnetic field distortion, EM interferences), as well as a dynamic system model, in order to evaluate position error in fast varying conditions; the Kalman filter will also implemented to obtain smooth trajectories. Moreover, in this first version, the algorithm is developed in Matlab, but other programming languages -e.g., Python- will be considered in further versions.



# *Chapter 7*

---

## *Platinum Nanostructured Miniaturized Ion-Sensors<sup>5</sup>*

The role of ion concentration measurements is particularly useful in many fields of applications, ranging from healthcare to plants and animals' health monitoring. One of the main technologies used for ion sensing is based on potentiometric measurements by means of ion-selective electrodes (ISEs), that rely on electrochemical principles to transduce the activity of a target ion into a measurable electrical signal [68]. Traditional ISEs are accurate and provide high stability, but they are quite bulky. Hence, much effort has been put in miniaturizing the electrodes, bringing to the development of all-solid-state ISEs, which are based on a solid contact (SC) that allows ion-to-electron transduction, thus allowing the fabrication of wearable and portable systems with high sensing performances. Flat screen-printed electrodes (SPEs) have been employed to fabricate SC-ISEs, due to their ease of use and availability, but they result bulky when invasiveness becomes a main parameter to be considered. Therefore, growing attention is being paid to needle-type ISEs, which are of particular interest due to their broad range of application, especially in biomedical field. In [69], an all-solid-state microneedle-based potentiometric platform for intradermal monitoring of potassium was presented. The system included a potassium-selective electrode produced by coating a steel microneedle with carbon ink first, and then with carbon nanotubes for the SC. Microelectrodes for in

---

<sup>5</sup> This Chapter is based on paper [67].

vivo sensing were also proposed in [70]. In that case, acupuncture needles were used as the base material and the electrodes were used for monitoring calcium ions in rat cerebrospinal fluid. Needle-type all-solid-state ISEs have also been proposed for live plants monitoring [71], [72], and coastal water monitoring [73], [74].

Among several others, Potassium ( $K^+$ ) ions play a fundamental role for cells functions. Their concentration inside cells is controlled by the  $Na^+/K^+$  pump, which controls the resting potential of the cell membrane, eases the transport of nutrients inside the cell, and regulates the cellular volume [75]. In case of cell damage or altered activity of the  $Na^+/K^+$  pump, the concentration of  $K^+$  ions inside and outside cells changes. In homeostasis, typical intracellular and extracellular  $K^+$  concentration of around 150 mM and 4 mM are measured, respectively. Measuring  $K^+$  concentration can hence be useful for monitoring cells function and detect possible anomalies. In [75], flat SC  $K^+$ -selective electrodes based on electrodeposited Pt nanopetals were fabricated for measuring the efflux of  $K^+$  from cells for the evaluation of acute cell death.

In previous research [76], planar ISEs with SCs based on gold nanostructures (Au-NSs) are compared to platinum nanostructures (Pt-NSs). Pt-NSs offered slightly better performances than Au-NSs in terms of potential stability and reproducibility, thus in this research a study on needle-shaped ISEs which exploit Pt nanostructures (Pt-NSs) as SC is presented, with particular focus on  $K^+$  sensing in the physiological range  $10^{-3} - 10^{-2}$  M  $K^+$ . The reduced sensor size is suitable for biomedical applications when invasiveness has to be minimized, such as surgical navigation procedures, where tracking systems support the surgeon with the localization of the surgical tools [28], [31]. Needle-shaped ISEs can hence be inserted into the surgical instruments, thus providing important information about cellular health in real-time, measuring ion concentration directly from blood inevitably present during surgery, or they can be integrated into ad hoc developed devices like in [31], where a smart pen-shaped electronic system for continuous monitoring of propofol in human serum was proposed.

The literature still lacks studies about the effect of parameters to produce needle-shaped ISEs with Pt nanostructuring. For example, in [77], ISEs were obtained by growing Pt-NSs on a Pt wire with diameter of 0.5 mm, but no investigation of the nanostructuring parameters was performed. In [78], a stainless steel acupuncture needle (diameter of 0.16 mm) was instead covered with Au nanoparticles, and the optimization of Pt nanoflower subsequently grown on the Au substrate was performed by showing different concentrations of the  $HAuCl_4$  solution, and different deposition times. However, the influence of electrodeposition parameters on Pt-NS was investigated in [79] only with regard to flat SPEs, whereas their effect on Pt-NSs grown on a thin Pt wire has been not yet explored so far.

Hence, in this Chapter we analyze the influence of electrodeposition voltage and duration on the morphology of Pt-NS grown on a Pt wire with very small diameter of 0.1 mm in order to find a set of optimized electrodeposition parameters for a regular fabrication of high performances  $K^+$  ISEs. The employed fabrication procedure relies on a one-step template-free electrodeposition process, and it is similar to that reported in [75],[79],[76]. This fabrication procedure has been shown to be very simple and effective. In this study, however, very thin Pt wires are used as conductive substrate of the electrode instead of planar microfabricated Pt SPE [79]: due to this different geometry, many differences in the nano-structuration results with respect to those obtained in [79] are observed and highlighted in this Chapter. The performances of the ISEs in  $K^+$  sensing are then assessed and compared with those obtained in [80], where larger Pt ISEs (circular shape, with radius of 2 mm) were fabricated on a flat flexible substrate with the same electrodeposition procedure and solution concentrations. The proposed electrodes show Nernstian sensitivity, high stability, and a limit of detection (LOD) suitable for  $K^+$  monitoring in biomedical applications.

## 7.1 Background

### 7.1.1 Working Principle

ISEs are based on a working electrode (WE) covered with an ion-selective membrane (ISM) that selectively captures the target ions, proportionally to their concentration in the sample solution under test. ISEs were conventionally built by including in the WE a liquid junction with target ion at constant concentration  $c_A$  (proportional to its activity  $a_A = \gamma_A c_A$ , where  $\gamma_A$  is the single ion activity coefficient) between the electrode substrate and the ISM, which allows ion-to-electron transduction due to redox reactions. Therefore, the concentration of the ions is also proportional to the open circuit potential (OCP) of the ISE relative to a stable reference electrode (RE), which can be simply measured by employing a potentiostat in a two-electrodes configuration (Figure 7.1b). In particular, the activity  $a_x$  of the sample solution is related to  $a_A$  by the Nernst equation:

$$OCP = \frac{RT}{z_A F} \ln \left( \frac{a_x}{a_A} \right) = const + 2.3 \frac{RT}{z_A F} \log(a_x) \quad (7.1)$$

where R is the gas constant, T the temperature,  $z_A$  the valence of the target ion, and F is Faraday's constant. This equation describes a linear relationship between the measured

OCP and  $\log(a_x)$ , with slope of about 59.16 mV/decade at room temperature for monovalent cations, as in the case of  $K^+$ . In this Chapter all results are related to ion concentration  $c_A$ , since the conversion to ion activity can be obtained by considering the activity coefficient known in literature for  $K^+$  [81].

The internal junction increases the stability of the measured potential but, on the other hand, it also implies problems relative to the conservation of the liquid and, mostly, it limits the possibility of miniaturizing the sensors [68]. To overcome these limitations, all-solid-state ISEs have been developed and are currently still very actively studied, with the aim of increasing their miniaturization and performances [82], [83]. In this kind of electrodes, the ISM is connected to the conductive substrate through SC materials of different classes.

One of the most promising types of SC is that based on nanostructured materials [84]–[87]. The OCP of nanostructured SCs is not based on redox reactions as in the case of conventional ISEs or conductive polymers SCs; instead, it is based on the formation of an electrical double layer at the interface between ISM and electrode substrate, due to the accumulation of ion charges at the side of the ISM, which causes the accumulation of holes and electrons on the other side, thus generating an asymmetric capacitor with a potential difference [68].

The function of the SC based on nanostructured materials is to improve the adhesion of the ISM to the electrode due to the larger surface area, and this leads to a reduction of the undesired water absorption by the membrane. Moreover, the SC is characterized by a large electrical capacitance, that reduces the potential drift due to the non-zero current involved in the measurement process, thus enhancing signal stability, and it is insensitive to light conditions. SC-ISEs based on nanostructured material have been used in many fields in recent years, including healthcare [76], [79], [88] and pharmaceutical industry [77], [89].

### 7.1.2 Performance Parameters

Similarly to what has been proposed in [68], four main parameters are considered in this research:

- Sensitivity: it represents the variation of OCP due to a variation of the target ion concentration, and it is expressed in millivolt per decade. It is evaluated by measuring the OCP at known concentration of the target ion. ISEs that exhibit a slope of 59 mV/dec are said to exhibit a Nernstian behavior (eq. 1). Ideal sensitivity can be obtained if the ISM is perfectly selective to the target ion and if it is not subjected to degradation.

- Limit of detection (LOD): minimum target ion concentration that can be detected. In order to increase the ISM detectivity in a specific concentration range, a conditioning procedure by immersing the ISEs in a solution with concentration near to the application range must be performed, since it affects LOD [75].
- Linearity: it is the deviation of the calibration curve from the theoretical curve, and it is expressed in millivolt or in percentage of the concentration range. It is mainly affected by the trapping into the ISM of interfering ions different from the target ion, which occurs when the ISM is not perfectly selective towards the target ion. Simultaneous measurements of the interfering ions (by means of other ISEs with ISM containing the proper ionophores) can be used to compensate this effect and increase linearity [90].
- Stability over time: it represents the variation of OCP in absence of ion concentration variations over a long period of time, and it is expressed in millivolt per hour or millivolt per second. It can be caused by *i)* the formation of a water layer at the ISM/SC interface, *ii)* the polarization effect due to non-zero currents required for the OCP measurements, or *iii)* the degradation of ISM composition, which can lose sensitivity to the target ion. The employment of nanostructured materials as SC has proved to improve potential stability, since it reduces the polarization effect and the formation of water layers.

## 7.2 Materials and Methods

### 7.2.1 Synthesis of Pt Nanostructures

Pt-NSs are grown on Pt wires using a one-step template-free electrodeposition procedure, as described in [79]. A three-electrodes setup is employed (Figure 7.1a), to precisely control the potential of the working electrode (WE), since the current flows through the counter electrode (CE) [91]. Pt wires with diameter of 0.1 mm (by Advent Research Materials Ltd) are used as WE and CE, whereas an Ag wire with diameter of 0.25 mm is used as reference electrode (RE). The potentials are applied using an Autolab PGSTAT12 potentiostat (by Metrohm). During the electrochemical process, the length of Pt wire dipped in the solutions is about 2 cm, whereas the distance between the WE and the CE is about 1 cm.

Bare Pt wires are first cleaned by applying a potential of +2 V for 120 s in 0.1 M H<sub>2</sub>SO<sub>4</sub> (by Sigma-Aldrich), in order to make them free of contaminants, which may interfere with the bonding of the nanostructures. Then Pt is deposited on the WE by

applying negative potentials in a solution containing 25 mM  $\text{H}_2\text{PtCl}_6$  (by Sigma-Aldrich) and 50 mM  $\text{H}_2\text{SO}_4$  [79],[76]. During the process, the solution is stirred at 1200 rpm, using a 5x2 mm magnetic stirring bar, to make the solution homogeneous. This stirring velocity results to be suitable for this electrodeposition process. Finally, cyclic voltammetry is performed to activate the material, acquiring multiple voltammograms between -0.2 V and +1.5 V in 0.1 M  $\text{H}_2\text{SO}_4$  with a scanning speed of 100 mV/s. The procedure is interrupted when two successive voltammograms overlapped, which happened after about ten cycles. As final step, the cleaning process is repeated, by applying a potential of +2 V for 120 s in 0.1 M  $\text{H}_2\text{SO}_4$ .

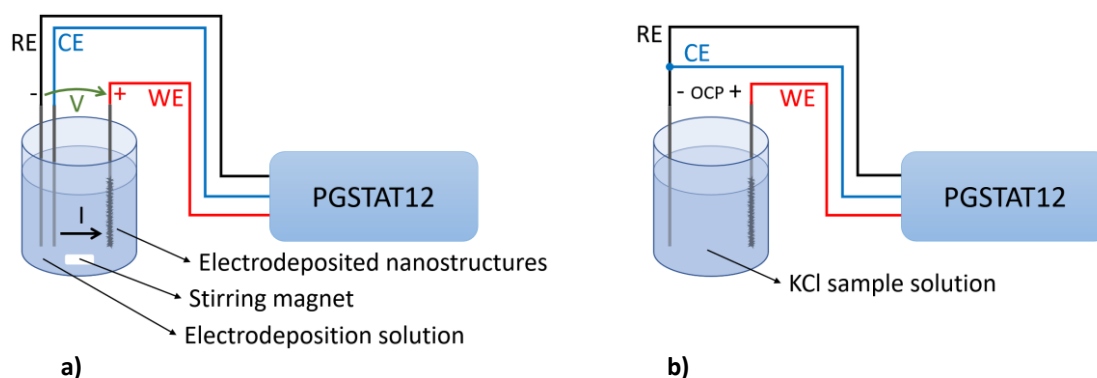


Figure 7.1 a) Setup used for the electrodeposition process, by applying a stable voltage  $V$ . The same setup, except for the stirring, was also used for the cleaning and cyclic voltammetry phases. b) Setup used for the characterization process, by measuring the OCP between WE and RE. Image source: [67].

## 7.2.2 Ion-Selective Membrane

The Pt wires with grown Pt-NSs are then coated with a  $\text{K}^+$ -selective membrane to realize the ion sensors. The membrane is composed of a mixture of: *i*) 33% high molecular weight poly (vinyl chloride) (PVC, by Sigma-Aldrich), which provides mechanical stability and is chemically inert; *ii*) 65% bis (2-ethylhexyl) sebacate (DOS, by Sigma-Aldrich), a plasticizer that increases the free volume of the polymeric materials, thus increasing flexibility, mobility, and durability; *iii*) 0.5% potassium tetrakis (4-chlorophenyl) borate (KTCIB, by Sigma-Aldrich), a lipophilic ion used to make the ISM permeable exclusively to ions of the same sign of the target ion, to ensure Nernstian behavior; *iv*) and 2% potassium ionophore I (by Sigma-Aldrich), a species that binds to the target ions, trapping them in the ISM. This mixture is then dissolved in tetrahydrofuran (THF, by Sigma-Aldrich), following a ratio of 100 mg/1 mL. The Pt-NSs/Pt electrodes are therefore coated by dipping them once in a drop of 5  $\mu\text{L}$  of membrane solution, as shown in Figure 7.2. This procedure is sufficient to completely cover the surface of the dipped region of the wires, which is slightly shorter than the

nanostructured region. It should be mentioned that in other works these needle-shaped electrodes are dipped several times into a beaker containing a bigger quantity of ISM solution [77],[92]. However, not significant variation in the ISM adhesion is found when employing this method, hence we use the aforementioned method to avoid wasting material and working with small quantities so as not to contaminate the ISM solution. Note also that this coating procedure differs from the one employed for SPE, where the ISM solution is directly dropped on the flat electrode surface.

The obtained solid-contact  $K^+$ -selective electrodes are kept drying at room temperature for at least 24 h to allow THF evaporation, and then they are conditioned in 0.01 M KCl (by Sigma-Aldrich) for at least 24 h before starting the characterization measurements, since we are interested in the physiological range  $10^{-3} - 10^{-2}$  M KCl.

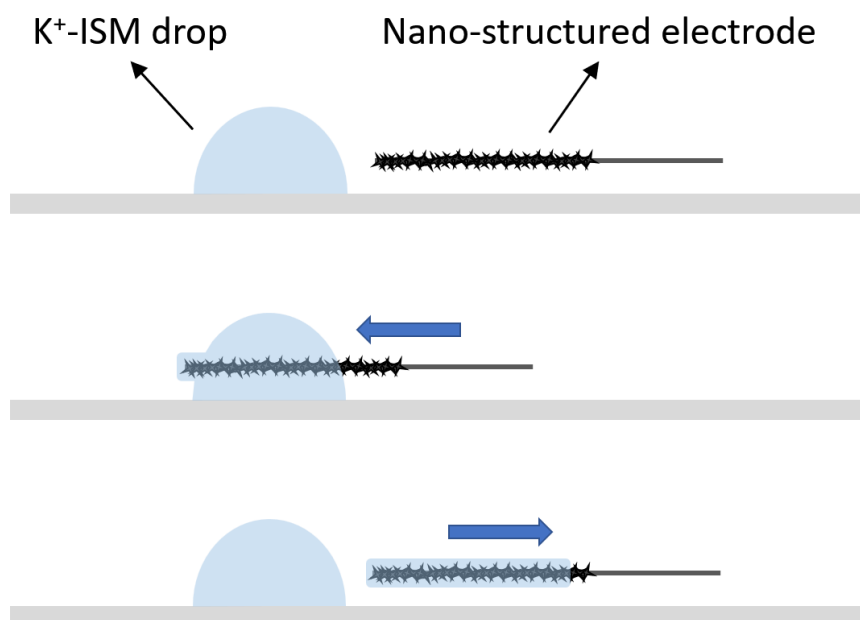


Figure 7.2 Application of the ion-selective membrane to the nano-structured Pt wire. Image source: [67].

### 7.2.3 Morphological Analysis

The morphology of the obtained Pt-NSs is analyzed using scanning electron microscopy (SEM) images acquired with a Zeiss Merlin high-resolution scanning microscope. The InLens detector is used with an accelerating voltage of 1.5 kV, and working distance of about 3 mm. The ISM is observed using an Hirox KH-8700 digital microscope. GIMP [93] and ImageJ software [94] are used for the quantification of

nanopetals and nanospheres sizes from SEM images, whereas the thickness of the ISM is computed directly with the Hirox software.

#### 7.2.4 Electrochemical Measurements

The solid-contact  $K^+$ -selective electrodes are characterized by measuring the OCP when immersed in beakers containing KCl solutions in the range  $10^{-7} - 10^{-1}$  M, which includes the physiological range  $10^{-3} - 10^{-2}$  M. The measurements are carried out in two-electrodes mode by using an Ag|AgCl double-junction electrode as RE (by Metrohm), inner filling solution 3 M KCl, outer filling solution 0.1 M NaCl (by Sigma-Aldrich). The OCP is measured as the difference in potential between the WE and RE. Indeed, we employ a commercial Ag|AgCl RE to ensure the best characterization process but miniaturized RE could be developed in the final step of the research. Note also that Ag/AgCl electrodes are well studied in literature and miniaturized RE have been successfully fabricated in [69], obtaining slopes really close to the Nernstian behavior and very low drift.

In order to evaluate sensors performances, four main parameters are considered in this research: sensitivity, LOD, linearity, and stability over time. The sensitivity is computed as the slope of the line that fits the data points in the linear range, and the LOD is calculated as the intercept between the line fitting the points in the linear region and the line fitting the points in the insensitive region [95] (as shown in Figure 7.7). Linearity is evaluated through the root mean square error (RMSE) between the measured points and the fitting line in the linear region [LOD,  $10^{-1}$ ] M KCl. The time-stability is assessed with a 14-hours measurement of the OCP in the 0.1 M KCl solution, soon after the characterization procedure. Temperature is also measured during the stability assessment, demonstrating that the influence of its variation on the OCP is negligible. Data analysis is carried out using the Matlab software (by MathWorks Inc.).

### 7.3 Results and Discussion

#### 7.3.1 Membrane Adhesion and Nanostructure Thickness

The Pt-NSs layer is evident in Figure 7.3a, with a thickness of about 2  $\mu\text{m}$ , measured by comparing outer diameter before and after electrodeposition procedure. After dipping the electrode in the  $K^+$ -ISM solution, we verified the adhesion of the membrane to the electrode nanostructured surface. Figure 7.3b shows the transparent layer of membrane quite uniformly coated on the Pt electrode surface. The outer diameter is of about 180

$\mu\text{m}$ , almost twice the diameter of the Pt wire, thus indicating the good outcome of the  $\text{K}^+$ -ISM coating.

### 7.3.2 Morphology of the Sensors

Several thin Pt wires are nanostructured at different voltage values, respectively -0.2 V, -0.4 V, -0.6 V, and -1 V, at a deposition time of 200 s, while stirring at 1200 rpm, to investigate the effect of deposition voltage on Pt-NSs morphology. The differently obtained Pt-NSs morphologies are reported in Figure 7.4, and the different density of the fabricated sensors is quite evident. Different applied voltages largely affect the Pt-NSs morphology and density. The Pt-NSs of the sensors fabricated by applying -0.2 V, -0.4 V, and -0.6 V, present the same morphology (i.e., granular), whereas a different morphology (i.e., petal-like) is obtained with -1 V. Furthermore, this latter shows a not fully covered surface, with a density of about 30%. These results are interesting, compared to the ones obtained in [79], where a Pt electrode fully covered with Pt-NS is obtained by applying -1 V after only 200 s. This significant difference shows directly how developing nanostructured working electrodes for electrochemical sensors with planar or wire geometries directly affect the optimized fabrication.

The sensors fabricated with -0.6 V and -1 V are furtherly compared: the former shows the best performances (as shown in Table 7.1), whereas the latter shows a different Pt-NSs morphology and a not fully covered surface. Different deposition times (varying from 50 s to 800 s) are analyzed for deposition voltages -0.6 V and -1 V, with aim of identifying the optimized deposition time as function of deposition voltage.

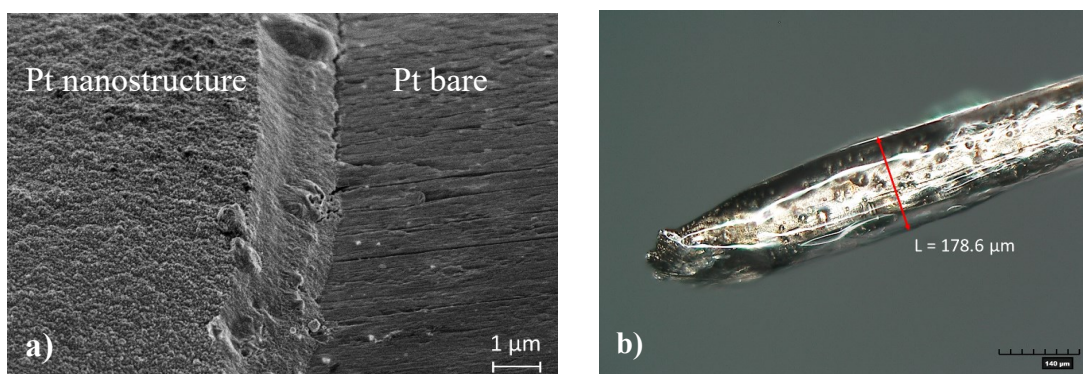


Figure 7.3 a) Thickness of the nanostructure layer obtained with -0.6 V applied for 200 s. b) Digital optical microscope image of the  $\text{K}^+$ -ISM layer on Pt-nanostructured Pt electrode. Image source: [67].

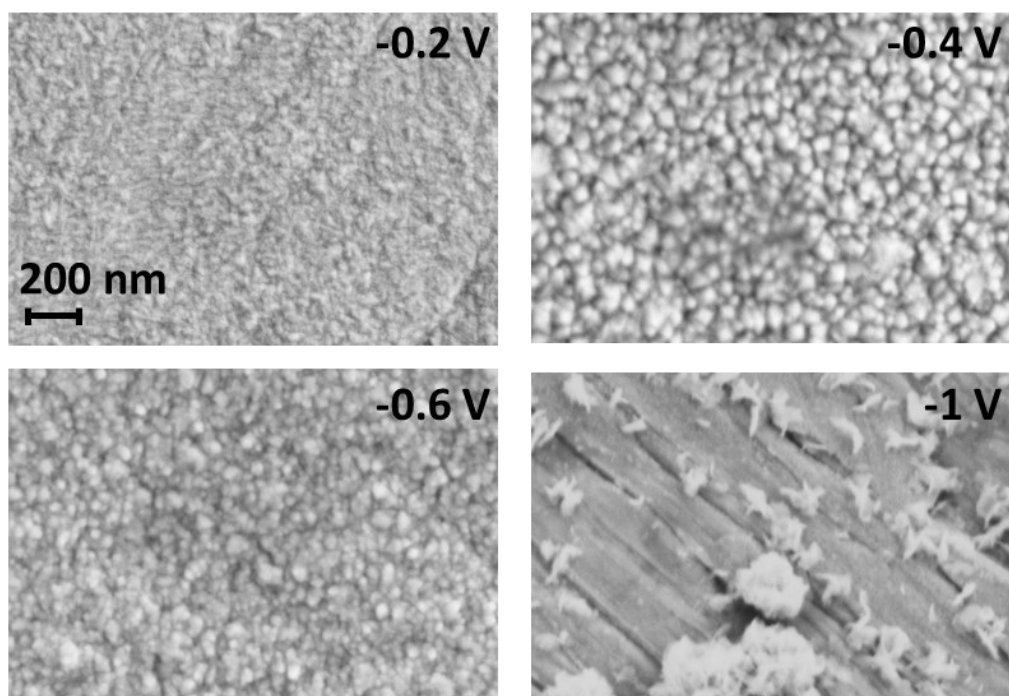


Figure 7.4 SEM images of Pt coatings obtained by applying different voltages, respectively  $-0.2$  V,  $-0.4$  V,  $-0.6$  V, and  $-1$  V, for a deposition time of 200 s. Image source: [67].

As shown in Figure 7.5, a fully covered electrode is obtained at  $-0.6$  V after a deposition time of 50 s, whereas the density of  $-1$  V samples reaches 100% only after a deposition time of 400 s. The nano-scale morphology of both  $-0.6$  V and  $-1$  V samples is not affected by the deposition time, as shown in Figure 7.6, which reports further SEM images at higher magnification for the 400 s, 600 s, and 800 s samples at  $-1$  V deposition voltage, and for the 200 s,  $-0.6$  V, respectively. Pt-NSs obtained by applying  $-1$  V are composed of petals with an average length of 96 nm, with no significant difference with different deposition times. The (200 s,  $-0.6$  V) Pt-NSs present spheres with an average diameter of 43 nm, and smaller spheres (on the surface of the larger spheres) with an average diameter of 6.9 nm. These results are coherent with those obtained in [79], where Pt petals with average size of 68 nm were obtained with a deposition for 200 s at  $-1$  V but on a Pt screen-printed electrode (SPE), and Pt spheres with average diameter of 52 nm were obtained with 200 s at  $-0.2$  V. This suggests that the obtained morphology tends to be granular rather than petal-like by lowering the absolute value of the deposition voltage.

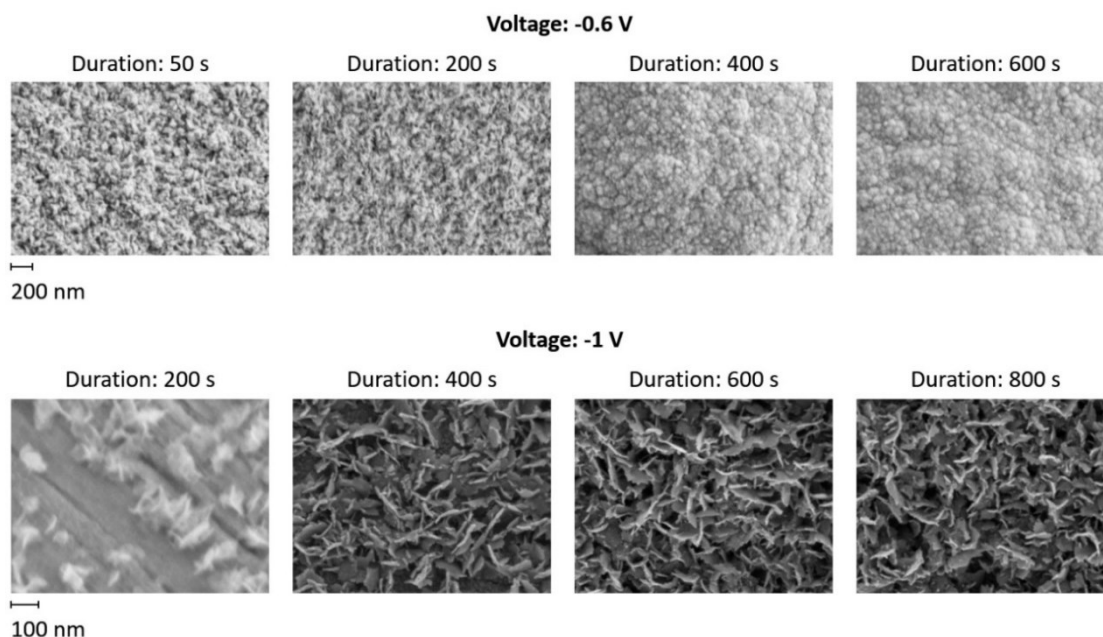


Figure 7.5 SEM images of Pt coatings at -0.6 V and -1 V, obtained at different deposition times. Image source: [67].

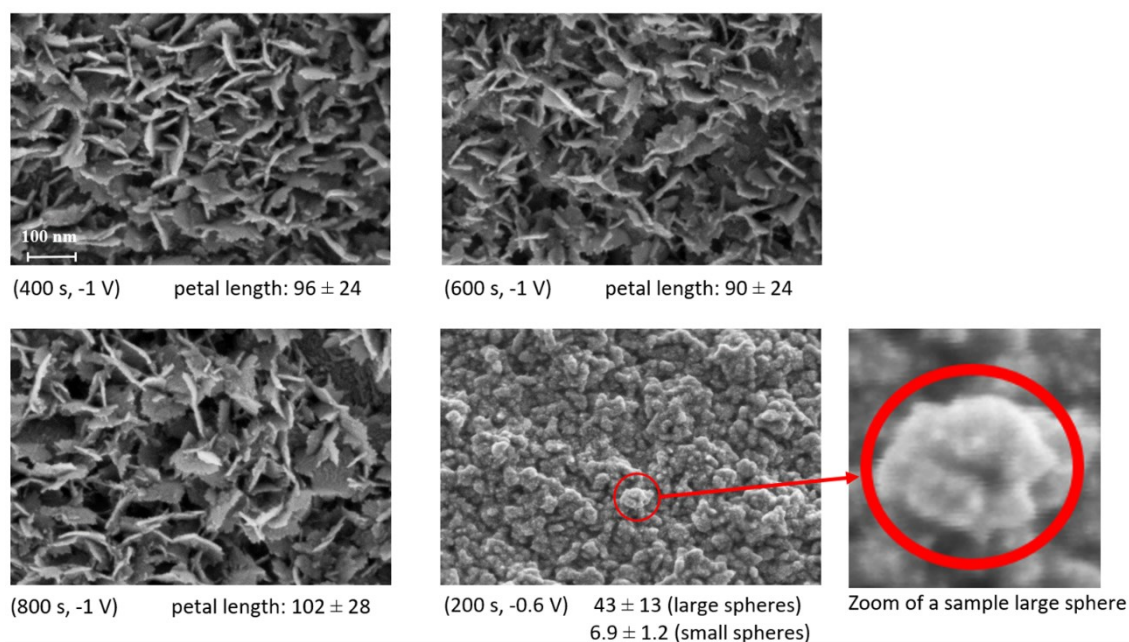


Figure 7.6 High magnification (350k) SEM images of the 400 s, 600 s, and 800 s samples at -1 V deposition voltage, and for the (200 s, -0.6 V) sample. On the bottom right, a zoom of a big sphere of (200 s, -0.6 V) SEM image: several smaller spheres are visible on the surface of the larger one. Nanostructure size is in [nm], expressed as mean  $\pm$  SD. Image source: [67].

### 7.3.3 Electrochemical Performances of the Sensors

An investigation of the effect by voltage deposition of Pt-NSs is carried out as well about the electrochemical performances of the realized sensors. Electrochemical measurements are performed on the samples to calculate sensitivity, LOD and linearity. Moreover, the long-term OCP drift after 14 hours with the KCl solution at highest concentration is calculated for each sample, in order to evaluate the time stability of the sensors. Table 7.1 shows the obtained values, reporting higher sensitivity and linearity for -0.6 V (see calibration curve in Figure 7.7), with a LOD of  $10^{-4}$  M, suitable for the physiological range of  $10^{-3} - 10^{-2}$  M. The comparison with the sensors realized with bare Pt electrodes coated with  $K^+$ -ISM as WE shows improved performances with the nanostructuring of Pt electrodes, in terms of both stability and sensitivity. The electrode with Pt-NSs obtained by applying -0.6 V presents lower OCP drift than the bare platinum electrode (Figure 7.8). The signals are also much more stable and definitely noisy than those obtained with both the bare electrode and the electrode with Pt-NSs deposited at -1 V. This could be explained with the low density of the Pt-NSs that cover the electrode surface in the second case. On the other hand, the stability improves significantly, accordingly to literature [79], when the electrode is fully covered by Pt-NSs.

Table 7.1 Performance parameters of the Pt nanostructured ISEs in  $10^{-7} - 10^{-1}$  M KCl solutions. Deposition time of 200 s, while stirring at 1200 rpm.

Deposition Voltage (V)	Sensitivity (mV/dec)	LOD (log[M])	Linearity (RMSE (mV))	Drift (mV) (*) After 14 h
bare Pt	38.2	-5.09	4.76	73.9
-0.2	50.0	-4.44	2.87	23.5
-0.4	57.1	-4.11	2.83	10.7
-0.6	<b>61.3</b>	-3.97	<b>1.55</b>	11.9
-1	51.9	-4.02	4.32	12.5

(\*) measured in  $10^{-1}$  M KCl.

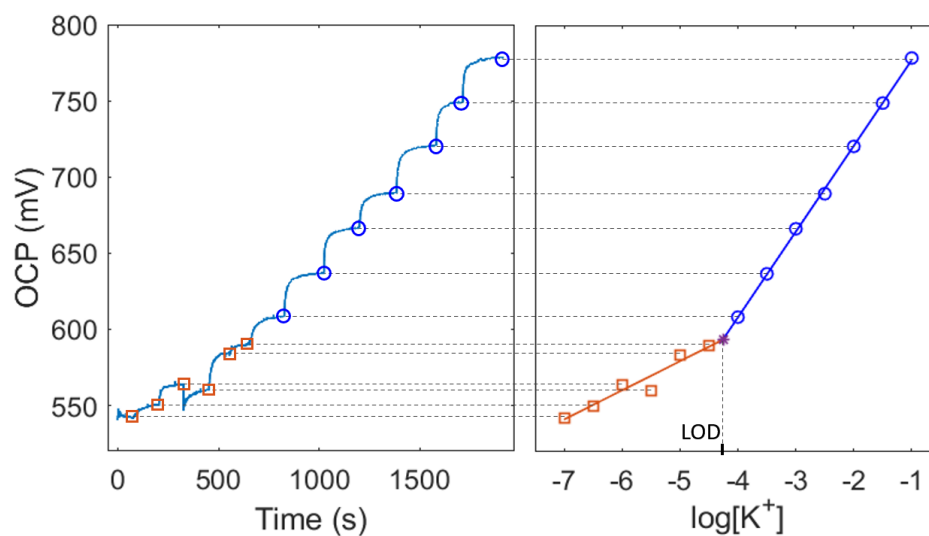


Figure 7.7 Calibration curve of one of the fabricated Pt nanostructured ISE obtained by applying  $-0.6$  V for 200 s. The star indicates the intersection between the two fitting lines, which corresponds to the LOD. Image source: [67].

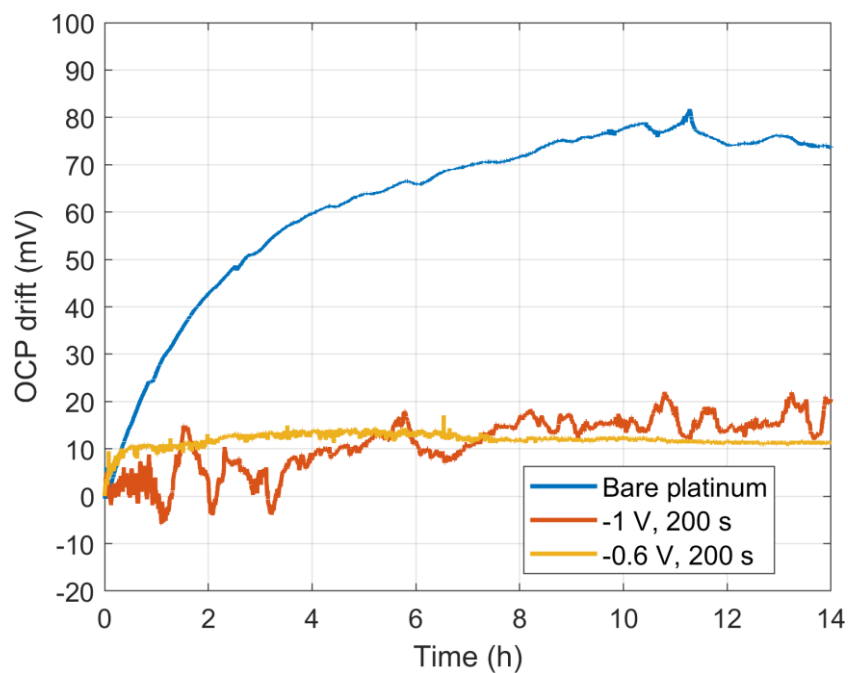


Figure 7.8 OCP drift in a concentration of  $10^{-1}$  M KCl for three fabricated ISEs: bare Pt substrate, and Pt nanostructured substrate with  $(-1$  V, 200 s) and  $(-0.6$  V, 200 s) deposition parameters, respectively. The not fully covered surface of the (200 s,  $-1$  V) sample resulted in a noisier signal. Image source: [67].

### 7.3.4 Optimization of Pt Nanostructuring Parameters with respect to $K^+$ Sensing Performances

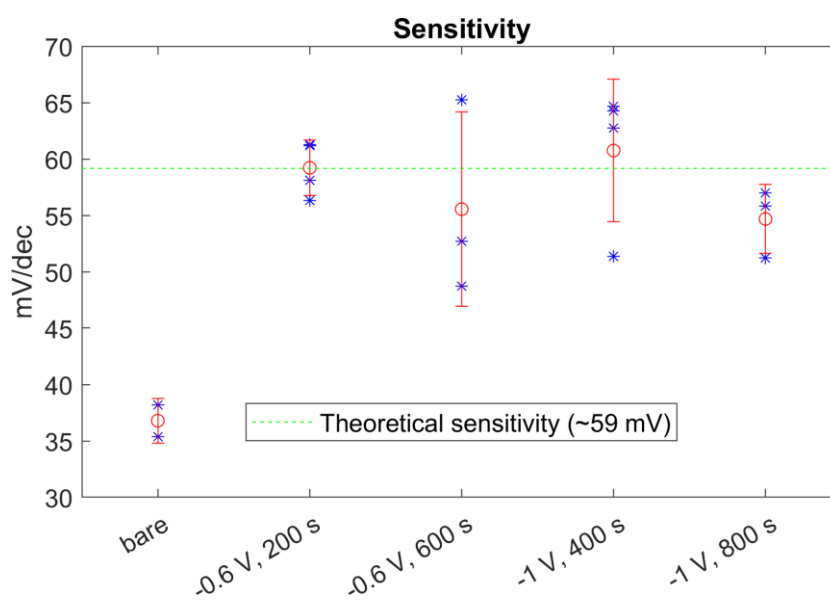
Since the main goal of this work is to optimize the fabrication of Pt-NSs needle-shaped sensors for  $K^+$  ions toward higher possible sensing performances, in this Section we investigate a possible correlation between sensors performances and electrodeposition parameters. Several other sensors are fabricated for each of the following four sets of deposition parameters: (200 s, -0.6 V), (600 s, -0.6 V), (400 s, -1 V), and (800 s, -1 V). Then, the wire WEs are coated with a  $K^+$  ISM, and the electrochemical measurements are performed. The experimental results are summarized in Table 7.2, which shows that the sensor performances in terms of sensitivity, LOD, time drift, and linearity are not significantly affected by deposition time and voltage. Among all configurations, the (200 s, -0.6 V) configuration shows lower mean and standard deviation (SD) drift after 14 h, and higher mean sensitivity with lower SD, whereas sensors fabricated with 800 s at -1 V present lower SD for sensitivity and LOD when compared to those with 400 s at -1 V. Overall, all performance metrics always improve with respect to bare Pt ISE, particularly regarding sensitivity and drift, as shown in Figure 7.9.

Despite the different Pt substrate geometry, sensitivity is always near the theoretical value of 59 mV/dec, and comparable with the one exhibited by the sensors with flat WE presented in [80] and obtained with the same electrodeposition procedure. The fabricated sensors exhibit high linearity, and the obtained LOD is at least one decade below the physiological concentration range. When the deposition time is longer than 200 s and 400 s for -0.6 V and -1 V, respectively, the fabrication procedure proves to be robust and the electrodeposition parameters do not significantly affect sensing performances. This makes the fabrication procedure quite flexible and it allows for arbitrarily choosing the electrodeposition parameters within these constraints, accordingly to other specific fabrication requirements.

Table 7.2 Statistics of performance parameters of the nanostructured samples for different deposition configurations. Results expressed in mean  $\pm$  SD. Comparison with literature is reported.

Configuration	Sensitivity (mV/dec)	LOD (log[K <sup>+</sup> ])	Linearity (RMSE (mV))	Drift (mV) (*)	
				After 1 h	After 14 h
Bare platinum	36.8 $\pm$ 2.0	-4.27 $\pm$ 1.15	1.02 $\pm$ 0.79	25.72 $\pm$ 0.68	68.7 $\pm$ 7.3
-0.6 V, 200 s	59.2 $\pm$ 2.4	-4.22 $\pm$ 0.33	2.48 $\pm$ 2.05	12.9 $\pm$ 9.8	7.9 $\pm$ 6.3
-0.6 V, 600 s	55.5 $\pm$ 8.6	-4.50 $\pm$ 0.53	2.17 $\pm$ 1.17	5.7 $\pm$ 5.2	20.4 $\pm$ 15.8
-1 V, 400 s	60.7 $\pm$ 6.3	-4.31 $\pm$ 0.48	2.39 $\pm$ 0.44	12.2 $\pm$ 13.3	22.0 $\pm$ 26.3
-1 V, 800 s	54.7 $\pm$ 3.1	-4.07 $\pm$ 0.05	2.05 $\pm$ 1.38	10.4 $\pm$ 10.2	24.4 $\pm$ 15.6
Literature [80]	56.1 $\pm$ 4.4	-5.42 $\pm$ 0.88	---	---	---

(\*) measured in  $10^{-1}$  M KCl.



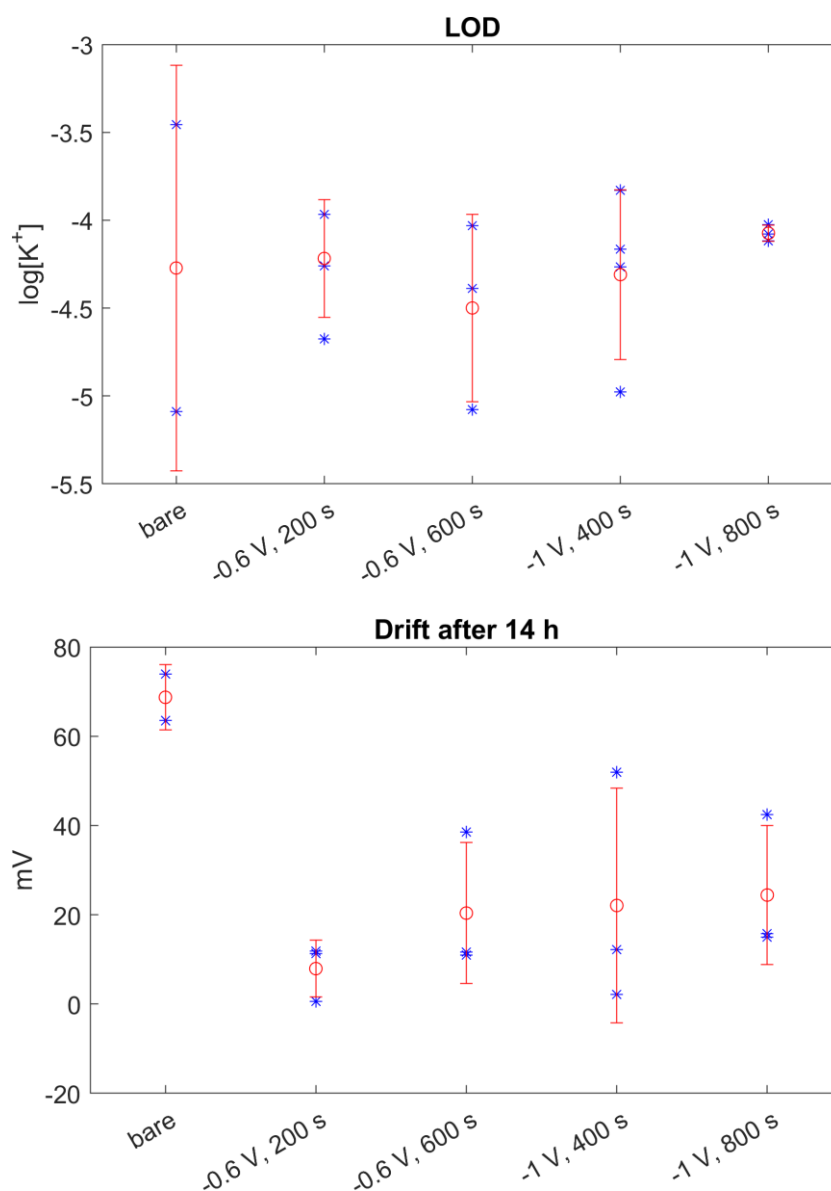


Figure 7.9. Sensitivity, LOD, and drift for the ISEs obtained with the four chosen deposition configurations with respect to bare Pt ISE. Single measurements (blue) and statistics (mean  $\pm$  SD in red) are shown. Image source: [67].

## 7.4 Chapter Conclusions

The need for miniaturization of Point-of-Care systems for ion sensing in biomedical field is leading toward the development of sensors based on all-solid-state ion-selective electrodes but realized onto working electrodes in very small sizes. The reason relies on typical applications where minimum invasiveness is a main issue to be considered, e.g.,

in surgery. Among several, potassium monitoring is key to be monitored during surgical procedures as a biomarker of organs failure. Hence, in this research we fabricate new miniaturized  $K^+$ -selective sensors with working electrodes obtained by electrodeposition of Pt-NSs on a very thin Pt wire with diameter of 0.1 mm, then in needle-shape. The use of nanostructured Pt-electrodes as ions solid contacts results in highly enhanced time stability, coherently with previous studies done on ion-sensors realized in past with planar working electrodes. We employ a simple and fast one-step template-free electrodeposition method, and we analyze for the first time the morphology of the obtained Pt-NSs depending on both deposition time and deposition voltage, as well as their effect on  $K^+$  sensing performances, in order to optimize the electrodeposition process. The Pt-NS are clearly visible and present granular or petal-like morphology, depending only on the voltage applied during the deposition.

Different deposition voltages produced differently shaped Pt-NSs. Although, their electrochemical behavior is very similar and does not lead to significant differences in terms of  $K^+$  sensing performances, thus proving the robustness of the fabrication procedure with respect to the electrodeposition parameters. The performed electrochemical measurements show high sensitivity, near to the theoretical value of 59 mV/dec, and comparable with the ones presented in [80], where larger flat sensors were fabricated with the same nanostructuring procedure. Compared to [80], our needle-shaped sensors show higher LOD, but still lower than  $10^{-4}$  M, which is one order of magnitude below the concentration range of interest, where the sensors exhibit high linearity.

Moreover, the minimum deposition time to cover the whole electrode surface varies with the applied voltage, increasing for higher applied voltage. Indeed, when applying -1 V the minimum deposition time results higher than that in [79], where Pt flat screen-printed working electrodes were employed as substrate instead of thin Pt wires. Thus, it remains demonstrated that working with different geometries and different working surfaces of the underneath substrates affects the nano-fabrication process and optimization.

Worth to note here also that the distinctive characteristics of the fabricated  $K^+$  sensors are the ease to fabricate and the very small sizes, so they could be easily and effectively integrated into surgical instruments to furnish diagnostics during surgical procedures, or into portable devices for real-time monitoring at the patient's bed.



# *Chapter 8*

---

## *Conclusions*

The use of tracking systems in medicine is an important aid in patient care, and ongoing research is focused on developing more performing systems, in order to provide accurate surgical instruments' position and orientation during surgical procedures. Huge effort is made on developing robust and effective methods to track surgical instruments.

This dissertation presented an innovative prototype of EMTS for surgical navigation, developed with the purpose of overcoming the limitation of current commercial systems, whose tracking distance is generally  $< 0.5$  m, thus allowing to place the FG far from the operating table. Several hardware improvements have been described, which led to enhanced system performances in terms of noise level reduction.

In Chapter 3, a new approach for assessing the position repeatability of EMTSs for surgical navigation has been presented. The repeatability error in sensor position estimation has been evaluated through the propagation of the voltage measurement error, at different distances from the FG, up to 700 mm, and the performances have been compared with results obtained from the tests executed on the Aurora system, which represents the state of the art of current commercial systems, obtaining SD values lower than 0.2 mm at 700 mm from the FG. A suitable assessment protocol has been defined, and a high-precision industrial robot has been used for the movement of the sensor and to provide accurate position references. The analysis methodology is based on the experimental measurement of field gradients, on the evaluation of coil sensor voltage noise and drift, and on the linear approximation of the voltage-position relation, which lead to an error propagation formula. The proposed analysis has the advantage of relating

the overall system performance to that of identifiable components which can be separately analyzed and optimized, on the one hand, and compared among different EMTSs, on the other.

In Chapter 4, position RMS error due to random components was then assessed in a volume of 400 mm x 500 mm x 400 mm, for different orientations of the magnetic sensor, instead of using linear trajectories with a single orientation as in Chapter 3. Results from experimentally estimated gradients are compared with those obtained by applying a model of the magnetic field where the coils are approximated as magnetic dipoles, leading to comparable performances. The obtained results show good overall system performance in the considered tracking volume, particularly when the sensor is oriented along the z-axis of the FG's reference system, meeting the specifications required for surgical applications in terms of repeatability. Some interesting aspects have been highlighted, showing the presence of regions where the position error is higher, which is due to magnetic field gradients, dependent on the spatial arrangement of the FG's transmitting coils and responsible for increased or reduced accuracy in the tracking volume.

In Chapter 5, tracking accuracy was evaluated by developing and testing an efficient reconstruction algorithm, to obtain accurate estimation of the instrument position and orientation. The results of position and angle estimation obtained by using two different cost functions were analyzed. The performance of the two techniques was analyzed and compared in a large measurement volume. The results obtained with the two estimation methods in terms of robustness and pose errors, allowed us to propose a new technique in which the best characteristic of both were easily combined. The analysis was performed by using simulated as well as experimental data. The results showed a mean position error of 2.2 mm, and a mean orientation error of  $0.5^\circ$  in a large volume with a distance from the FG center higher than 600 mm. In the same condition mean repeatability errors of 1 mm and  $0.25^\circ$ , respectively are obtained, which constitutes a noteworthy achievement, and are of the same order of those obtained in Chapter 4 by applying the estimation through gradients. As a further step the effect of variations in transmitting coils' excitation currents was studied, which cause magnetic field variations, resulting in noise in the induced voltage measured by the coil sensor. We quantified this effect by performing several simulations, then we proposed a solution to reduce this unwanted effect, by introducing the measurement of excitation currents in the position reconstruction algorithm. We performed different tests both on simulated and experimental data, proving the effectiveness and robustness of the proposed solution.

Finally, in Chapter 6 we proposed a virtual platform for assessing the performance of EMTSs for surgical navigation, showing in real-time how the various sources of error affect the accuracy of tracking distance estimation. This platform provides a useful tool

for supporting engineers during design and prototyping of EMTSs, since the high accuracy required from surgical applications is highly influenced by the design and arrangement of the transmitting coils of the FG. It is designed to be used in combination with the robotic arm, but can also be used in simulation mode without the need of the physical system, so that all parameters can be studied quickly and with much less hardware requirements. The platform permits to analyze system performances by adding noise components and simulating error sources, hence the robustness and the accuracy of the system and its weaknesses can be studied. Moreover, it can be particularly useful for system prototyping, by investigating the effects of system parameters (geometrical and electrical ones). The usefulness of the platform was demonstrated by performing simulations related to some practical cases, and it was validated by comparing simulation tests with that performed on the real EMTS prototype, obtaining comparable results. The platform will be applied in further studies to design the arrangement of the transmitting coils in order to obtain a particular distribution of the gradients and increase tracking distance and accuracy.

Chapter 7 concerned the last part of this dissertation, regarding the fabrication and characterization of an innovative needle-shaped sensor in sub-mm sizes with nanostructured platinum for ion-detection aims. It can be employed in biomedical applications, with particular regard to surgical procedures. The developed sensor has been tested for potassium detection, which is very important in cells functions assessment. For the first time in literature, the effects of electrodeposition voltage and time on the morphology of the nanostructures have been investigated. In past, similar nanofabrications have been successfully tried on usual planar geometries. Here, instead, Pt nanostructures growth is successfully shown on a thin Pt wire with diameter of 0.1 mm only. Both granular and petal-like nanostructures were obtained depending on the applied deposition voltage. The minimum time needed to nanostructure the whole electrode surface was found for each deposition voltage, suggesting that higher absolute voltage values need higher deposition time. The electrochemical measurements performed on the Pt nanostructured  $K^+$  ISEs showed enhanced stability over time with respect to non-nanostructured ISEs, and a Nernstian response with best sensitivity of  $59.2 \pm 2.4$  mV/decade in the linear range from  $10^{-4}$  to  $10^{-1}$  M. These good results encourage to further extend this study toward sensing of other ions by means of these microfabricated needle-shaped sensors, which can be easily integrated into surgical instruments to be then used for diagnosis during surgical operations.



# Appendix A

Let  $I_i$  be the current in the  $i$ -th coil, and  $I_{i,j}$  be the current in the  $i$ -th coil, filtered at the frequency  $f_j$ ,  $j = 1, \dots, 5$ .

Four different techniques to implement the control loop are defined, where the definition of the regulated variable changes each time [30].

- i) For the  $i$ -th coil, the regulated variable  $I'_i$  was evaluated by considering all the five harmonic components ( $j = 1, \dots, 5$ ) present in the current measured on the  $i$ -th channel. Then, the following expression was used:

$$I'_i = \sqrt{\sum_{j=1}^5 I_{i,j}^2}$$

- ii) For the  $i$ -th coil, the regulated variable  $I''_i$  was evaluated by considering current components in the five coils at the same frequency  $f_i$ . Then, the following expression was used:

$$I''_i = \sqrt{\sum_{l=1}^5 I_{l,i}^2}$$

- iii) For the  $i$ -th coil, only the current component at  $f_i$  was considered.

$$I'''_i = I_{i,i}$$

- iv) For the  $i$ -th coil, the measured current signal  $I_i$  was used directly, without any filtering.



# *Funding Acknowledgements*

This research was supported by project SINACH, “Integrated minimally-invasive surgical navigation systems”, funded by European Regional Development Fund, POR Puglia FESR - FSE 2014-2020, “InnoNetwork” call.

# *Personal Acknowledgements*

I ringraziamenti, a questo punto, sono più che superflui<sup>6</sup>.

---

<sup>6</sup> Ovviamente scherzo! I ringraziamenti sono più che doverosi e seguono alla pagina seguente.

Questi tre anni di dottorato sono stati decisamente ricchi, pieni di tante esperienze e di svolte decisive nella mia vita, che ricorderò sempre con grande affetto. Ciò che ho imparato è che ci sono delle scadenze da rispettare, delle aspettative da non deludere, ma vorrei assicurare tutti: capita di impegnarsi al massimo e non riuscire a rispettare le scadenze, o deludere le aspettative; ciò che conta è non identificarsi in quelle scadenze e aspettative. Il lavoro e lo studio fanno parte della vita, sono necessari e la riempiono anche di significato, ma non sono la vita. A chi pensa di non farcela, dico: tutti deludiamo aspettative: caduti ci si rialza; tutti abbiamo bisogno di aiuto: chiediamolo. Auguro di incontrare sul proprio cammino persone come quelle che ho incontrato io quando ho affrontato ostacoli che ritenevo troppo grandi per me.

Grazie anzitutto al meraviglioso gruppo dei Misuristi, in cui ho trovato presone che non smorzano le ali a chi vuol volare alto, ma si prendono cura e guardano anch'essi in alto!

Grazie Annie, Attilio, e Filippo: fin dall'inizio della mia esperienza accademica avete dimostrato attenzione e fiducia nei miei confronti, dandomi gli strumenti e le possibilità per far nascere in me il desiderio per la ricerca accademica. Non sono mancati i rimproveri e le correzioni (e non mancheranno in futuro), da cui cercherò sempre di trarre miglioramento e di ripagare la fiducia riposta in me.

Grazie Maurizio, Francesco, Nicola, Gregorio, e Pino, per le chiacchierate, i consigli, la presenza costante e la confidenza: da voi c'è solo da imparare.

Grazie, mitici giovani dottorandi (ormai lo possiamo dire, da oggi siamo ex colleghi, cambia la gerarchia), amici più che colleghi: Marco, compagno di avventure ormai da quattro anni, un'amicizia che le conferenze e l'esperienza in Svizzera hanno fortificato ancor di più: le marachelle ormai sono all'ordine del giorno; Luisa, seguita dai tempi della sua tesi triennale, e ora gioiello e splendida presenza femminile del nostro gruppo: l'affidabilità fatta persona; Daniel, un concentrato di tecnica, passione e determinazione: se hai bisogno di aiuto, chiedi a lui (che non manca di chiedere aiuto quando ne ha bisogno); Ivano, il giovanissimo del gruppo, propositivo, a volte (spesso) incazzato, a tratti trasgressivo, ma sempre modesto e disponibile: l'ultima ruota solo in termini di età. Grazie Donato, mio collega Matlab Ambassador, o meglio, io tuo collega, per qualche mese: la tua aria da manager si fiuta da lontano.

Grazie, Gianni, per le bellissime esperienze di ricerca che spero riprenderemo quanto prima, per l'amicizia, per il trio unico con Marco, per le disavventure comuni con la segreteria, per le chiacchierate serali sfruttando il fuso orario, e per le cenette da Seppcol, anch'esse da ripetere.

Grazie, caro Sandro, per aver ospitato me e Marco durante il nostro soggiorno a Neuchâtel: un professionista competente, un uomo attento alle necessità e con una grande fiducia nei giovani ricercatori. Sono grato per l'esperienza vissuta, da te ho appreso molto in termini umani e professionali, e ritengo con soddisfazione di aver migliorato molto il mio profilo di ricercatore. Grazie anche ai cari amici Ali, Francesca, Giuliano e Gianluca per il bel tempo passato insieme a Neuchâtel: a voi auguro il meglio per l'avvenire.

Grazie alla comunità neocatecumenale di Sant'Antonio: siete diventati una famiglia per me e Federica, ci avete visto crescere in questi due anni di matrimonio. Qui Dio ci ha fatto un grande dono, che abbiamo avuto la grazia di accogliere. Grazie di cuore.

Grazie Papà e Mamma: da quando sono diventato padre non riesco a fare a meno di pensare ogni giorno a quanto amore avete avuto e avete per me, come anch'io verso i miei figli. Chi sono oggi e ciò che ho potuto realizzare, è in gran parte grazie a voi, i miei genitori, che in tutto avete provveduto a me e mi avete dato tutto ciò che avete potuto, anche quando io non me ne sono reso conto. A voi il mio grazie, per la vita.

Grazie Samuele e Manuel, fratelli miei. Soprattutto ora che sono padre, e voi zii, riconosco ancor di più la meraviglia di avere dei fratelli, che ha reso la mia infanzia e giovinezza piena, e mi ha portato a maturare. Non sempre vi ho compreso come dovuto, ma da fratello maggiore sappiate che sempre la vostra presenza e il vedervi felici è per me una grande gioia, una ferma sicurezza.

Grazie Nonna, che fai merenda con tè e panettone come la regina Elisabetta, che dimentichi presto ma ricordi ciò che conta: sei una radice che conserva la bellezza delle nostre origini, incastrata nel nostro bel presente.

Grazie Federica, mia sposa, dono immenso che da Dio ho ricevuto, accolto, e che sempre voglio custodire. Sei la meraviglia che si fa carne nella mia vita. Grazie per la tua forte fiducia in me, per il tuo essere donna, moglie, madre, per il tuo essere semplice nelle cose più complicate, e a volte complicata nelle cose semplici. Grazie per il tuo metterti in gioco, per il tuo entusiasmo, per i tuoi timori, per la tua bella genuinità. Ti amo.

Grazie Tommaso Emanuele, figlio nostro: ci hai meravigliato, ci hai stravolto, ci hai indicato il Cielo, e dolcemente ci accompagna. Ti ameremo sempre.

Grazie Stefano Maria, figlio nostro, sorriso di Dio nella nostra famiglia. Un uragano di tenerezza, amore, gioia: tu ci insegni il sacrificio, la pazienza, l'amore, la bellezza, la responsabilità. Ti ameremo sempre.

*“La famiglia è lo specchio in cui Dio si guarda e vede i due miracoli più belli che ha fatto: donare la vita e donare l'amore.”*

(Giovanni Paolo II)

# References

- [1] T. Peters and K. Cleary, *Image-guided interventions: Technology and applications*. Boston, MA: Springer US, 2008, p. 557. doi: 10.1007/978-0-387-73858-1.
- [2] H. Alemdar and C. Ersoy, “Wireless sensor networks for healthcare: A survey,” *Comput. Netw.*, vol. 54, no. 15, pp. 2688–2710, 2010, doi: 10.1016/j.comnet.2010.05.003.
- [3] O. Aziz *et al.*, “A pervasive body sensor network for measuring postoperative recovery at home,” *Surg. Innov.*, vol. 14, no. 2, pp. 83–90, 2007, doi: 10.1177/1553350607302326.
- [4] X. Chen, N. Bao, J. Li, and Y. Kang, “A review of surgery navigation system based on ultrasound guidance,” in *2012 IEEE International Conference on Information and Automation, ICIA 2012*, Jun. 2012, pp. 882–886. doi: 10.1109/ICInfA.2012.6246906.
- [5] G. Andria *et al.*, “Dosimetric Characterization and Image Quality Assessment in Breast Tomosynthesis,” *IEEE Trans. Instrum. Meas.*, vol. 66, no. 10, pp. 2535–2544, Oct. 2017, doi: 10.1109/TIM.2017.2692318.
- [6] M. C. Paul and A. Larman, “Investigation of spiral blood flow in a model of arterial stenosis,” *Med. Eng. Phys.*, vol. 31, no. 9, pp. 1195–1203, Nov. 2009, doi: 10.1016/j.medengphy.2009.07.008.
- [7] L. Fabbiano, G. Vacca, R. Morello, and C. De Capua, “An Innovative Strategy for Correctly Interpreting Simultaneous Acquisition of EEG Signals and FMRI Images,” *IEEE Sens. J.*, vol. 13, no. 9, pp. 3175–3181, Sep. 2013, doi: 10.1109/JSEN.2013.2261294.
- [8] G. Bachar, J. H. Siewerdsen, M. J. Daly, D. A. Jaffray, and J. C. Irish, “Image quality and localization accuracy in C-arm tomosynthesis-guided head and neck surgery,” *Med. Phys.*, vol. 34, no. 12, pp. 4664–4677, Nov. 2007, doi: 10.1118/1.2799492.
- [9] G. Andria, F. Attivissimo, A. Di Nisio, A. M. L. L. Lanzolla, G. Guglielmi, and R. Terlizzi, “Dose optimization in chest radiography: System and model characterization via experimental investigation,” *IEEE Trans. Instrum. Meas.*, vol. 63, no. 5, pp. 1163–1170, May 2014, doi: 10.1109/TIM.2013.2282411.
- [10] L. M. Galantucci, G. Percoco, F. Lavecchia, and E. Di Gioia, “Noninvasive computerized scanning method for the correlation between the facial soft and hard tissues for an integrated three-dimensional anthropometry and cephalometry,” *J.*

- Craniofac. Surg.*, vol. 24, no. 3, pp. 797–804, May 2013, doi: 10.1097/SCS.0b013e31828dcc81.
- [11] N. Casap, E. Tarazi, A. Wexler, U. Sonnenfeld, and J. Lustmann, “Intraoperative computerized navigation for flapless implant surgery and immediate loading in the edentulous mandible,” *J. Prosthet. Dent.*, vol. 94, no. 2, p. 201, Aug. 2005, doi: 10.1016/j.prosdent.2005.04.022.
- [12] G. Andria, F. Attivissimo, G. Cavone, and A. M. L. Lanzolla, “Acquisition times in magnetic resonance imaging: Optimization in clinical use,” *IEEE Trans. Instrum. Meas.*, vol. 58, no. 9, pp. 3140–3148, Sep. 2009, doi: 10.1109/TIM.2009.2016888.
- [13] A. M. Franz, T. Haidegger, W. Birkfellner, K. Cleary, T. M. Peters, and L. Maier-Hein, “Electromagnetic tracking in medicine -A review of technology, validation, and applications,” *IEEE Trans. Med. Imaging*, vol. 33, no. 8, pp. 1702–1725, Aug. 2014, doi: 10.1109/TMI.2014.2321777.
- [14] F. H. Raab, “Quasi-Static Magnetic-Field Technique for Determining Position and Orientation,” *IEEE Trans. Geosci. Remote Sens.*, vol. GE-19, no. 4, pp. 235–243, 1981, doi: 10.1109/TGRS.1981.350378.
- [15] G. Welch and E. Foxlin, “Motion tracking: No silver bullet, but a respectable arsenal,” *IEEE Comput. Graph. Appl.*, vol. 22, no. 6, pp. 24–38, 2002, doi: 10.1109/MCG.2002.1046626.
- [16] H. Qasem and L. Reindl, “Precise wireless indoor localization with trilateration based on microwave backscatter,” in *IEEE Wireless and Microwave Technology Conference, WAMICON 2006*, 2006. doi: 10.1109/WAMICON.2006.351899.
- [17] M. Salucci, L. Poli, N. Anselmi, and A. Massa, “Multifrequency Particle Swarm Optimization for Enhanced Multiresolution GPR Microwave Imaging,” *IEEE Trans. Geosci. Remote Sens.*, vol. 55, no. 3, pp. 1305–1317, 2017, doi: 10.1109/TGRS.2016.2622061.
- [18] A. Cataldo, G. Cannazza, N. Giaquinto, A. Trotta, and G. Andria, “Microwave TDR for real-time control of intravenous drip infusions,” *IEEE Trans. Instrum. Meas.*, vol. 61, no. 7, pp. 1866–1873, 2012, doi: 10.1109/TIM.2012.2192346.
- [19] A. M. A. M. Franz, A. Seitel, D. Cheray, and L. Maier-Hein, “Polhemus EM tracked Micro Sensor for CT-guided interventions,” *Med. Phys.*, vol. 46, no. 1, pp. 15–24, 2019, doi: 10.1002/mp.13280.
- [20] “Polhemus—Accessories Polhemus.” 2004. [Online]. Available: [https://est-kl.com/images/PDF/Polhemus/Accessories\\_brochure.pdf](https://est-kl.com/images/PDF/Polhemus/Accessories_brochure.pdf)
- [21] G. De Angelis *et al.*, “An Indoor AC Magnetic Positioning System,” *IEEE Trans. Instrum. Meas.*, vol. 64, no. 5, pp. 1267–1275, May 2015, doi: 10.1109/TIM.2014.2381353.
- [22] L. T. De Paolis, M. Pulimeno, L. Ramundo, and G. Aloisio, “Human anatomy visualization and navigation system for image-guided surgery,” in *2009 9th International Conference on Information Technology and Applications in Biomedicine*, Nov. 2009, pp. 1–4. doi: 10.1109/ITAB.2009.5394338.
- [23] A. M. Franz, T. Haidegger, W. Birkfellner, K. Cleary, T. M. Peters, and L. Maier-Hein, “Electromagnetic tracking in medicine -A review of technology, validation,

- and applications,” *IEEE Trans. Med. Imaging*, vol. 33, no. 8, pp. 1702–1725, Aug. 2014, doi: 10.1109/TMI.2014.2321777.
- [24] G. Andria, F. Attivissimo, A. Di Nisio, A. Trotta, S. M. Camporeale, and P. Pappalardi, “Design of a microwave sensor for measurement of water in fuel contamination,” *Meas. J. Int. Meas. Confed.*, vol. 136, pp. 74–81, 2019, doi: 10.1016/j.measurement.2018.12.076.
- [25] S. Tumanski, “Induction coil sensors—a review,” *Meas. Sci. Technol.*, vol. 18, no. 3, pp. R31–R46, Jan. 2007, doi: 10.1088/0957-0233/18/3/R01.
- [26] V. Pasku, A. De Angelis, G. De Angelis, A. Moschitta, and P. Carbone, “Magnetic Field Analysis for 3-D Positioning Applications,” *IEEE Trans. Instrum. Meas.*, vol. 66, no. 5, pp. 935–943, May 2017, doi: 10.1109/TIM.2017.2682738.
- [27] F. Santoni, A. De Angelis, I. Skog, A. Moschitta, and P. Carbone, “Calibration and Characterization of a Magnetic Positioning System Using a Robotic Arm,” *IEEE Trans. Instrum. Meas.*, vol. 68, no. 5, pp. 1494–1502, May 2019, doi: 10.1109/TIM.2018.2885590.
- [28] F. Attivissimo, A. D. Nisio, A. M. L. Lanzolla, and **M. A. Ragolia**, “Analysis of Position Estimation Techniques in a Surgical EM Tracking System,” *IEEE Sens. J.*, vol. 21, no. 13, pp. 14389–14396, Jul. 2021, doi: 10.1109/JSEN.2020.3042647.
- [29] **M. A. Ragolia**, F. Attivissimo, A. Di Nisio, A. M. L. Lanzolla, and M. Scarpetta, “Reducing effect of magnetic field noise on sensor position estimation in surgical EM tracking,” in *2021 IEEE International Symposium on Medical Measurements and Applications (MeMeA)*, Jun. 2021, pp. 1–6. doi: 10.1109/MeMeA52024.2021.9478723.
- [30] A. Plotkin, O. Shafrir, E. Paperno, and D. M. Kaplan, “Magnetic eye tracking: A new approach employing a planar transmitter,” *IEEE Trans. Biomed. Eng.*, vol. 57, no. 5, pp. 1209–1215, 2010, doi: 10.1109/TBME.2009.2038495.
- [31] **M. A. Ragolia et al.**, “Performance analysis of an electromagnetic tracking system for surgical navigation,” in *Medical Measurements and Applications, MeMeA 2019 - Symposium Proceedings*, Jun. 2019, pp. 1–6. doi: 10.1109/MeMeA.2019.8802220.
- [32] G. Andria, F. Attivissimo, A. Di Nisio, A. M. L. Lanzolla, and **M. A. Ragolia**, “Assessment of position repeatability error in an electromagnetic tracking system for surgical navigation,” *Sens. Switz.*, vol. 20, no. 4, pp. 961–961, Feb. 2020, doi: 10.3390/s20040961.
- [33] G. Andria, F. Attivissimo, A. Di Nisio, A. M. L. Lanzolla, P. Larizza, and S. Selicato, “Development and performance evaluation of an electromagnetic tracking system for surgery navigation,” *Meas. J. Int. Meas. Confed.*, vol. 148, p. 106916, Dec. 2019, doi: 10.1016/j.measurement.2019.106916.
- [34] F. Attivissimo, A. M. L. Lanzolla, S. Carlone, P. Larizza, and G. Brunetti, “A novel electromagnetic tracking system for surgery navigation,” *Comput. Assist. Surg.*, vol. 23, no. 1, pp. 42–52, Jan. 2018, doi: 10.1080/24699322.2018.1529199.
- [35] “Aurora 5DOF Sensor.” <https://www.ndigital.com/electromagnetic-tracking-technology/aurora/aurora-sensors/> (accessed Sep. 19, 2022).
- [36] M. Industrial, “RV-2F-D Series Standard Specifications Manual”.

- [37] Z. Duan, Z. Yuan, X. Liao, W. Si, and J. Zhao, "3D tracking and positioning of surgical instruments in virtual surgery simulation," *J. Multimed.*, vol. 6, no. 6, pp. 502–509, 2011, doi: 10.4304/jmm.6.6.
- [38] F. Attivissimo, A. Di Nisio, C. G. C. C. G. C. Carducci, and M. Spadavecchia, "Fast Thermal Characterization of Thermoelectric Modules Using Infrared Camera," *IEEE Trans. Instrum. Meas.*, vol. 66, no. 2, pp. 305–314, 2017, doi: 10.1109/TIM.2016.2631818.
- [39] H. Shekhar, J. S. J. Kumar, V. Ashok, and A. V. Juliet, "Applied Medical Informatics Using LabVIEW," *Int. J. Comput. Sci. Eng.*, vol. 1, no. 2, pp. 198–202, 2010.
- [40] **M. A. Ragolia**, F. Attivissimo, A. Di Nisio, A. M. L. Lanzolla, and M. Scarpetta, "A virtual platform for real-time performance analysis of electromagnetic tracking systems for surgical navigation," *ACTA IMEKO*, vol. 10, no. 4, pp. 103–103, Dec. 2021, doi: 10.21014/acta\_imeko.v10i4.1191.
- [41] IEEE and I. S. C. C. 28, *IEEE Standard for Safety Levels With Respect to Human Exposure to Electromagnetic Fields, 0-3 kHz*, vol. 2002, no. September. 2002.
- [42] IEEE Standards, *IEEE Standard for Safety Levels With Respect to Human Exposure to Radio Frequency Electromagnetic Fields, 3 kHz to 300 GHz*, vol. 2005, no. April. 2006. doi: 10.1109/IEEESTD.2006.99501.
- [43] G. De Angelis, A. De Angelis, M. Dionigi, M. Mongiardo, A. Moschitta, and P. Carbone, "An accurate Indoor Position-measurement system using mutually coupled resonating circuits," in *2014 IEEE International Instrumentation and Measurement Technology Conference (I2MTC) Proceedings*, May 2014, pp. 844–849. doi: 10.1109/I2MTC.2014.6860862.
- [44] C. G. C. Carducci, A. Di Nisio, F. Attivissimo, and A. Trotta, "Dynamic Error Correction for Magnetic Property Measurement," *IEEE Trans. Instrum. Meas.*, vol. 69, no. 3, pp. 836–844, 2020, doi: 10.1109/TIM.2019.2907037.
- [45] K. O'Donoghue, "Electromagnetic tracking and steering for catheter navigation," Doctoral thesis, University College Cork, 2014. Accessed: Oct. 04, 2022. [Online]. Available: <https://cora.ucc.ie/handle/10468/2025>
- [46] T. Koivukangas, J. P. A. P. Katisko, and J. P. Koivukangas, "Technical accuracy of optical and the electromagnetic tracking systems," *SpringerPlus*, vol. 2, no. 1, pp. 1–7, Dec. 2013, doi: 10.1186/2193-1801-2-90.
- [47] "Aurora Field Generators - NDI." <https://www.ndigital.com/electromagnetic-tracking-technology/aurora/aurora-field-generators/> (accessed Sep. 20, 2022).
- [48] **M. A. Ragolia**, F. Attivissimo, A. D. Nisio, and A. Maria Lucia Lanzolla, "Evaluation of position RMS error from magnetic field gradient for surgical em tracking systems," in *I2MTC 2020 - International Instrumentation and Measurement Technology Conference, Proceedings*, May 2020, pp. 1–6. doi: 10.1109/I2MTC43012.2020.9128837.
- [49] **M. A. Ragolia**, F. Attivissimo, A. Di Nisio, and A. Maria Lucia Lanzolla, "Assessment of position repeatability of surgical EM tracking systems employing magnetic field model," in *2020 IEEE International Symposium on Medical*

- Measurements and Applications (MeMeA)*, Jun. 2020, pp. 1–6. doi: 10.1109/MeMeA49120.2020.9137161.
- [50] R. Morello and C. De Capua, “An ISO/IEC/IEEE 21451 compliant algorithm for detecting sensor faults: An approach based on repeatability and accuracy,” *IEEE Sens. J.*, vol. 15, no. 5, pp. 2541–2548, 2015, doi: 10.1109/JSEN.2014.2361697.
- [51] G. M. D’Aucelli, N. Giaquinto, C. Guarnieri Caló Carducci, M. Spadavecchia, and A. Trotta, “Uncertainty evaluation of the Unified Method for thermo-electric module characterization,” *Meas. J. Int. Meas. Confed.*, vol. 131, pp. 751–763, Jan. 2019, doi: 10.1016/j.measurement.2018.08.070.
- [52] T. Koivukangas, “Methods for determination of the accuracy of surgical guidance devices: a study in the region of neurosurgical interest,” University of Oulu, Finland, 2012. [Online]. Available: <http://urn.fi/urn:isbn:9789514299049>
- [53] J. C. Lagarias, J. A. Reeds, M. H. Wright, and P. E. Wright, “Convergence properties of the Nelder-Mead simplex method in low dimensions,” *SIAM J. Optim.*, vol. 9, no. 1, pp. 112–147, 1998, doi: 10.1137/S1052623496303470.
- [54] D. D. Frantz, A. D. Wiles, S. E. Leis, and S. R. Kirsch, “Accuracy assessment protocols for electromagnetic tracking systems,” *Phys. Med. Biol.*, vol. 48, no. 14, pp. 2241–2251, 2003, doi: 10.1088/0031-9155/48/14/314.
- [55] G. De Angelis, A. De Angelis, A. Moschitta, and P. Carbone, “Comparison of measurement models for 3D magnetic localization and tracking,” *Sens. Switz.*, vol. 17, no. 11, 2017, doi: 10.3390/s17112527.
- [56] R. H. Byrd, J. C. Gilbert, and J. Nocedal, “A trust region method based on interior point techniques for nonlinear programming,” *Math. Program. Ser. B*, vol. 89, no. 1, pp. 149–185, 2000, doi: 10.1007/PL00011391.
- [57] V. V. Kindratenko, “A survey of electromagnetic position tracker calibration techniques,” *Virtual Real.*, vol. 5, no. 3, pp. 169–182, 2000, doi: 10.1007/BF01409422.
- [58] S. Goll and A. Borisov, “Interactive model of a magnetic field reconstruction stand for the debugging of mobile robot navigation algorithms using magnetometer data,” *Acta IMEKO*, vol. 8, no. 4, pp. 47–53, 2019, doi: 10.21014/acta\_imeko.v8i4.688.
- [59] E. Petritoli, F. Leccese, L. Ciani, and G. S. Spagnolo, “Probe position error compensation in near-field to far-field pattern measurements,” in *2019 IEEE International Workshop on Metrology for AeroSpace, MetroAeroSpace 2019 - Proceedings*, 2019, pp. 214–217. doi: 10.1109/MetroAeroSpace.2019.8869674.
- [60] A. Sorriente *et al.*, “Optical and Electromagnetic Tracking Systems for Biomedical Applications: A Critical Review on Potentialities and Limitations,” *IEEE Rev. Biomed. Eng.*, vol. 13, pp. 212–232, 2020, doi: 10.1109/RBME.2019.2939091.
- [61] Y. Qi, H. Sadjadi, C. T. Yeo, K. Hashtrudi-Zaad, and G. Fichtinger, “Electromagnetic tracking performance analysis and optimization,” in *2014 36th Annual International Conference of the IEEE Engineering in Medicine and Biology Society, EMBC 2014*, 2014, pp. 6534–6538. doi: 10.1109/EMBC.2014.6945125.
- [62] J. B. Hummel *et al.*, “Design and application of an assessment protocol for electromagnetic tracking systems,” *Med. Phys.*, vol. 32, no. 7Part1, pp. 2371–2379, 2005, doi: 10.1118/1.1944327.

- [63] E. Wilson *et al.*, “A hardware and software protocol for the evaluation of electromagnetic tracker accuracy in the clinical environment: a multi-center study,” in *Medical Imaging 2007: Visualization and Image-Guided Procedures*, Mar. 2007, vol. 6509, pp. 960–970. doi: 10.1117/12.712701.
- [64] T. Haidegger, B. Sirokai, G. Fenyvesi, L. Kovács, B. Benyó, and Z. Benyó, “Repeatable assessment protocol for electromagnetic trackers,” in *Medical Imaging 2012: Image-Guided Procedures, Robotic Interventions, and Modeling*, Feb. 2012, vol. 8316, pp. 562–570. doi: 10.1117/12.911673.
- [65] P. Catala-Lehnen, J. V. Nchtern, D. Briem, T. Klink, J. M. Rueger, and W. Lehmann, “Comparison of 2D and 3D navigation techniques for percutaneous screw insertion into the scaphoid: Results of an experimental cadaver study,” *Comput. Aided Surg.*, vol. 16, no. 6, pp. 280–287, 2011, doi: 10.3109/10929088.2011.621092.
- [66] M. Li, C. Hansen, and G. Rose, “A simulator for advanced analysis of a 5-DOF EM tracking systems in use for image-guided surgery,” *Int. J. Comput. Assist. Radiol. Surg.*, vol. 12, no. 12, pp. 2217–2229, 2017, doi: 10.1007/s11548-017-1662-x.
- [67] A. Di Nisio, N. Giaquinto, A. M. L. Lanzolla, **M. A. Ragolia**, M. Scarpetta, and S. Carrara, “Platinum Nanostructured Needle-Shaped Sensors for Ion Detection in Biomedical Applications,” *IEEE Sens. J.*, vol. 22, no. 23, pp. 22404–22412, Dec. 2022, doi: 10.1109/JSEN.2022.3216682.
- [68] F. Criscuolo, M. I. N. Hanitra, I. Taurino, S. Carrara, and G. De Micheli, “All-Solid-State Ion-Selective Electrodes: A Tutorial for Correct Practice,” *IEEE Sens. J.*, vol. 21, no. 20, pp. 22143–22154, Oct. 2021, doi: 10.1109/JSEN.2021.3099209.
- [69] M. Parrilla *et al.*, “Wearable All-Solid-State Potentiometric Microneedle Patch for Intradermal Potassium Detection,” *Anal. Chem.*, vol. 91, no. 2, pp. 1578–1586, Jan. 2019, doi: 10.1021/acs.analchem.8b04877.
- [70] J. Zhai, Y. Zhang, D. Zhao, L. Kou, and G. Zhao, “In vivo monitoring of calcium ions in rat cerebrospinal fluid using an all-solid-state acupuncture needle based potentiometric microelectrode,” *Anal. Chim. Acta*, vol. 1191, p. 339209, Jan. 2022, doi: 10.1016/j.aca.2021.339209.
- [71] J. Church, S. M. Armas, P. K. Patel, K. Chumbimuni-Torres, and W. H. Lee, “Development and Characterization of Needle-type Ion-selective Microsensors for in situ Determination of Foliar Uptake of Zn<sup>2+</sup> in Citrus Plants,” *Electroanalysis*, vol. 30, no. 4, pp. 626–632, 2018, doi: 10.1002/elan.201700697.
- [72] M. Abunasar Miah, Y. Nakagawa, R. Tanimoto, R. Shinjo, M. Kondo, and H. Suzuki, “Mass-producible disposable needle-type ion-selective electrodes for plant research,” *RSC Adv.*, vol. 9, no. 52, pp. 30309–30316, 2019, doi: 10.1039/C9RA05477D.
- [73] H. Han, D. Pan, Y. Li, J. Wang, and C. Wang, “Stripping Voltammetric Determination of Lead in Coastal Waters With a Functional Micro-Needle Electrode,” *Front. Mar. Sci.*, vol. 7, 2020, Accessed: May 31, 2022. [Online]. Available: <https://www.frontiersin.org/article/10.3389/fmars.2020.00196>
- [74] G. Zhao, R. Liang, F. Wang, J. Ding, and W. Qin, “An all-solid-state potentiometric microelectrode for detection of copper in coastal sediment pore water,” *Sens.*

- Actuators B Chem.*, vol. 279, pp. 369–373, Jan. 2019, doi: 10.1016/j.snb.2018.09.125.
- [75] I. Taurino *et al.*, “Platinum nanopetal-based potassium sensors for acute cell death monitoring,” *RSC Adv.*, vol. 6, no. 46, pp. 40517–40526, 2016, doi: 10.1039/C6RA01664B.
- [76] F. Criscuolo, I. Taurino, F. Stradolini, S. Carrara, and G. De Micheli, “Highly-stable Li<sup>+</sup> ion-selective electrodes based on noble metal nanostructured layers as solid-contacts,” *Anal. Chim. Acta*, vol. 1027, pp. 22–32, Oct. 2018, doi: 10.1016/j.aca.2018.04.062.
- [77] E. M. Hussien and A. R. Derar, “Highly-Stable Miniaturized Pt-Nanostructures/Pt Coated Wire Ion Selective Electrode for Fluoxetine HCl,” *IEEE Sens. J.*, vol. 20, no. 12, pp. 6263–6269, Jun. 2020, doi: 10.1109/JSEN.2020.2977529.
- [78] Q. Zhu *et al.*, “3D bimetallic Au/Pt nanoflowers decorated needle-type microelectrode for direct in situ monitoring of ATP secreted from living cells,” *Biosens. Bioelectron.*, vol. 153, p. 112019, Apr. 2020, doi: 10.1016/j.bios.2020.112019.
- [79] I. Taurino, G. Sanz , F. Mazzei, G. Favero, G. De Micheli, and S. Carrara, “Fast synthesis of platinum nanopetals and nanospheres for highly-sensitive non-enzymatic detection of glucose and selective sensing of ions,” *Sci. Rep.*, vol. 5, no. 1, p. 15277, Dec. 2015, doi: 10.1038/srep15277.
- [80] F. Criscuolo *et al.*, “Wearable multifunctional sweat-sensing system for efficient healthcare monitoring,” *Sens. Actuators B Chem.*, vol. 328, p. 129017, Feb. 2021, doi: 10.1016/j.snb.2020.129017.
- [81] P. C. Meier, “Two-parameter debye-h ckel approximation for the evaluation of mean activity coefficients of 109 electrolytes,” *Anal. Chim. Acta*, vol. 136, pp. 363–368, Jan. 1982, doi: 10.1016/S0003-2670(01)95397-8.
- [82] S.-Y. Fan, S. Khuntia, C. H. Ahn, B. Zhang, and L.-C. Tai, “Electrochemical Devices to Monitor Ionic Analytes for Healthcare and Industrial Applications,” *Chemosensors*, vol. 10, no. 1, Art. no. 1, Jan. 2022, doi: 10.3390/chemosensors10010022.
- [83] Y. Shao, Y. Ying, and J. Ping, “Recent advances in solid-contact ion-selective electrodes: functional materials, transduction mechanisms, and development trends,” *Chem. Soc. Rev.*, vol. 49, no. 13, pp. 4405–4465, 2020, doi: 10.1039/C9CS00587K.
- [84] T. Yin, D. Pan, and W. Qin, “All-Solid-State Polymeric Membrane Ion-Selective Miniaturized Electrodes Based on a Nanoporous Gold Film as Solid Contact,” *Anal. Chem.*, vol. 86, no. 22, pp. 11038–11044, Nov. 2014, doi: 10.1021/ac5029209.
- [85] E. Jaworska, M. W jcik, A. Kisiel, J. Mieczkowski, and A. Michalska, “Gold nanoparticles solid contact for ion-selective electrodes of highly stable potential readings,” *Talanta*, vol. 85, no. 4, pp. 1986–1989, Sep. 2011, doi: 10.1016/j.talanta.2011.07.049.
- [86] B. Paczosa-Bator, L. Cabaj, R. Piech, and K. Skupie , “Potentiometric Sensors with Carbon Black Supporting Platinum Nanoparticles,” *Anal. Chem.*, vol. 85, no. 21, pp. 10255–10261, Nov. 2013, doi: 10.1021/ac402885y.

- [87] F. Li *et al.*, “All-solid-state potassium-selective electrode using graphene as the solid contact,” *The Analyst*, vol. 137, no. 3, pp. 618–623, 2012, doi: 10.1039/C1AN15705A.
- [88] F. Criscuolo, F. Cantu, I. Taurino, S. Carrara, and G. De Micheli, “A Wearable Electrochemical Sensing System for Non-Invasive Monitoring of Lithium Drug in Bipolar Disorder,” *IEEE Sens. J.*, vol. 21, no. 8, pp. 9649–9656, Apr. 2021, doi: 10.1109/JSEN.2020.3009538.
- [89] E. M. Hussien and A. R. Derar, “3D spongy-like Au film for highly stable solid contact potentiometric ion selective electrode: application to drug analysis,” *SN Appl. Sci.*, vol. 1, no. 4, p. 338, Apr. 2019, doi: 10.1007/s42452-019-0349-z.
- [90] A. Lewenstam, “Routines and Challenges in Clinical Application of Electrochemical Ion-Sensors,” *Electroanalysis*, vol. 26, no. 6, pp. 1171–1181, 2014, doi: 10.1002/elan.201400061.
- [91] O. K. Echendu, K. B. Okeoma, C. I. Oriaku, and I. M. Dharmadasa, “Electrochemical deposition of CdTe semiconductor thin films for solar cell application using two-electrode and three-electrode configurations: A comparative study,” *Adv. Mater. Sci. Eng.*, vol. 2016, 2016, doi: 10.1155/2016/3581725.
- [92] F. M. Abdel-Haleem, M. Saad, A. Barhoum, M. Bechelany, and M. S. Rizk, “PVC membrane, coated-wire, and carbon-paste ion-selective electrodes for potentiometric determination of galantamine hydrobromide in physiological fluids,” *Mater. Sci. Eng. C*, vol. 89, pp. 140–148, Aug. 2018, doi: 10.1016/j.msec.2018.04.001.
- [93] The GIMP Development Team, “GIMP.” Jun. 12, 2019. [Online]. Available: <https://www.gimp.org>
- [94] C. A. Schneider, W. S. Rasband, and K. W. Eliceiri, “NIH Image to ImageJ: 25 years of image analysis,” *Nat. Methods*, vol. 9, no. 7, pp. 671–675, Jul. 2012, doi: 10.1038/nmeth.2089.
- [95] R. P. Buck and E. Lindner, “Recommendations for nomenclature of ionselective electrodes (IUPAC Recommendations 1994),” *Pure Appl. Chem.*, vol. 66, no. 12, pp. 2527–2536, Jan. 1994, doi: 10.1351/pac199466122527.